RICE UNIVERSITY

Rydberg-atom synthetic dimensions

By

Soumya Kamal Kanungo

A THESIS SUBMITTED
IN PARTIAL FULFILLMENT OF THE
REQUIREMENTS FOR THE DEGREE

Doctor of Philosophy

APPROVED, THESIS COMMITTEE

Thomas Killian

Thomas Killian
Dean of the Wiess School of Natural Sciences
Professor, Physics and Astronomy

Barry Dunning

F. Barry Dunning
Sam and Helen Worden Professor,
Physics and Astronomy

Songtao Chen

Songtao Chen
Assistant Professor, Electrical and
Computer Engineering

HOUSTON, TEXAS

August 2022

RICE UNIVERSITY

Rydberg-atom synthetic dimensions

by

Soumya Kamal Kanungo

A Thesis Submitted
in Partial Fulfillment of the
Requirements for the Degree

Doctor of Philosophy

Approved, Thesis Committee:

Thomas C. Killian, Chair
Professor of Physics and Astronomy

F. Barry Dunning
Sam and Helen Worden Professor of
Physics and Astronomy

Songtao Chen
Assistant Professor, Electrical and
Computer Engineering

Houston, Texas

Aug, 2022

ABSTRACT

Rydberg-atom synthetic dimensions

by

Soumya Kamal Kanungo

Synthetic dimensions are powerful tools for quantum simulation and computation. They are realized by harnessing internal or external degrees of freedom of an atom or molecule, which can mimic the motion of an electron in a real-space lattice potential. Such degrees of freedom are highly tunable and can be engineered to create configurations difficult to access or realize in real space. Some of the exciting possibilities include realizing higher dimensions systems[1, 2, 3], nontrivial real space[4, 5] and band structure[6, 7] topologies and artificial gauge fields[8, 9]. Experiments have utilized various degrees of freedom to create synthetic dimensions, such as motional[10, 11], spin[8, 12, 13, 14] and rotational[15] levels of atoms and molecules, and frequency modes, spatial modes, and arrival times in photonic systems[16]. Atomic synthetic dimensions have demonstrated artificial gauge fields, spin-orbit coupling, chiral edge states using Raman-coupled ground magnetic sublevels[8, 12, 17] of atoms, and phenomena such as Anderson localization using two-photon Bragg transitions by coupling free-particle momentum states[18]. Here, we harness the Rydberg levels of ^{84}Sr to realize a synthetic lattice for studying quantum matter. Resonant millimeter-wave (mm-wave) radiation coupling Rydberg levels $|i\rangle$ and $|j\rangle$ with amplitude Ω_{ij} (Rabi frequency) are described by the same Hamiltonian as a particle tunneling between lattice sites $|i\rangle$ and $|j\rangle$ with tunneling amplitude $J_{ij} = \Omega_{ij}/2$. The mathematical equivalence

to particles moving in a real-space lattice enables Rydberg levels to function as a synthetic spatial dimension. Rydberg-atom synthetic dimensions offer control over connectivity, tunneling rates and on-site potentials, which allows for the creation of a broad range of synthetic dimensional system. The capabilities of such a system are demonstrated by realizing the famous Su-Schrieffer-Heeger(SSH) model[19] and studying its topologically protected edge states(TPS).

Contents

Illustrations

Tables

Acknowledgments

August 2016 was a month of adjustments as I came to live in a new country, with new ways of life. I was nervous, lacking confidence and possessing a bit of imposter's syndrome. Not a great combination to have when one is trying to prove oneself to the world, which is often the case, unfortunately, in the first year of grad school. After a few months of not being able to find my feet on the ground, I emailed Tom Killian for an opportunity to work in his group. I will always remember and be thankful for the first thing he said to me, "Do not worry about how much Physics you know, all that I want to see is if you are willing to explore...". In Tom, I not only had an amazing physicist as my advisor, but also a very supporting mentor who gave me the confidence I needed. I can never thank him enough. The perks of working on the Rydberg experiment is that you get to work with the "ever-inspirational" Barry Dunning, from whom I have come to admire the art of scientific writing. I truly am lucky to have not just one but two great mentors.

I am grateful for my time at Rice for many reasons. One, it molded me into an explorer, by introducing me to the thrill of standing at the horizon of certainty and trying probe the unknown. Second, it helped me discover the beauty of scientific approach. Because, at times when at the brink of knowledge, it can be quite tempting to arrive at self-satisfying answers due to the biases of the human mind. My time here taught me to understand and acknowledge those biases while developing critical thinking skills to navigate through uncertain terrains. It is not as easy to practice as it is write or speak about it, unless you have colleagues like Roger and Joe. They made experimental explorations look, dare I say it, "sexy". I have been so fortunate to have them around in my initial years. Along with them, I would like to thank

Jim, Thomas, Josh and Grant, who were always encouraging, and watching them do Physics was a great learning experience. I hope to have learnt important bits to pass those on to the next generation of amazing Killian lab physicists in Yi, Brent, Chuanyu, Mackenzie and Nina, with whom it always is a pleasure to discuss physics and life.

My grad life in Houston would not be complete without my friends. And I am proud to call some truly amazing human beings as my best friends. In Gaurav Harsha I got a brother that I never had. A brilliant theoretical physicist in his own right with whom I loved sharing not only ideas, but also food, a house and my first alcoholic drink ever. With Kedar and Yash I had some of the most memorable times of my life pulling pranks, cracking jokes, and playing poker all over Houston! The countless card game nights with Gaurav, Kedar, Yash, Aditya (the guy who never missed a chance to bring microwavable food to eat before card games) and Zaid (my heads-up poker nemesis:)!) are the happiest moments that I can recall. There was also countless hours spent on the soccer field where I formed many beautiful friendships. Thank you to all of you for being there always!

Last but not the least, I want to thank you, Amber, for bringing color into life. With you by my side, I have learnt to look at life with a new sense of excitement and enthusiasm. I love you so much, and can't wait for our new exciting adventures together!

I would like to dedicate this thesis to my grandparents, Ramesh Chandra Kanungo and Usha Rani Kanungo, and my parents, Debesh Prasad Kanungo and Kabita Kanungo. All my accomplishments are your accomplishments.

Chapter 1

Introduction

The title of the thesis is an amalgamation of two exciting fields of atomic physics, "Rydberg atoms" and "synthetic dimensions". Rydberg atoms have a rich history and have been a topic of study since the inception of the modern atomic theory and have had profound use in numerous experiments over the years. In contrast, the concept of a synthetic dimension is fresh and new. This new research arena holds promise for exploring many-body quantum systems that are analogs of real materials as well as engineering exotic systems that are non-existent in nature. Recently, it has generated hot interest for understanding topological quantum matter and its phase transitions[16]. In this thesis, a new platform for synthetic dimensions based on Rydberg atomic states is explored and the powers of such a synthetic space is demonstrated by simulating a 1-D lattice model described by the Su-Schrieffer-Heeger(SSH) Hamiltonian[19]. These initial experiments probe the single-particle band structure and properties of the topologically protected edge states.

We begin our journey with the evergreen topic of Rydberg atoms.

1.1 Rydberg atoms

Swiss teacher Johann Balmer (1825-1898) formulated his famous expression to describe the wavelengths of Hydrogen emission lines observed from a discharge lamp in the middle of 1880s. But it was not until the next 15 years and the discovery of

Einstein's photoelectric effect, physicists started to think deeply about the internal energy structure of an atom. Niels Bohr, finally, was able to concoct a working atomic theory based on Einstein's idea, where the internal energy states of an atom were postulated to be discrete, or in other words, "quantized". This was revolutionary, and it led to the development of modern quantum mechanics. The atom became understood to only absorb or emit radiation matching the internal energy difference between its two states. Moreover, the ladder of energy states was discovered to be non-linear, i.e., the energy difference between consecutive levels decreases exponentially with the total energy of the atom. The Rydberg formula for a Hydrogen atom, which captures this behavior, is given by:

$$E_n = \frac{-R_y}{n^2} \tag{1.1}$$

E_n is the energy for an internal state of the atom labeled by the principal quantum number n. $R_y \approx 13.6$ eV[1] is the Rydberg constant. Note, the energy is described by a negative quantity as the electron and the nucleus form a bound state.

Property	n-scaling	Sr $5s38s\ ^3S_1$
Rydberg radius	n^2	$2200a_0$
Binding energy	n^{-2}	1200 cm^{-1}
Polarizability	n^7	7 MHz/(V/cm)^2
Lifetime	n^3	21 μs

Table 1.1 : Table showing the $n-$scaling of various properties of a Rydberg atom. The typical values for a strontium Rydberg atom excited to $n = 38$ are in the third column.

A Rydberg atom is an atom with at least one valence electron excited to a high

[1] 1 eV $\approx$ 8065.73 cm^{-1}. Rydberg constant for Hydrogen in this unit is 109737.3 cm^{-1}.

principal quantum number, where $n >> 1$. These atoms possess exaggerated properties, some of which are listed in table 1.1. One such property is the scaling of the binding energy, which causes difference in energy required to excite an atom to the next higher level to decrease as n^{-3}. To put this into perspective, one can excite a Hydrogen Rydberg atom from $n = 70$ to $n = 71$ with ~ 19 GHz (or 1.9×10^{10} Hz) radiation, while exciting the same atom from $n = 1$ to $n = 2$ requires ~ 2.4 PHz (or 2.4×10^{15} Hz) radiation, a difference of five orders of magnitude. This is an important property in the creation of a synthetic dimension based on Rydberg atomic states[20], as elucidated in this thesis.

Another widely useful property is the large tunable Rydberg-Rydberg interaction strengths, characterized by the C_3 and C_6 coefficients, which describe resonant dipole-dipole interaction, including Forster resonance ($\sim 1/R^3$ potential)[21, 22], and Van der Waals interaction ($\sim 1/R^6$ potential)[23, 24] respectively. This provides exquisite control over interaction strengths covering a range which spans across weak to strongly correlated regimes of many-body systems. This is also the basis of the Rydberg blockade effect[25], which has profound uses in collective Rydberg excitations and creation of single-photon sources[26, 27], quantum information and implementation of two-qubit gates[28].

1.1.1 Strontium and its Rydberg states

Strontium([Kr]$5s^2$) is a heavy alkaline earth metal with two valence electrons and a completely filled inner shell[2]. The two valence electrons provide all alkaline earth metals, like strontium, with a series of singlet and triplet states. The electron spins

[2]Kr stands for the noble gas krypton, whose atomic number is 36. The atomic number of strontium is 38.

Quantum state	$^3S_1$	$^3P_0$	$^3P_1$	$^3P_2$	$^1S_0$	$^1P_1$
Quantum defect (δ_{lj})	3.371	2.8866	2.8824	2.8719	3.2689	2.7295

Table 1.2 : Table showing the quantum defect values for relevant strontium states represented in the spectroscopic notation of $^{2s+1}l_j$, where s is the spin quantum number, l is the orbital angular momentum and j is the total angular momentum[23, 29].

are anti-aligned for singlet states whereas they are aligned for triplet states. It also has four major isotopes, ^{88}Sr, ^{87}Sr, ^{86}Sr and ^{84}Sr. Only ^{87}Sr is a fermion with nuclear spin $I = 9/2$ and the rest are bosons with a nuclear spin $I = 0$[3]. In this thesis, we focus on ^{84}Sr and its atomic states.

A strontium Rydberg atom is similar to a hydrogen Rydberg atom when one of its valence electrons is excited to a high-n state. But unlike in hydrogen, the Rydberg electron interacts with the inner core which results in shifting of energy levels. This lifts the degeneracy of various orbital angular momentum states(l) of a given n, as described by the modified Rydberg formula:

$$E_{nlj} = \frac{-R_y}{(n - \delta_{lj})^2} \tag{1.2}$$

where, δ_{lj} is defined as the quantum defect, which depends on the angular momentum quantum number (l) and the total angular momentum(j)[29]. Table 1.2 shows the values of quantum defects for strontium states[23]. Figure 1.1 shows the structure of Rydberg states of strontium(^{84}Sr) from $n = 57 - 62$ for both singlet and triplet states, resulting from its quantum defects. It is noteworthy that a $\sim$200 GHz frequency span contains all the Rydberg states shown in the figure.

[3] $I = 0$ implies absence of a hyperfine structure and hence, all bosonic isotopes of strontium possess a single electronic ground state, represented as $(5s^2)\,^1S_0$ in standard spectroscopic notation.

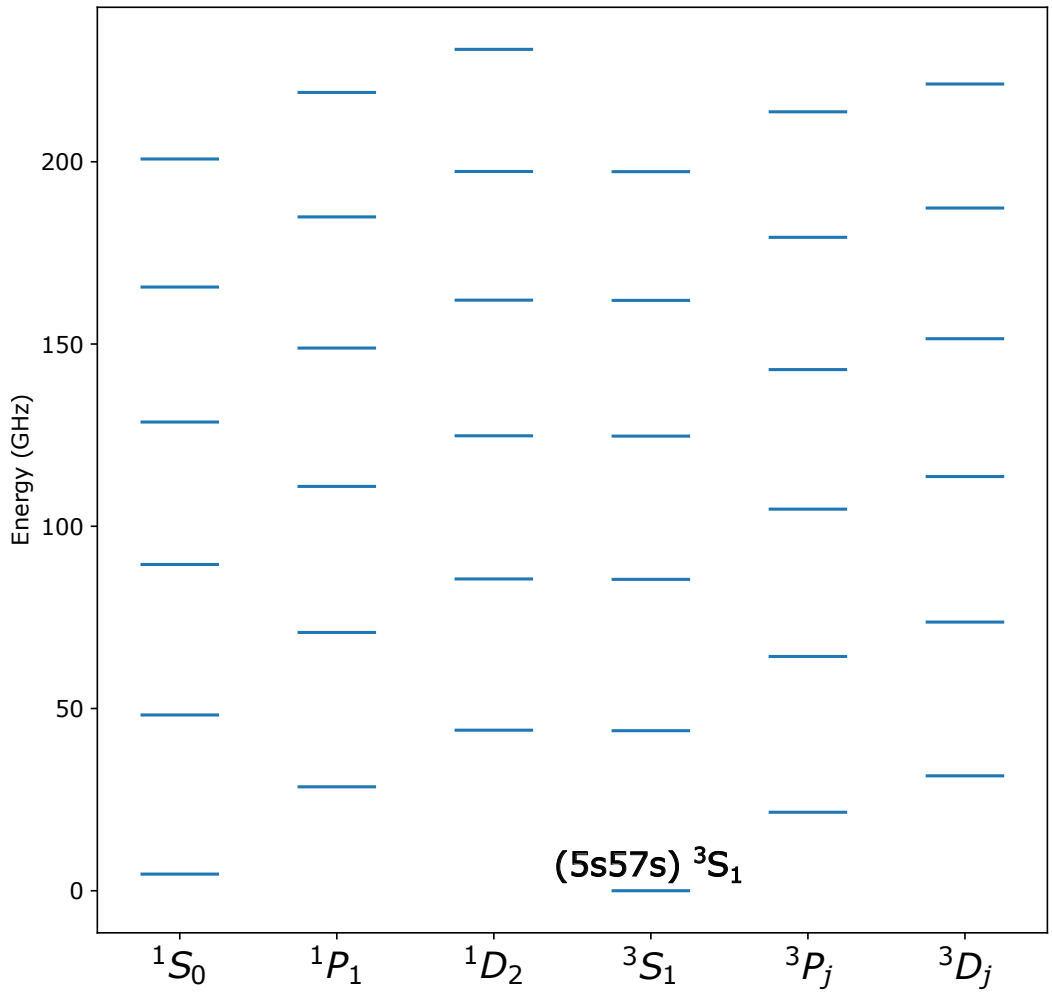

Figure 1.1 : Rydberg energy level structure for certain singlet(^1l_j) and triplet(^3l_j) states of ^{84}Sr. All energies are referenced to the energy of $(5s57s)\,^3S_1$.

1.2 Synthetic dimensions

Synthetic dimensions is a concept inspired by quantum simulation. In 1980, Feynman proposed the idea of using quantum systems to simulate other quantum systems that are classically infeasible to compute[30]. For example, total number of states of a system composed of only 300 spin-1/2 particles exceeds the total number of atoms

in the universe. The exponential scaling of the Hilbert space makes it impossible for any classical computer to store a complete quantum state of such a system.

> "Nature isn't classical, dammit, and if you want to make a simulation of nature, you'd better make it quantum mechanical..." - R. P. Feynman

1.2.1 Quantum simulation

The central idea behind a quantum simulation is using a well-controlled and flexible quantum system to emulate essential features of another quantum system of interest that is more difficult to probe. The performance of a quantum simulator depends on realizing a Hamiltonian that directly maps to the system of interest and hence, is "analogous" to the actual system. Moreover, it relies on the preparation of a quantum state that mimics the quantum state of the actual system. A measurement is often made to read-out the quantum state and extract physical information. Such systems can be used to study the equilibrium states of a quantum many-body system as well as dynamics[31].

Over the years, quantum simulators have been realized on platforms based on superconducting circuits[32], atoms[33], molecules[34], ions[31, 35], photons[36] and cavities. Such platforms have demonstrated important quantum phase transitions, such as, a superfluid to a Mott insulator transition[37] and the BEC-BCS crossover[38], implemented lattice models such as the Bose-Hubbard and Fermi-Hubbard models[39], created disordered systems, and studied topological matter.

Atomic systems are particularly attractive among the plethora of available simulators due to their high controllability over system parameters. A particular example is the study of dynamical properties by quenching the system, which is extremely tedious if not impossible for solid-state based systems. Moreover, there is existence of excit-

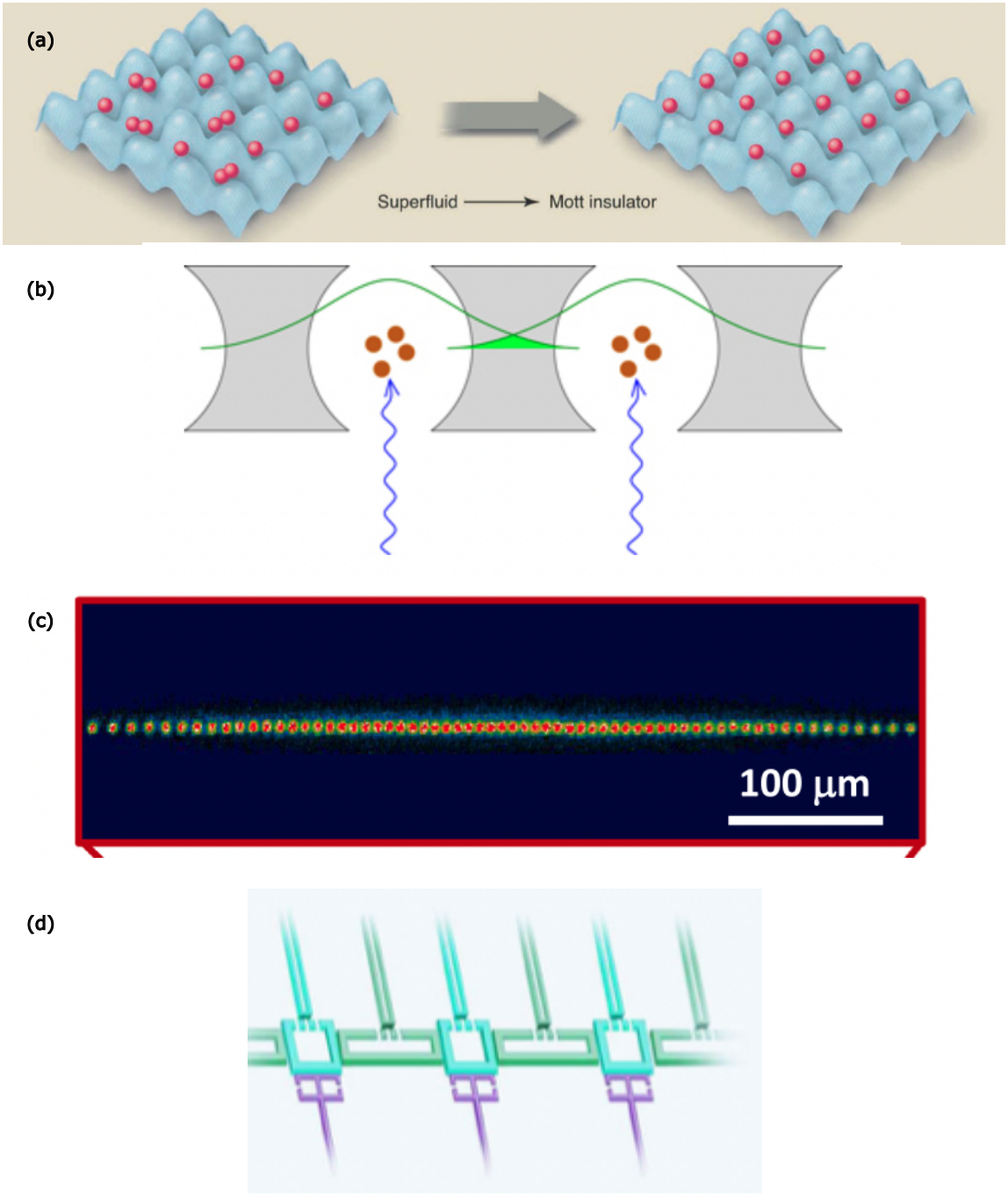

Figure 1.2 : Array of quantum simulation platforms. (a) Optical lattices (b) Atom-cavity systems (c) Ion traps (d) Superconducting circuits. Figures adapted from [40].

ing tools such as quantum gas microscopes[41], which enable probing of many-body systems atom by atom. Optical lattices present control over geometry and dimensionality which is essential in understanding physics in one, two or three dimensions. The recent development of tweezer techology[42, 43] has enabled creation of arbitrary trap arrays and lent supreme control over individual particles. Such developments promise to push the frontiers of many-body physics, quantum information, precision measurements and ultracold chemistry.

1.2.2 Synthetic dimensions: The idea!

A synthetic dimension is a degree of freedom encoded on internal or external states that can mimic the motion of a particle in a real-space lattice potential. These internal or external states may be motional[10, 11], spin[8, 12, 13, 14], or rotational[15] levels of atoms and molecules, or frequency modes, spatial modes and arrival times in photonics systems[16]. Figure 1.3 shows a few examples of platforms that have been used to realize a synthetic dimension. Artificial gauge fields, spin-orbit coupling and chiral edge states have been demonstrated with Raman-coupled ground magnetic states[Fig. 1.3(a)] and single-photon-coupled electronic orbitals[Fig. 1.3(b)]. A synthetic dimension based in the rotational states of polar molecules in conjunction with a 1-D real dimension (optical lattice or tweezers) has been proposed to observe interesting quantum phases such as quantum strings[Fig. 1.3(c)]. Free particle momentum-states of a BEC coupled by two-photon Bragg transitions have explored tailored disorders, Anderson localization and 1-D lattices such as the SSH and SSH4 models[Fig. 1.3(d)]. Eigenstates of harmonic trap where hopping is realized by periodic shaking of the trap has been proposed for realizing quantum hall physics[Fig. 1.3(e)].

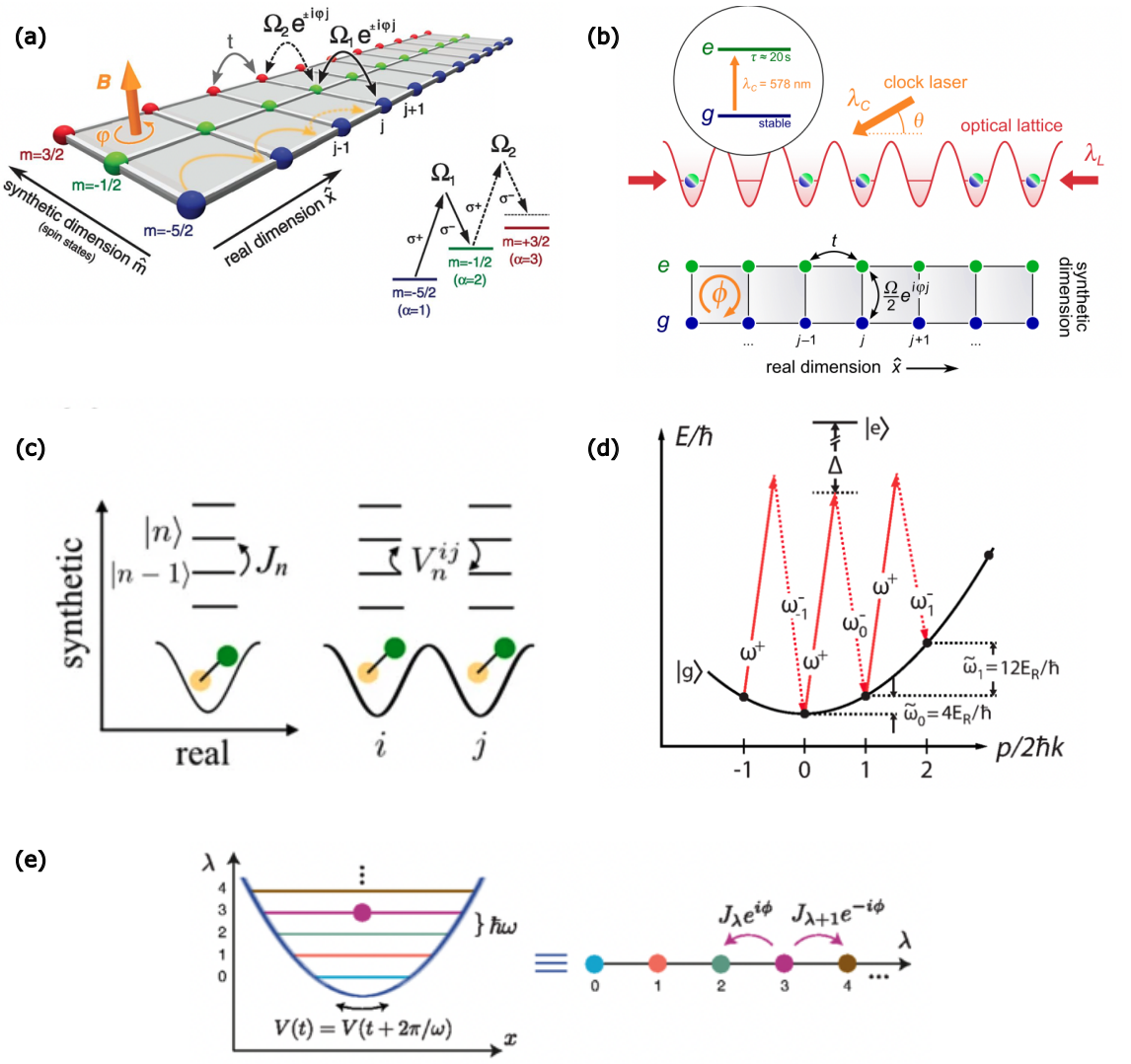

Figure 1.3 : Array of different synthetic dimension platforms. (a) Magnetic sublevels of the ground hyperfine state is utilized to construct a hybrid lattice with one real and one synthetic dimension, where, Raman transitions control hopping between synthetic sites[12]. (b) Electronic states such as clock states are used to create a series of hybrid 2D plaquettes[44]. (c) Rotational states of polar molecules can be used as a pure synthetic dimension, with microwave fields coupling different levels to realize tunneling dynamics between lattice sites[45]. (d) Momentum states of a Bose-Einstein condensate used as a pure synthetic lattice, where hopping is realized by Bragg transitions[46]. (e) Periodic shaking of a harmonic trap can potentially be used to hop between synthetic lattice sites formed by the eigenstates of the harmonic potential[47].

These systems open up exciting possibilities to realize higher-dimensional systems[1, 2, 3], non-trivial real-space[4, 5] and band-structure[6, 7] topologies and artificial gauge fields[8, 9], and tailored disorder[10].

One of the main technical challenges for these platforms has been to extend the synthetic dimension to many sites. Non-uniform Clebsch-Gordan coefficients[4] make it very demanding to couple more internal states for laser-based platforms. This has motivated a search for alternative platforms that hold the potential to circumvent some of these issues. A proposal by the group of Dr. Kaden Hazzard at Rice University suggested the possibility of harnessing the closely spaced rotational states of polar molecules, where the coupling between the states by microwave/millimeter-wave radiation could be reinterpreted as tunneling between synthetic sites. Also, the similarity of the wavefunctions resulting in large overlap integrals could bring more uniformity in coupling strength among different states.

1.2.3 A synthetic dimension on Rydberg atomic states

Rydberg atomic states create a unique experimental setting for synthetic dimensions, where the Rydberg states are interpreted as lattice sites and the dynamics is simulated by the hopping of the Rydberg electron. It offers many advantages. The plethora of Rydberg states available at high$-n$ enable intricate connectivity between many states, which is important in realizing exotic geometries and non-trivial real-space and band-structure topologies. These couplings can be created by using robust microwave or millimeter-wave sources, where, the power, phase and frequency of the microwave field fully control the tunneling amplitudes and on-site potentials on individual synthetic sites. Rydberg states also possess strong transition dipole moment, scaling as n^2,

[4]Clebsch-Gordan coefficients are used to add angular momentum in quantum mechanics.

which make large and complex synthetic landscapes feasible. Moreover, the dipole-dipole interactions between Rydberg atoms provide a mechanism to create tunable, localized interactions for many-body systems in synthetic space, which is a challenge for other atom-based platforms.

In this thesis, we harness the Rydberg levels in ^{84}Sr to create a 1-D synthetic lattice and demonstrate its capabilities by realizing the famous SSH Hamiltonian and observing its topologically protected edge states (TPS). We also test the robustness of TPS by controllably introducing disorders.

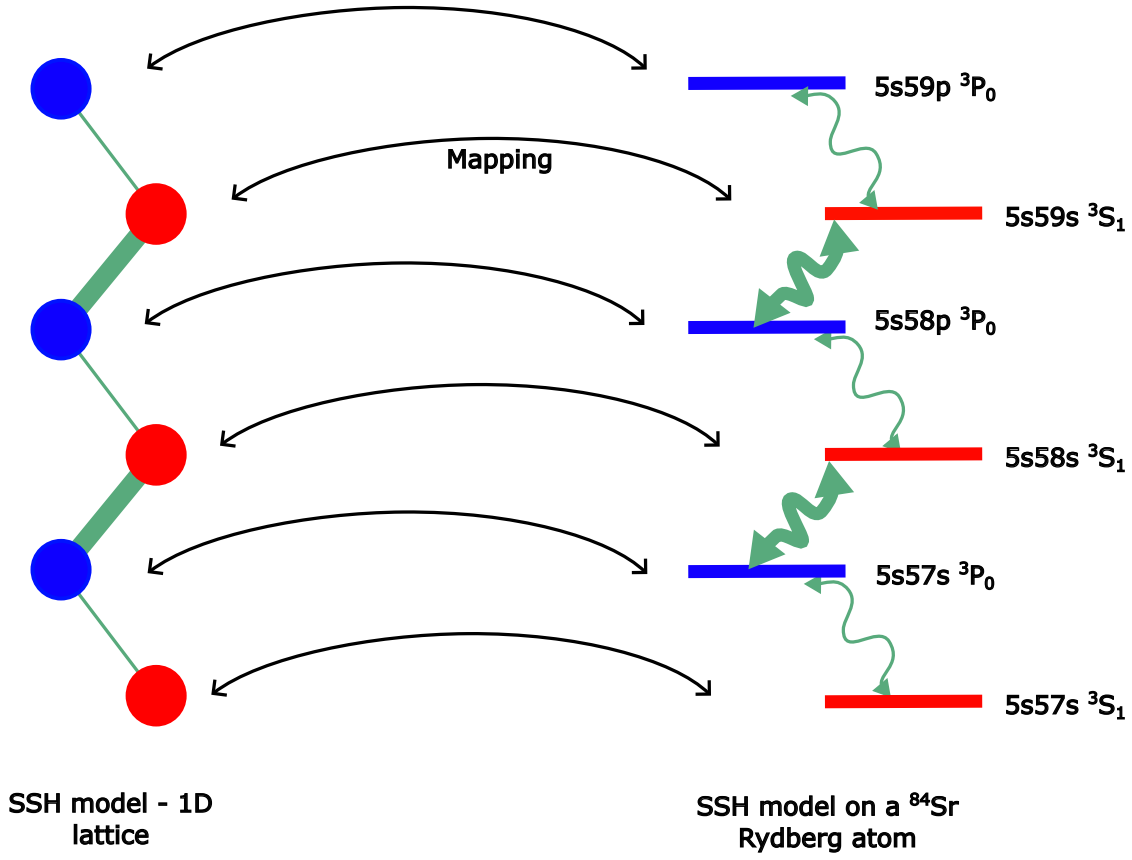

Figure 1.4 : The Rydberg atomic states of ^{84}Sr are reinterpreted as lattice sites. The strong (thick green lines) and weak (thin green lines) tunneling are realized with millimeter-wave coupling of consecutive S and P states. Standard spectroscopic notation is used to label the Rydberg states.

Chapter 2

Experimental Apparatus

Since the advent of laser cooling, atomic physics has dramatically expanded our ability to study and control quantum systems and explore fundamental laws of physics. A few of the shining feats of laser cooling include the achievement of Bose-Einstein condensate[48, 49, 50] and the creation of fermi degenerate gas[51, 52], which are paradigms of quantum statistical behavior. In our experiments we laser cool strontium, which has two valence electrons and has four stable isotopes, i.e., ^{84}Sr, ^{86}Sr, ^{87}Sr, ^{88}Sr. It is one of the few elements with which Bose-Einstein condensation[53, 54, 55, 56] and fermi degeneracy[57, 58] have been achieved. The two valence electrons introduce a series of triplet states and narrow intercombination-line transitions between singlet and triplet states. These are the basis for powerful laser cooling techniques[59] and the use of Sr in optical clocks[60]. A brief overview of our laser cooling apparatus is presented in the following sections, including other topics such as creation of Rydberg atoms in ultracold atomic samples, Rydberg detection and millimeter-wave setup for Rydberg-Rydberg transitions.

2.1 Laser cooling and trapping of Sr

Strontium possesses two main cooling transitions. $(5s^2)\,^1S_0 \longrightarrow (5s5p)\,^1P_1$ is the 461 nm dipole allowed transition with a natural linewidth of 30.5 MHz and is the first stage of laser cooling. The light scattering force generated on this strongly allowed

transition is strong enough to slow and cool atoms originating from a thermal source of atoms at ∼400 C[61, 62] to achieve a ∼1 mK magneto-optical trap(MOT), colloquially referred to as the "blue" MOT for its color[1]. During laser cooling in the blue MOT, spontaneous emission results in population leaking to the magnetically trappable state $(5s5p)\,^3P_2$ via the $(5s4d)\,^1D_2$ state. A repumper laser (481 nm) addressing the $(5s5p)\,^3P_2 \longrightarrow (5p^2)\,^3P_2$ transition puts atoms back in the $(5s5p)\,^3P_1$ state, which consequently decay back to the ground state for further cooling. $(5s^2)\,^1S_0 \longrightarrow (5s5p)\,^3P_1$ narrow intercombination line is the second major cooling transition at 689 nm with a natural linewidth of 7.5 kHz, referred to as the "red" MOT for its color. Light scattering on this transition is weaker, but it is enough to capture atoms that are pre-cooled in the blue MOT, and the forces are strong enough to hold against gravity. The narrow linewidth allows for the creation of denser and colder samples at a temperature of about a few μK. Figure 2.1 shows the relevant transitions for making cold samples of strontium. Detailed descriptions of laser cooling and trapping each isotope of strontium utilizing these transitions is provided in other theses[59, 62, 63] and will not be discussed here.

^{87}Sr is the only fermionic isotope of strontium. It has 10 ground states because of a high nuclear spin of 9/2. The details of trapping ^{87}Sr is described in this reference[64].

---

[1]The velocity of strontium atoms originating from the ∼ 400 C source is about 425 m/s. The atoms are slowed and cooled to 1 mK in three steps, which involve a 2-D collimator, a Zeeman slower and the blue MOT, utilizing the broad $(5s^2)\,^1S_0 \longrightarrow (5s5p)\,^1P_1$ transition. Extensive discussions can be found in theses by F. Camargo[61] and R. Ding[62].

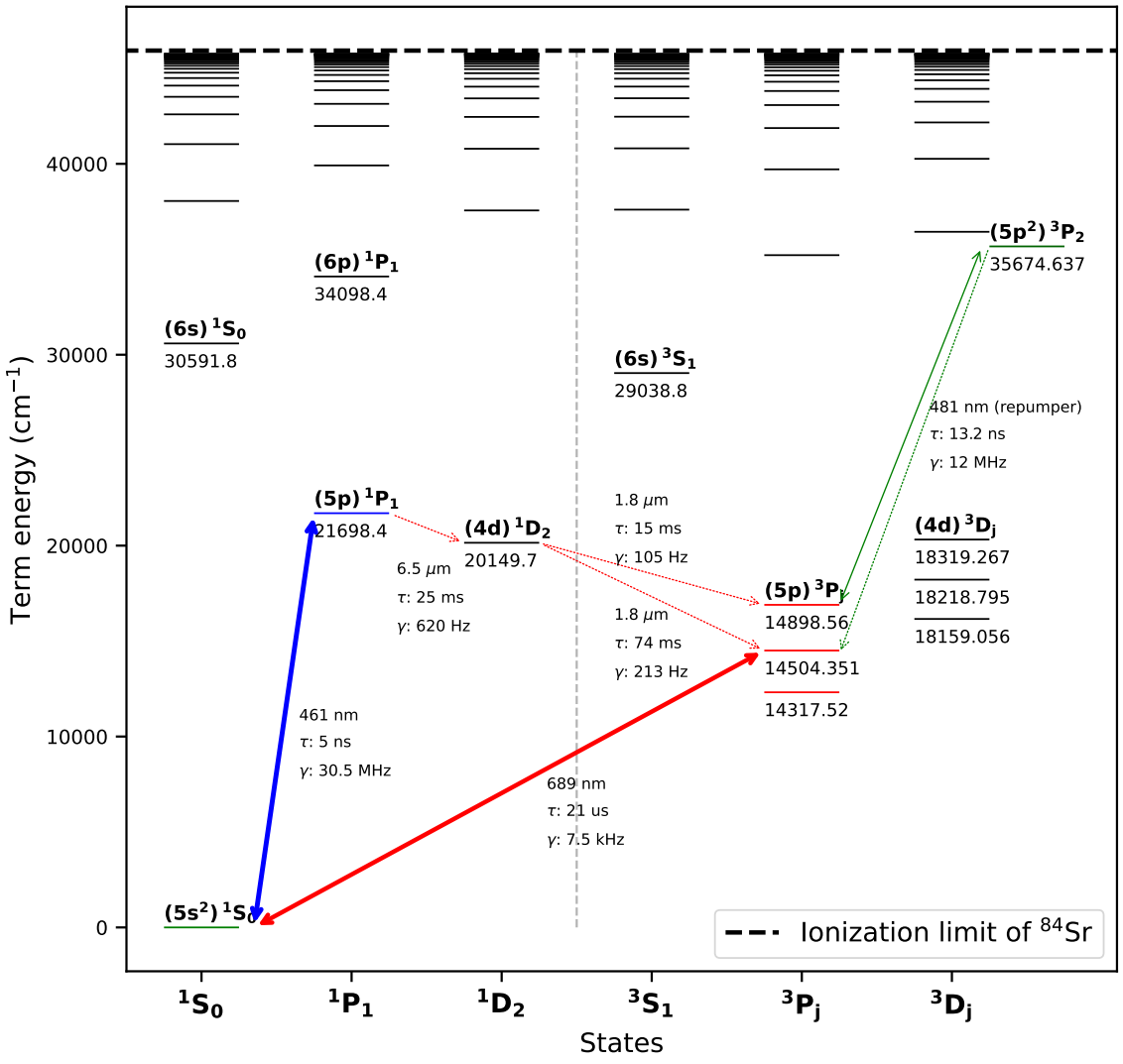

Figure 2.1 : Figure showing major transitions in ^{84}Sr used for laser cooling and trapping. The blue MOT (blue arrow) operates on the broad 30.5 MHz transition to realize a MOT of about 1 mK in temperature. The leakage via spontaneous emission from $(5s5p)\,^1P_1$ results in the population getting trapped in $(5s5p)\,^3P_2$ state. The atoms are repumped back to $(5s5p)\,^3P_1$ state via a 481 nm laser addressing the $(5s5p)\,^3P_2 \longrightarrow (5p^2)\,^3P_2$ transition (green arrows). Then, the red MOT stage operating on the 689 nm transition (bold red arrow) makes a cold sample of about 1-2 μK. All dotted lines denote spontaneous decays while solid lines are laser-excited.

Isotope	$(5s^2)\,^1S_0 - (5s5p)\,^1P_1$	$(5s^2)\,^1S_0 - (5s5p)\,^3P_1$
^{84}Sr	-270.8	-351.49
^{86}Sr	-124.8	-163.81
^{87}Sr	-46.5	-62.15
^{88}Sr	0	0

Table 2.1 : Table showing the isotope shifts of the major cooling transitions for strontium in MHz (values for ^{87}Sr are given for $J = 0$), referenced to the most abundant isotope, i.e., ^{88}Sr. The lasers are locked to the atomic resonance in ^{88}Sr and the isotope shifts are addressed by acousto-optic modulators (AOMs) to trap and cool different isotopes. Details can be found here[61, 62, 63].

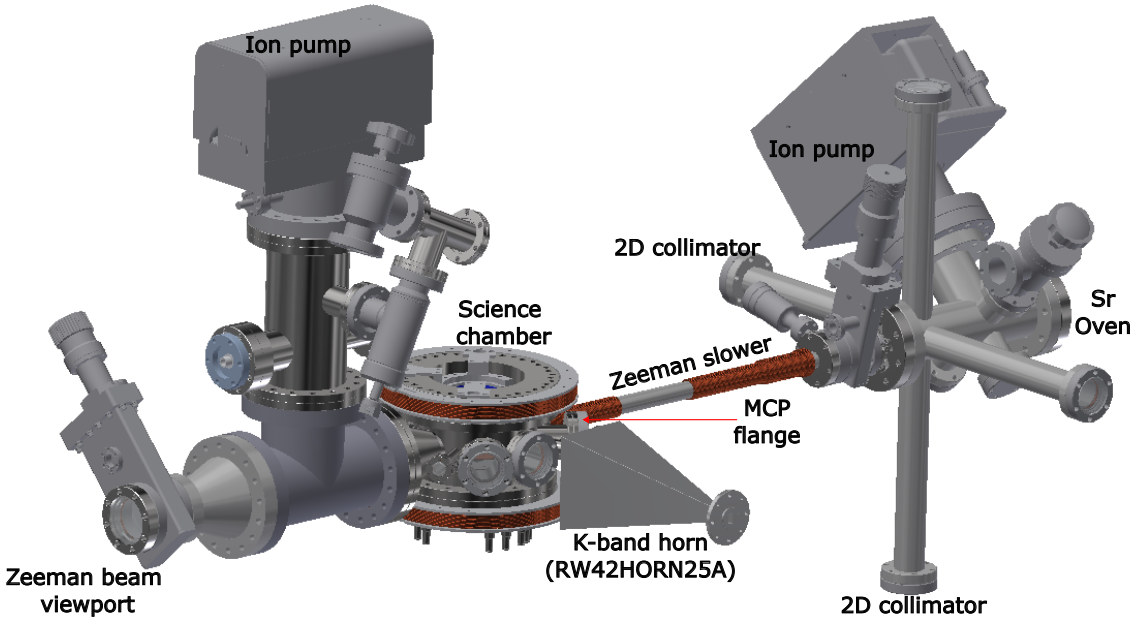

Figure 2.2 : 3D model of the atom trapping setup with few of the relevant components labeled. The horn (K-band; RW42HORN25A) is used for driving Rydberg-Rydberg transitions. The micro-channel plate (MCP) is used for detection of Rydberg species by ionizing the Rydberg electrons. Detailed description of the setup can be found here[61, 62, 63].

2.1.1 Optical dipole trap

The last stage of producing denser ultracold atoms in the experiment relies on loading the atoms trapped in the red MOT into a far-detuned optical dipole trap[65] for additional cooling via forced evaporation[66]. The induced dipole on the atom interacts with the electric field of the dipole trap light to produce a shift in the electronic state energies proportional to the intensity. Therefore a trapping potential can be engineered by sculpting a gradient in the intensity distribution. This potential is approximately conservative when the frequency of light is far-detuned from any transition, as there is minimal dissipation by scattering and the atoms stay in the ground state.

In our experiment, the dipole trap is formed by two tightly focused 1064 nm gaussian beams[67]. The wavelength of this trapping light is red-detuned from the principal transitions in strontium, which means a gaussian intensity distribution will trap ground state atoms at the most intense part of the light beam. The cross-section of both the beams is elliptical with high eccentricities, resembling a sheet geometry. The two sheet beams intersect to form a "pan-cake" shaped trap at the center to match the shape of atoms in the red MOT for efficient loading.

The intensity distribution for sheet 1 is given by:

$$I_1(x,y,z,P) = \frac{2P}{\pi\sqrt{w_y^1(x)w_z^1(x)}} e^{\frac{-2z^2}{w_z^1(x)^2}} e^{\frac{-2y^2}{w_y^1(x)^2}} \tag{2.1}$$

Similarly for sheet 2 we have

$$I_2(x,y,z,P) = \frac{2P}{\pi\sqrt{w_x^2(y)w_z^2(y)}} e^{\frac{-2z^2}{w_z^2(y)^2}} e^{\frac{-2x^2}{w_x^2(y)^2}} \tag{2.2}$$

Gravity is along z-axis. The measured beam waists for sheet 1 (i.e., at x = 0) are 231 microns (w_y^1) and 26 microns (w_z^1). For sheet 2 (i.e., at y = 0) they are 117 microns

(w_x^2) and 38 microns (w_z^2)[62, 63] [2]. The tight waist along z-axis for both beams gives rise to tight confinement along gravity.

The atomic polarizability is often well-approximated by treating the atom as a two-level system interacting with radiation. It is given as[65]:

$$\alpha(\omega_{trap}) = Re\left[6\pi\epsilon_0 c^3 \frac{\Gamma_0/\omega_0^2}{\omega_0^2 - \omega_{trap} - i(\omega_{trap}^3/\omega_0^3)\Gamma_0}\right] \tag{2.3}$$

where, ω_{trap} is the frequency of the trapping light, ω_0 and Γ_0 are the resonant frequency and decay rate of the transition. ϵ_0 and c are the vacuum permittivity and speed of light respectively. The trap potential is then written as:

$$U(x, y, z, P_1, P_2) = \frac{1}{k_B}\left[\frac{-1}{2\epsilon_0 c}\alpha\left(I_1(x, y, z, P_1) + I_2(x, y, z, P_2)\right) + mgz\right] \tag{2.4}$$

Here, P_1 and P_2 are the powers in the two beams. The potential along each axis is plotted in fig. 2.3 for a beam power of 0.75 W, which is used for loading atoms from the red MOT. Lowering of the final trap depth by the method of forced evaporation[66] leads to sub-μK atom samples.

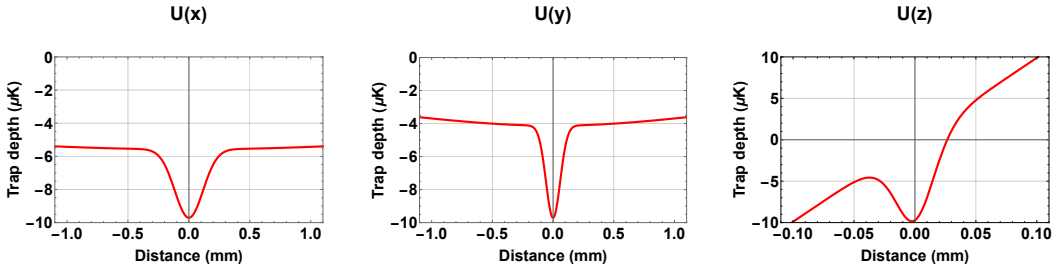

Figure 2.3 : ODT potential profile during the loading phase of atoms from the red MOT into the OPT. The power in each sheet beam is around 0.75 W.

[2] Theses by R. Ding and J. D. Whalen can be found here: https://ultracold.rice.edu/publications/

2.2 Rydberg excitation and Detection

The wavelength of light required to access Rydberg states with a single photon is around 220 nm, which is a difficult regime to manufacture a lasing media. Therefore it is standard practice in atomic physics to use multi-photon processes, such as a two-photon process, to drive atomic transitions of this energy. Various phenomena, such as Raman and Bragg transitions, rely on two-photon processes, and a sufficient description is given by second-order perturbation theory[68, 69] [3].

2.2.1 Spectroscopy beams

We employ a two-photon excitation scheme for Rydberg excitation, where the first photon (689 nm) is detuned from the intermediate $(5s5p)\,^3P_1$ state and the second photon (320 nm), whose energy is tunable, addresses a Rydberg state of interest. The 689 nm photon is typically blue-detuned from $(5s5p)\,^3P_1$ by tens of MHz. The large detuning ensures minimal single photon scattering which would otherwise lead to heating up of the sample [linewidth of $(5s5p)\,^3P_1$is about 7.5 kHz].

The 689 nm photon is generated by a a diode laser amplifier that is injection-locked to the photons from a primary 689 nm laser that is stabilized to the $(5s^2)\,^1S_0 \rightarrow (5s5p)\,^3P_1$ atomic resonance of ^{88}Sr. An acousto-optic modulator controls the detuning from the $(5s5p)\,^3P_1$ state. The photons after the AOM are coupled to a polarization-maintaining (PM) optical fiber pointed at the atoms on the output end. A polarizing beam splitter (PBS) is placed after the output coupler of the fiber to allow only p-polarized photons on to the atoms. The beam is well-collimated.

[3] An excellent tutorial on two-photon processes by Wolfgang Ketterle: MIT 8.421 Atomic and Optical Physics I, Spring 2014

The 320 nm photons are derived by second-harmonic-generation (SHG) of 640 nm photons using a Toptica SHG-pro module. The 640 nm photons are generated by a Lockheed Martin Aculight Argos Model 2400 CW optical-parametric-oscillation (OPO) cavity pumped by a 8.5 W fiber-amplified 1064 nm laser (YAR-15K-1064-LP-SF, IPG Photonics), which is seeded by a tunable 1064 nm fiber laser seed (Rock, NP Photonics). The OPO cavity holds a periodically polled non-linear crystal (magnesium-oxide-doped lithium niobate crystal, MgO:PPLN) and an etalon that allows for coarse frequency tuning in steps of ∼15 GHz. The fine tuning of frequency is achieved by setting the temperature of the 1064 nm seed laser. For active stabilization of this frequency, about 1% of the total power (1.5 W) of 640 nm photons generated from the OPO is directed through an AOM (+75 MHz) and a fibered EOM (from Jenoptik) to a ultra-low-expansion (ULE) cavity (from Stable Laser systems) with a free-spectral-range (FSR) of 1.5 GHz. Pound-Drever-Hall (PDH)[70] method is employed to generate an error signal, which is fed back to the system through a slow and a fast path. The slow path is fed to the piezoelectric transducer (PZT) of the 1064 nm seed laser, whereas the fast path modulates the drive on the 75 MHz AOM to aid frequency-locking. The stability of the frequency of the 1064 nm seed stabilizes the frequency of the OPO generated 640 nm photons and hence, also stabilizes the frequency of 320 nm photons from the SHG cavity.

The rest of the power (about 1.4 W) from the OPO is directed to the SHG module which generates about 100-180 mW of 320 nm photons[4]. The SHG module contains a bow-tie cavity and holds a non-linear crystal [Beta Barium Borate (BBO)] for second-harmonic generation. The generated 320 nm photons are then frequency shifted by

[4]The SHG-pro has a conversion efficiency of about 60%, and is capable of outputting 400 mW of UV when properly aligned and pumped with 1.4 W of 640 nm light.

a 150 MHz AOM after the cavity before being mode-coupled to a UV fiber (LMA-10-UV-PM, Alphanov). The UV fiber connects to a cage system that directs the UV beam towards the atoms located in the chamber through a vacuum viewport. The cage system contains optics that shape the UV beam to achieve a beam diameter of about 500 microns and an almost pure horizontal polarization. Less than 1% of the total UV power is sampled to monitor the power using a photodiode. Figure 2.4 provides a schematic for the frequency-stabilization of the 320 nm photons.

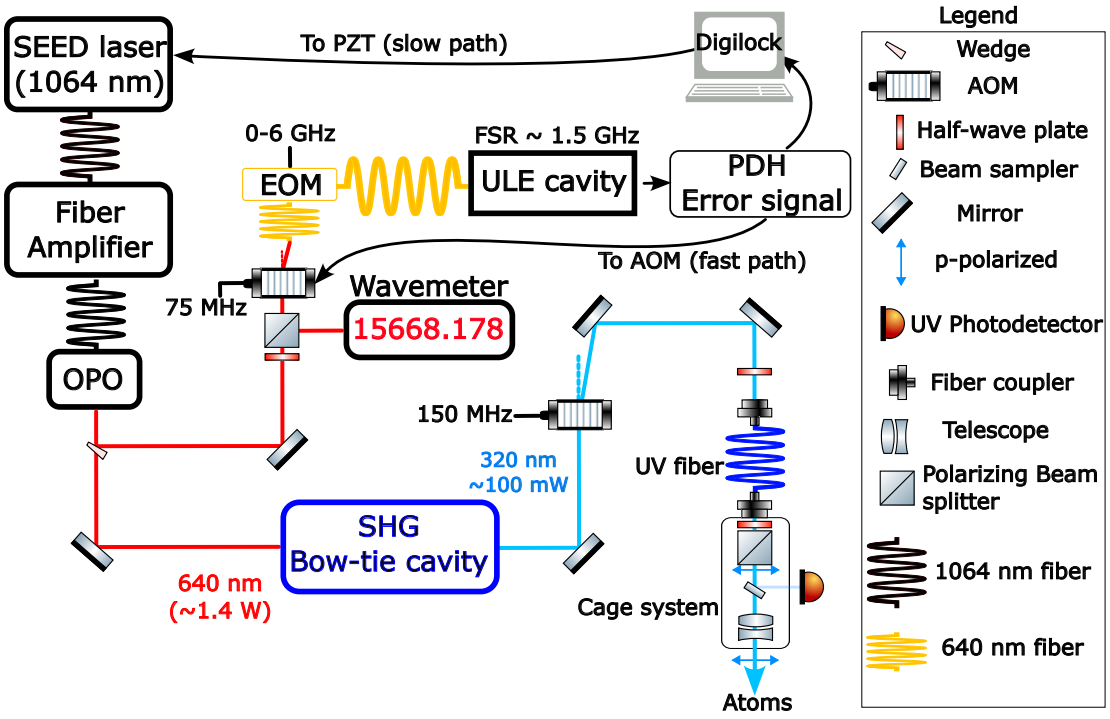

Figure 2.4 : Schematic of the generation of frequency-stabilized 320 nm spectroscopy beam.

Exposure times for both the photons on the atoms are of the order of few μs. The Rydberg energy is scanned by controlling the frequency of the drive on the fiber EOM. The power of the drive is optimized so that the ± 1 order of sidebands are maximized in power. One of the two sidebands is then locked to the ULE cavity. Change of the

drive frequency results in a change of carrier frequency, which the atoms experience. For example, if the +1 sideband is locked to the ULE cavity, increasing the drive frequency leads to a decrease in the frequency of the 640 nm carrier. Therefore, a Rydberg spectra is obtained by holding the 689 nm photon energy constant and scanning the 320 nm photon energy across a state resonance by the above method.

Figure 2.5 shows the two-photon scheme graphically. Figure 2.6 shows the spectroscopy beam configurations. The UV beam $k-$vector direction is kept fixed with a polarization parallel to the table. The red photon $k-$vector can be chosen to be counter-, co-, or perpendicular to the UV beam. The co-linear beams can address the $m = \pm 1$ magnetic sublevels of $^3S_1$ Rydberg states, whereas, the perpendicular red beam is circularly polarized and can address $m = +1$ state only.

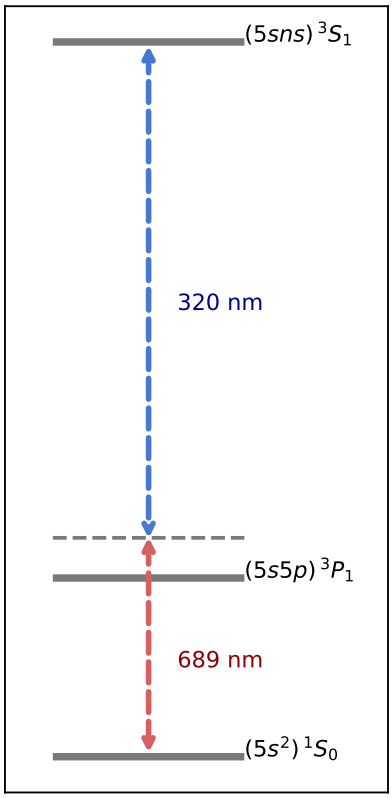

Figure 2.5 : Two-photon Rydberg excitation scheme with 689 nm and 320 nm photons. The 320 nm photon frequency is tunable to address different Rydberg states. 689 nm photon is blue-detuned by several MHz (typically ∼15 MHz) from the intermediate state.

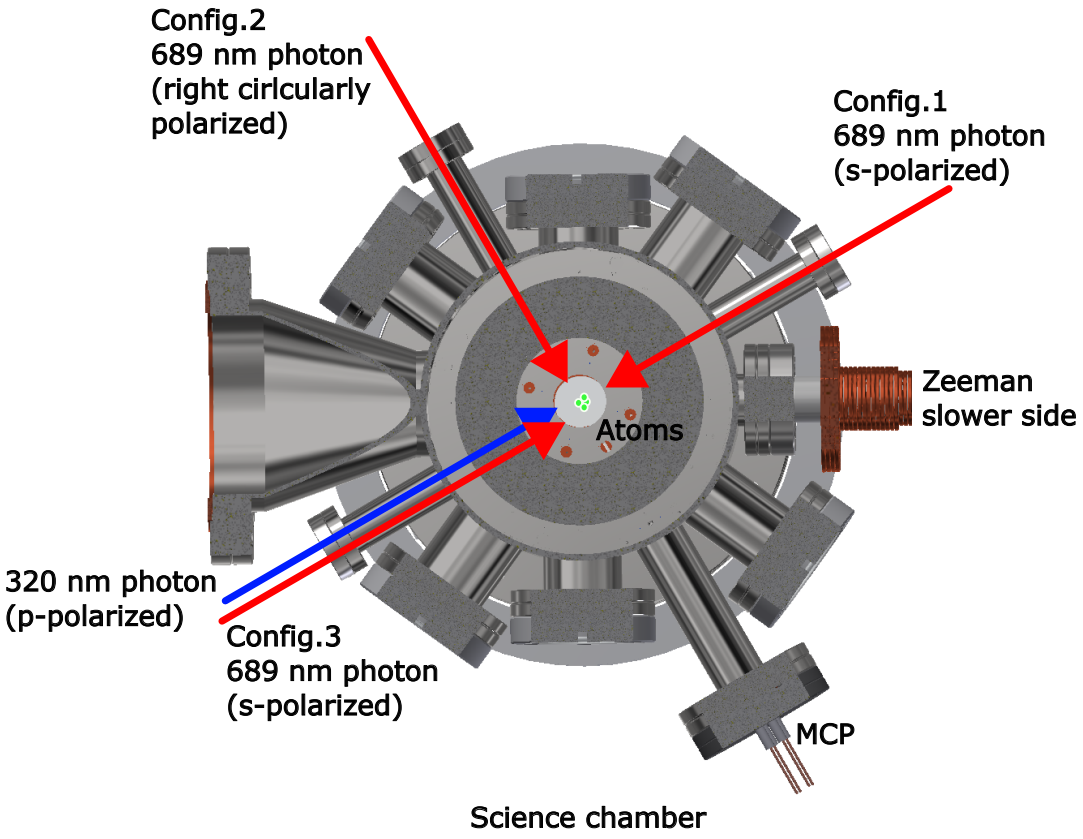

Figure 2.6 : Three different configurations of spectroscopic beams for two-photon Rydberg excitation. UV beam propagation direction and its polarization is kept fixed for all three configurations. Configuration 1 and 3 for 689 nm photons along with 320 nm photons address $m = -1, 1$ magnetic sublevels of the $(5sns)\,^3S_1$ Rydberg state. Configuration 2 for 689 nm photons with the 320 nm photons address $m = 1$ magnetic sublevel of the $(5sns)\,^3S_1$ Rydberg state. In this thesis, we use config. 1 of 689 nm photons for the two-photon Rydberg excitation.

UV fiber

The profile and propagation direction of the 320 nm UV laser from the SHG cavity changes when the wavelength is tuned to address different Rydberg states. Without a fiber intermediary, this affects the UV laser alignment to the atoms and hurts the accuracy to which the UV intensity on the atoms is known. Opting to use a UV fiber (LMA-10-UV-PM, Alphanov) that points at the atoms in the science chamber

solves the pointing issue and improves repeatability. Moreover, the mode quality of the beam is greatly improved and environmental fluctuations are mitigated.

Sidenote: Polarization maintaining optical fibers that can carry milliwatts of power in the UV bandwidth are not prevalent due to a phenomena called UV solarization. A darkening of the optical core of the fiber is induced by the intensity of the light resulting in decreased transmission. While this can occur for other wavelengths as well, the threshold for it much lower at UV wavelengths. We use a UV fiber manufactured by Alphanov (LMA-10-UV-PM) that solves this issue[71]. Figure 2.7(a) plots the profile of the UV beam on the atoms. Figure 2.7(b) shows the tip of the UV fiber viewed with a fiber inspection scope (FS200-FC, from Thorlabs).

(a)

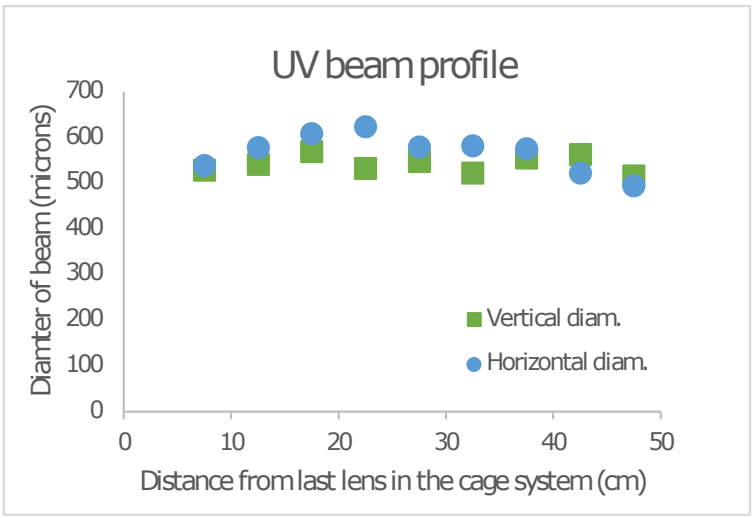

(b)

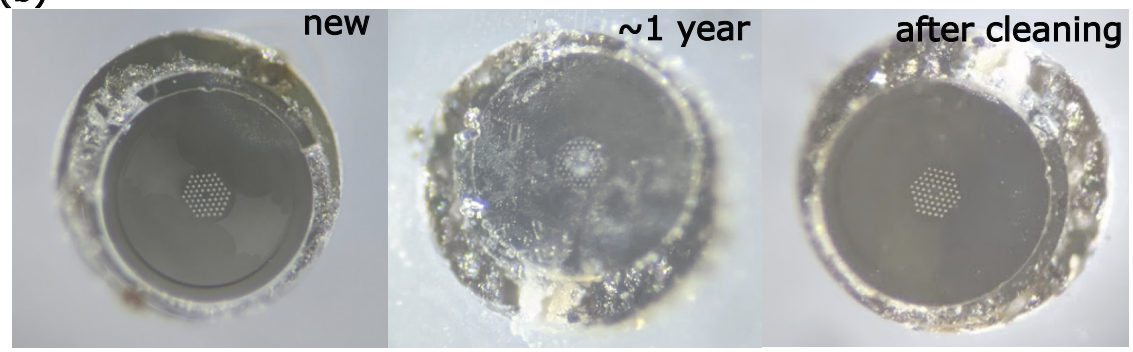

Figure 2.7 : (a) UV beam profile after the last lens on the cage system. The atoms are located at around 35 cm away. (b) UV fiber tip viewed with a fiber inspection scope (FS200-FC, from Thorlabs) before installation (left panel). UV beam intensity causes dirt accumulation over ~ 1 year (mid panel), resulting in poor coupling ($\lessapprox 5\%$). Isopropanol (99 % pure) is used to clean the tip to recover coupling efficiency ($\gtrapprox 30\%$) (right panel).

2.2.2 Selective field ionization (SFI)

Under selective-field-ionization scheme, an ionizing electric field is employed to liberate the Rydberg electron, which then can be collected with a detector, such as a micro-channel plate (MCP). The MCP's output is connected to a preamplifier, which is then fed in to an RF amplifier to remove DC offsets before going to the MCS (Multi-channel scaler) to detect pulses.

The adiabatic ionization threshold for low angular momentum states ($l \leq 1$) is given by $E_{adia} = 1/16(n-\delta)^4$[72], and hence depends on $(n-\delta)$. δ is the quantum defect of the Rydberg state.

low-n regime ($\lessapprox 60$)

For low-n experiments, the ionizing electric fields are generated by application of a voltage ramp on a set of eight plate electrodes[61] installed inside the science chamber, as shown in Fig. 2.8(a). Half (four) of the plates are connected to a positive supply while the other half is connected to a negative supply. The kinetic energy of the electrons hitting the MCP sets the efficiency of the detection process. Therefore, the magnitude and the rise time (≈ 6.5 μs for all experiments described in this thesis) of both the positive and negative ramps are kept equal to ensure zero potential on the atoms located at the geometric center of the electrodes. This implies that the electrons hit the MCP with the same kinetic energy even with different magnitude of ramps employed, when probing different principal quantum numbers.

Figure 2.8(b) shows the arrival times of Rydberg signal from different states [Fig. 2.8(c)] superposed with the electric field ramp applied to the atoms. $^3S_1$ states from different n have different ionization thresholds and therefore, the signals arrive when their respective ionization fields are reached. This feature is an important tool to differentiate between states in the SFI domain, as we will see in the following chapters.

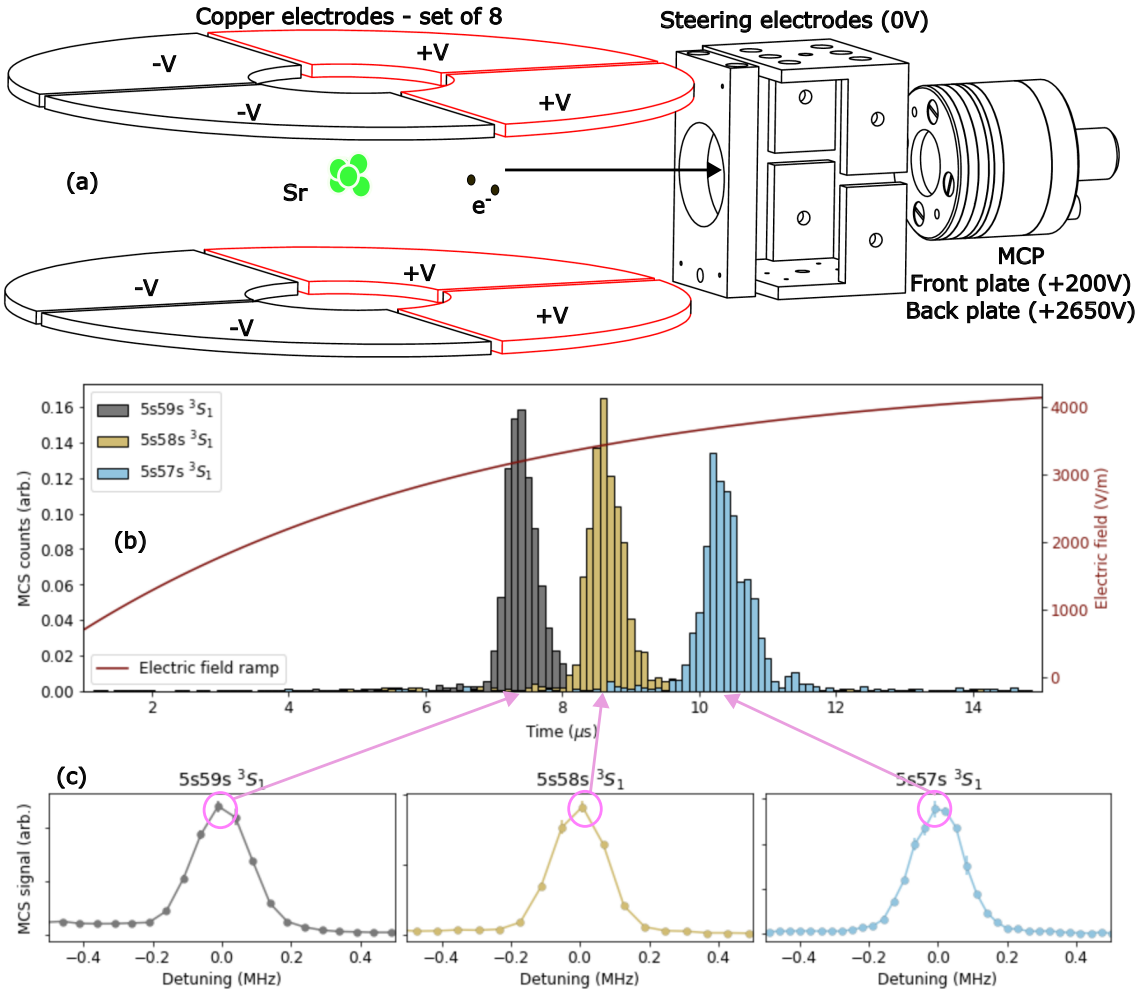

Figure 2.8 : (a) Selective field ionization setup inside the science chamber. Set of 8 electrodes apply an electric field ramp pointing towards the micro-channel plate (MCP) ionizing the Rydberg electron which gets collected at the MCP. The typical voltages are shown in the figure. The +V and -V values range anywhere from few volts to 2500V depending on the principal quantum number being probed. (b) The signal at the MCP as a function of the electric field ramp time. Different atomic states have different ionizing fields and hence their signal arrives at different intervals for a fixed ramp. (c) A single data point is obtained by summing all of the signal in the MCP spectra for a given frequency detuning. Typical Rydberg atomic state spectra are shown for three different quantum numbers.

high-n regime ($\gtrapprox 60$)- Trimming stray electric fields

Rydberg states are incredibly sensitive to the presence of electric fields due to their exaggerated polarizability ($\propto n^{*7}$). This is because of the "wobbly" nature of a Rydberg atom where the Rydberg electron is loosely bound at a far distance away from the core, possessing a large dipole moment ($\propto n^{*2}$). Stray electric fields can mix neighboring manifolds[5] at high-$n$and hence, need to be nulled to conduct spectroscopy on bare Rydberg states. An example of stark mixed states due to stray fields is shown in the upper panel of fig. 2.9(b), which results in the absence of sharp Rydberg features. The lower panel of fig. 2.9(b) shows the Rydberg manifold when the trim fields are applied and the Rydberg features near their predicted energies are recovered.

At high-n, the required fields to ionize a Rydberg electron are small and therefore, it is not necessary to drive both sets of electrodes with voltage ramps. One half of the plates are used to ionize the electrons and the rest are used to apply offset voltages to trim stray electric fields. This can be done for high-n experiments because the potential at the atoms during ionization is low enough compared to the potential drop to the MCP such that it does not affect the detection efficiency.

The algorithm to cancel these fields is based on DC stark effect. A Rydberg atomic line (in our case the $^3S_1$ state) resonance is monitored in the frequency domain as a function of offset fields applied. Since the shift in line position depends on the absolute magnitude of the field, a parabola can be traced out whose minima denotes the cancelling fields value. This is repeated for the other two axes and many iterations are performed to finely cancel the fields. Higher lying atomic states are subsequently used to increase the sensitivity to electric fields for better cancellation.

[5]Electric field required to mix neighboring manifolds is given by $1/(3n^5)$ [in atomic units].

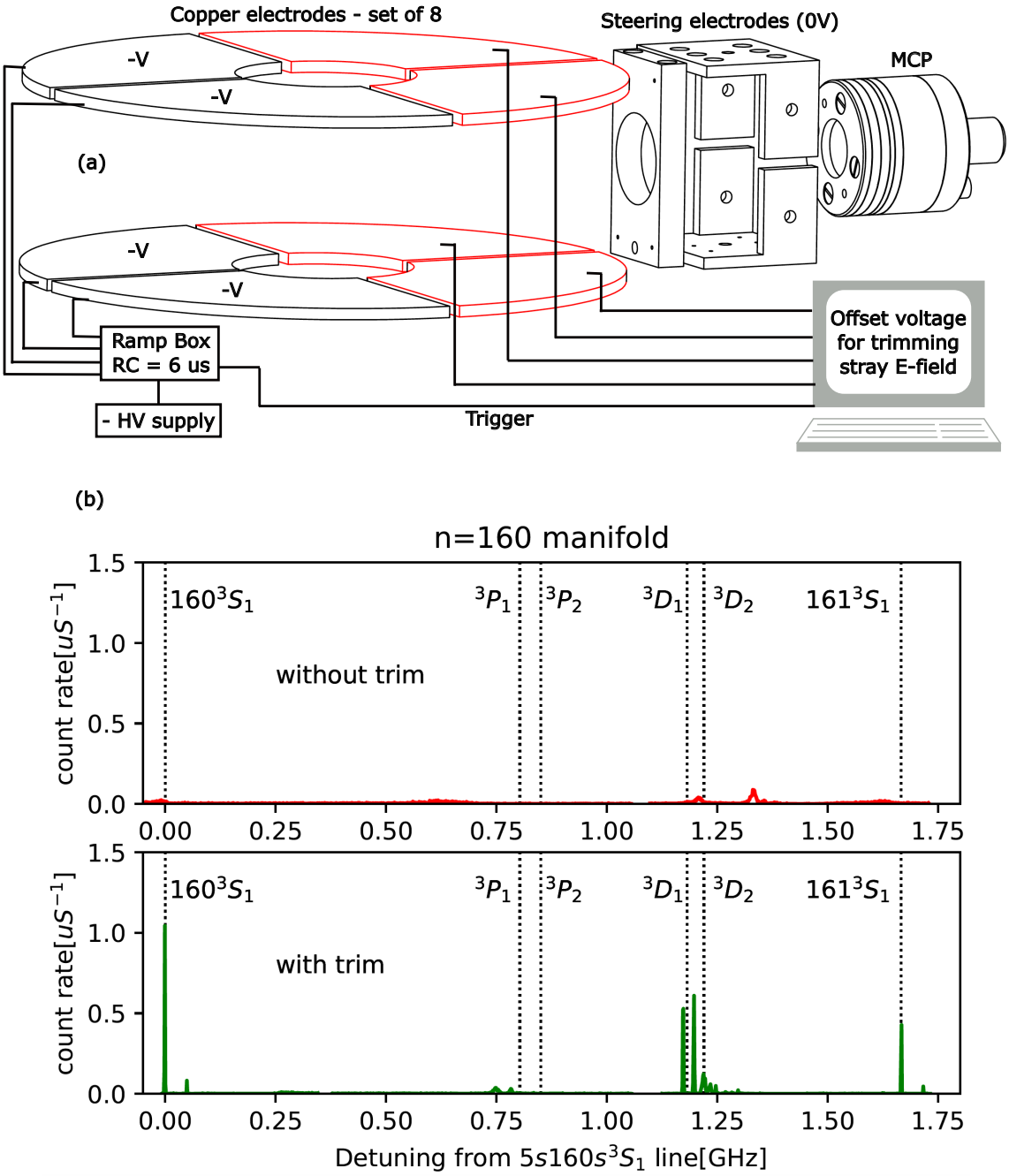

Figure 2.9 : (a) For high-n Rydberg spectroscopy, we are able to trim the stray electric fields upto 10 mV/cm. Front plates (near the MCP) are used for applying offset voltages to cancel stray electric field while the back (negative plates) plates are used for SFI detection. (b) $n = 160$ manifold with and without the stray fields is shown. Sharp Rydberg features are absent when the neighboring manifolds are mixed by stray fields (top panel), and they are recoved when trim fields are applied (bottom panel). The vertical dotted lines show the predicted positions of the Rydberg states by using literature value of quantum defects[23, 29].

2.3 Millimeter-wave setup

We have discussed methods to create Rydberg atoms by optical excitation from the ground state. Now we explore Rydberg-Rydberg transitions, which can be driven by millimeter-wave radiation at high n. The precision of the millimeter/microwave fields is a very desirable trait in terms of coherence. Moreover, the technology is already well-established and are an affordable investment in contrast to optical lasers. Among the main advantages, is the favorable scaling of wavefunction overlap between Rydberg states which allows tens of MHz Rabi frequency to be easily achievable. Figure 2.10 shows the layout of the experiment with the relevant components for driving Rydberg-Rydberg transitions.

Five 15 dBm VALON 5009 synthesizer channels, which can output frequencies upto 6 GHz, are combined with a 6-way combiner (PE20DV003). These are fed to the IF port of a mixer to be mixed with a local oscillator (LO) operating at 16 GHz. The LO is derived from a 13 dBm channel of a DS 3000 synthesizer[6] (by Syntonic). The output of the mixer contains two frequencies, which are denoted by LO+IF and LO−IF. The mixer is optimized to suppress the carrier and distribute powers in the two sidebands. The lower frequency sidebands and the carrier get rejected by the switch (RFSPSTA1840G) and the K-band horn (RW42HORN25A) whose lowest operating frequecies are 18 GHz and 17.6 GHz respectively. Therefore, only the LO+IF frequencies are experienced by the atoms. A total of ∼0 dBm power is delivered to the horn after all the insertion losses along the path. Rabi and Autler-Townes spectroscopy reveal that such levels of power are enough to realize Rabi frequencies of the order of a few MHz.

[6]Phase noise of the synthesizer, operated at 20 GHz (max.), is ~ -100 dBc/Hz, at an offset of 1 kHz.

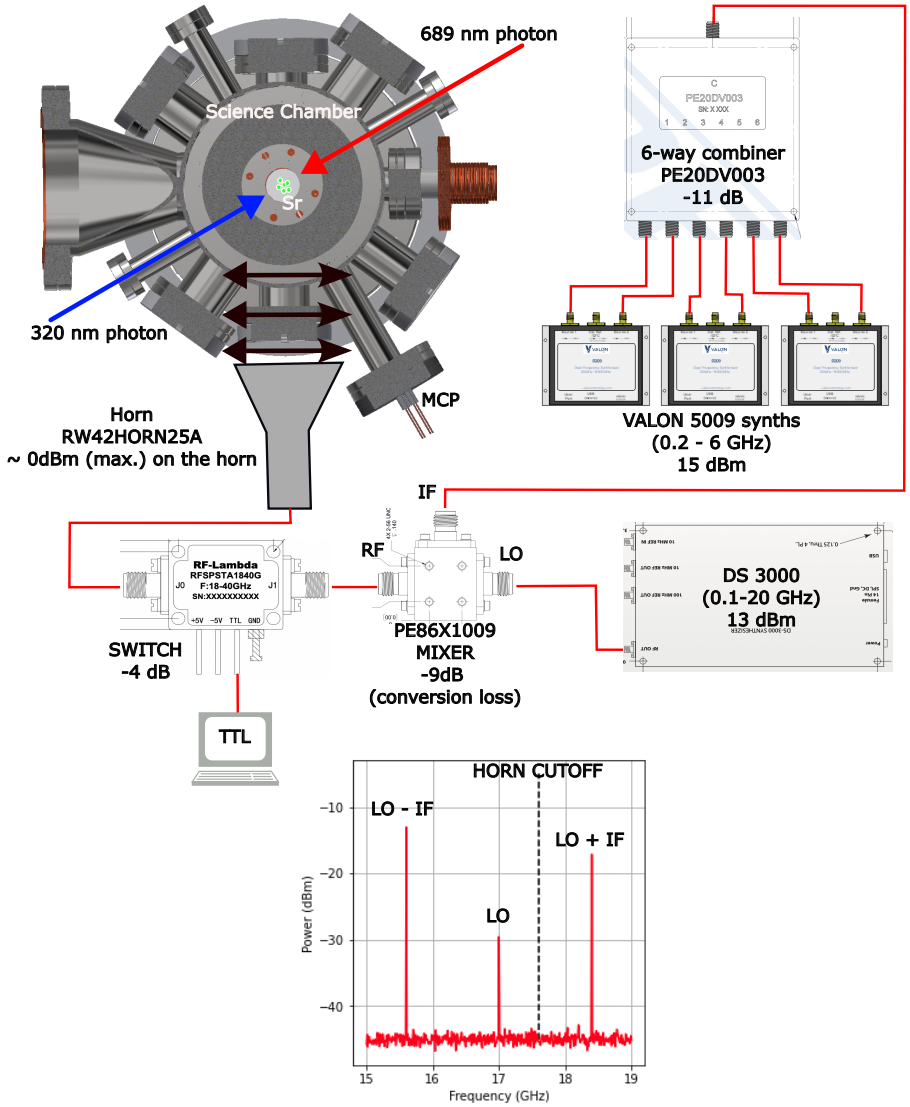

Figure 2.10 : Millimeter-wave setup to drive Rydberg-Rydberg transitions. Six commercially available (VALON 5009) synthesizer frequencies combined with a 6-way combiner (PE20DV003) are mixed with a a local oscillator (LO, DS 3000 model) driven at 17GHz (using a PE86X1009 mixer), which is then fed to a horn antenna (RW42HORN25A) via a mm-wave switch (RFSPSTA1840G, controlled by a TTL signal). The horn cutoff of 17.6 GHz suppresses the lower modes including the carrier and hence, only the positive sideband frequencies are experienced by the atoms. An example of this is shown in the graph with red traces from a fast spectrometer (Keysight-N9344C). The mm-wave polarization is parallel to the table as shown by black double-headed arrows. A maximum power of about 0 dBm reaches the horn. The figure also shows the counter-propagating configuration for Rydberg excitation from the ground state (using 689 nm and 320 nm photons). The MCP shown in the figure is used for collection of ionized Rydberg electrons.

Chapter 3

Rydberg atom and millimeter-wave radiation

In this chapter, transitions between two Rydberg levels is explored[1]. The experimental sequences to detect transitions are introduced and the subsequent analysis methods are discussed.

3.1 Search for mm-wave transitions in ^{84}Sr

The energy difference between Rydberg levels decreases as $\sim n^{-3}$, and hence it is desirable to harness Rydberg atomic states at higher principal quantum numbers to avail a larger synthetic space for a certain bandwidth. But, experimental constraints restrict the use of radiation beyond a certain wavelength. Certain factors control the choice of frequency band for the current experiment. First, the size of the vacuum viewport, through which radiation passes through and reaches the atoms inside the vacuum chamber (Fig. 2.2), puts an upper limit on the wavelength that suffer minimal attenuation. The cut-off wavelength for such a viewport (Fig. 3.1) is about 1.5 inches, which corresponds to a cut-off frequency of about 5 GHz. Hence, all bands lying above this value were initially considered. Second, the size of the horn antennae is proportional to the wavelength of radiation, i.e, larger wavelength radiation require larger horns to guide the waves. Therefore, the bands C(4-8 GHz), X (8-12 GHz)

[1]The physics is analogous to a two-level atom described in a standard quantum mechanics textbook[68].

and Ku (12-18 GHz) were ruled out due to space constraints on the experimental table. Thus, the K-band spanning over ∼17-27 GHz was chosen for the experiment described in this thesis.

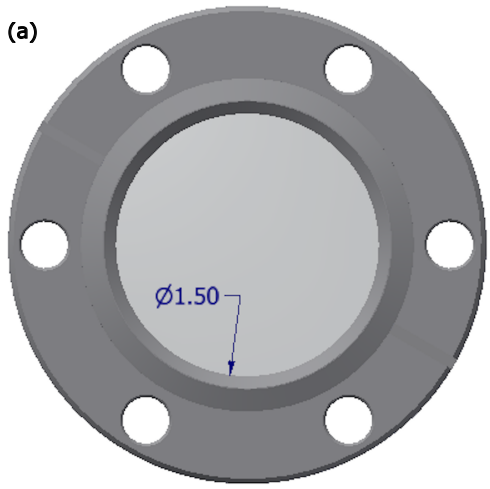

Figure 3.1 : Vacuum viewport with a diameter of 1.5 inches puts an upper limit on the wavelength of the radiation passing through and reaching the atoms.

3.1.1 Rydberg transitions in the K-band

The initial Rydberg state created using the two-photon excitation scheme presented is a $(5sns)\,^3S_1$ state. Hence, a single mm-wave photon can only drive $S-P$ transitions, whereas, two mm-wave photons can drive $S-S$ and $S-D$ transitions. In order to determine the range of principal quantum numbers for such transitions in the K-band, quantum defects from reference [23] were used to calculate the frequency difference between strontium Rydberg states. Figure 3.2 plots $(5sns)\,^3S_1-(5snp)\,^3P_j$, $(5sns)\,^3S_1-(5s(n+1)s)\,^3S_1$ and $(5sns)\,^3S_1-(5snd)\,^3D_j$ transition energies for ^{84}Sr as a function of the principal quantum number(n).

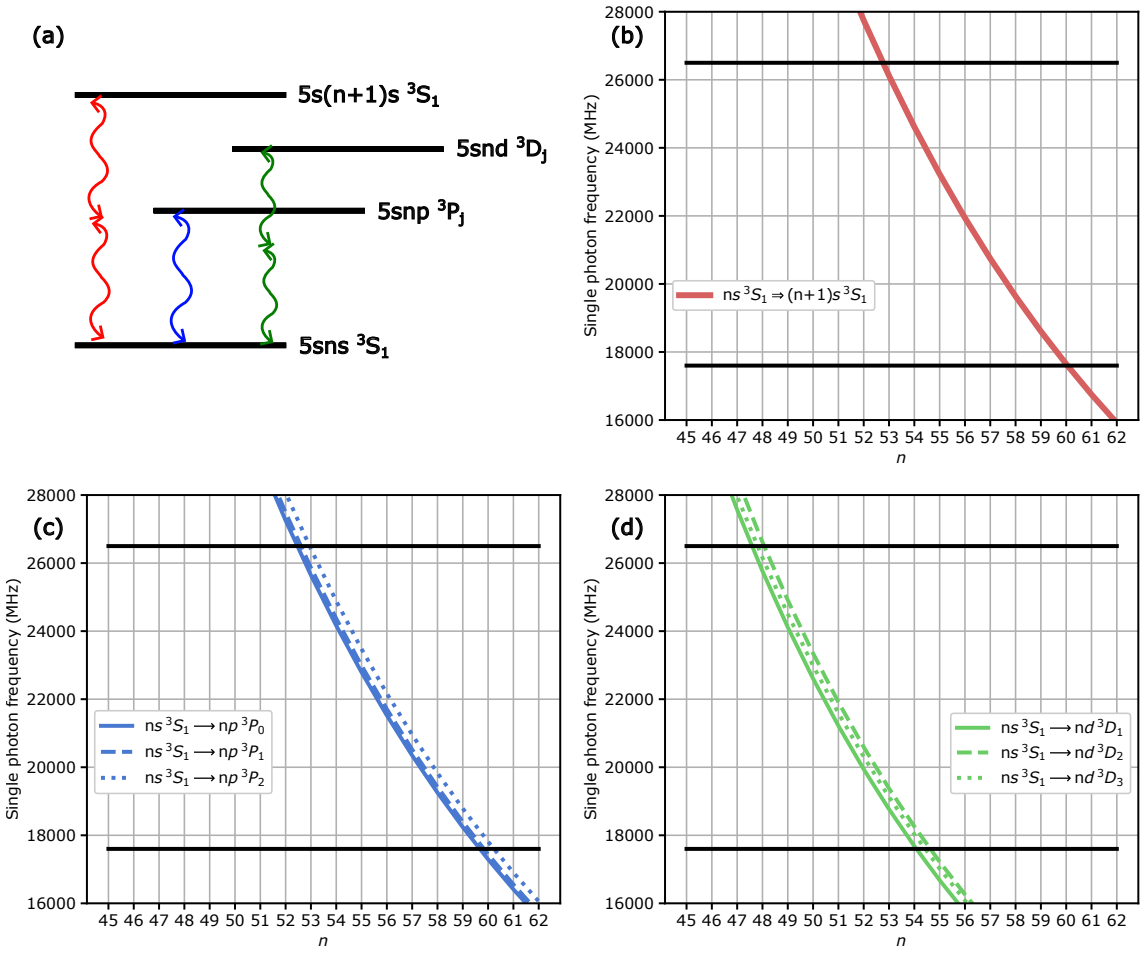

Figure 3.2 : (a) Types of Rydberg-Rydberg transitions that can be driven from the initial $(5sns)\,^3S_1$ state by using one or two mm-wave photons. (b) Two-photon $(5sns)\,^3S_1 - (5s(n+1)s)\,^3S_1$ transitions. (c) Single photon $(5sns)\,^3S_1 - (5snp)\,^3P_j$ transitions, for $j = 0, 1, 2$. (d) Two-photon $(5sns)\,^3S_1 - (5snd)\,^3D_j$ transitions, for $j = 1, 2, 3$. The black solid lines indicate the lower and upper cut-off frequencies of K-band.

3.2 Actually finding Rydberg-Rydberg transitions

3.2.1 Experimental sequences

SFI-ROI scheme

The first step under this scheme is exciting a ground-state atom to the initial Rydberg state. Therefore, Rydberg excitation lasers are turned on for a period of 10 μs to create one Rydberg atom in $(5sns)\,^3S_1$ state. The Rydberg excitation lasers are then switched off, following which the mm-waves are turned on for a desirable time period ($\sim 30\,\mu$s). This results in a Rydberg atom residing in the bath of mm-wave radiation of a certain frequency. At a near-resonant frequency and adequate intensity of mm-waves, a fraction of the initial population is transferred to the final Rydberg state. The mm-wave is then turned is off and the resulting Rydberg state is probed using selective field ionization[72], where, the atoms are subject to an electric field ramp capable of ionizing a Rydberg atom. Rydberg states have a quantum number-dependent ionization fields, which implies Rydberg states with different quantum numbers ionize at different fields, with the less bound Rydberg state ionizing earlier during an electric field ramp. This leads to the detection of Rydberg electrons at two different times, which allows for the identification of different Rydberg states with proper time resolution. Initially, the mm-wave setup was operated at full power to have maximum intensity at the atoms. This broadens the Rydberg-Rydberg transitions in the frequency domain, and increases the probability of transferring population to the final Rydberg state non-resonantly, making it easier to find a Rydberg-Rydberg transition during a frequency scan. A schematic of SFI-ROI scheme is presented in fig. 3.4(a).

At a near-resonant frequency, an atom is dressed by the two Rydberg levels, whose state vector can be described on a Bloch sphere [figure 3.3(a) and (c)]. The

state vector rotates on the surface of the Bloch sphere depending on the frequency, the duration of exposure and the intensity of the coupling radiation. For example, an equal superposition of $(5s58s)\,^3S_1$ and $(5s58p)\,^3P_0$ states of ^{84}Sr can be created by exposing the atoms to a $\pi/2$ pulse, tailored by adjusting the intensity and duration of exposure of the mm-wave radiation . The SFI spectra of such a state is shown in figure 3.3(d). The SFI spectra of a "pure" Rydberg state is shown in 3.3(b).

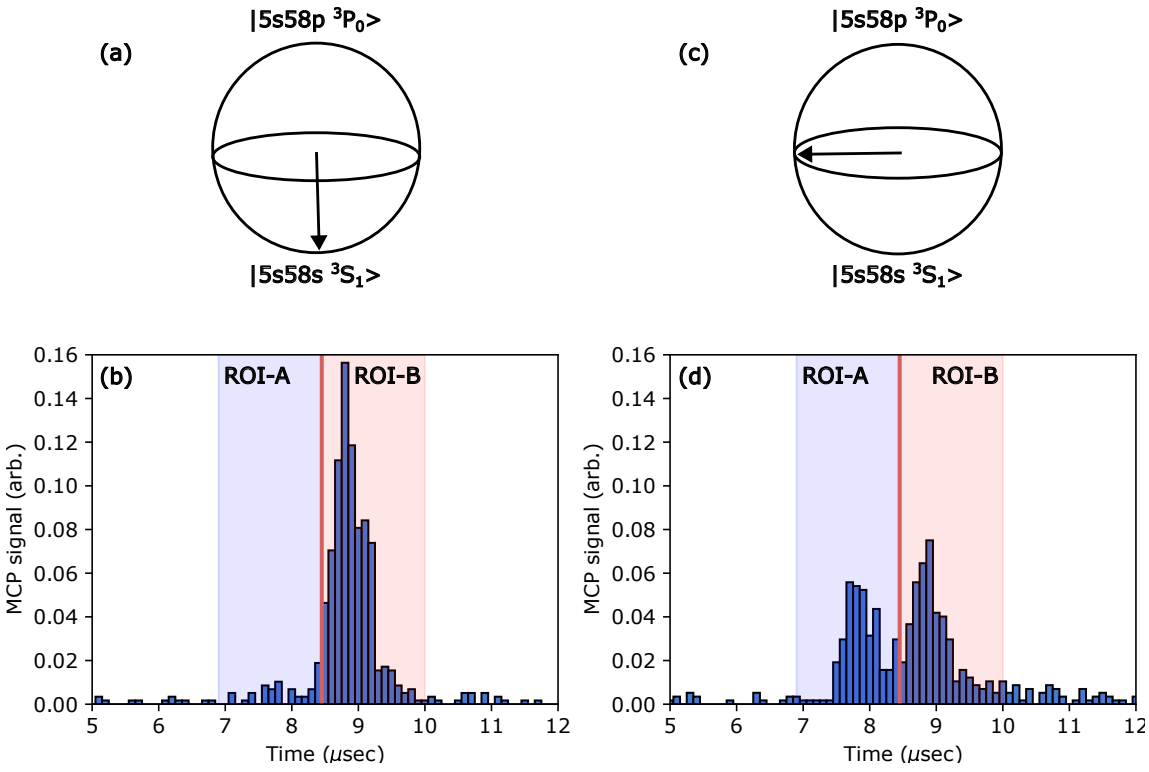

Figure 3.3 : (a) Bloch state vector for a Rydberg atom in the unperturbed state $(5s58s)\,^3S_1$. (b) SFI spectra for $(5s58s)\,^3S_1$ Rydberg state. (c) Bloch state vector for a Rydberg atom in a superposition state of $(5s58s)\,^3S_1$ and $(5s58p)\,^3P_0$ (d) SFI spectra for Rydberg atom in a superposition of $(5s58s)\,^3S_1$ and $(5s58p)\,^3P_0$ states. Blue and red shaded areas denote the ROIs for the individual Rydberg states. Signal arriving within the ROI is proportional to the population in that state.

Regions of interest (ROIs) can then be defined on the SFI spectra corresponding to each Rydberg state. Figure 3.3(b) and (d) show the blue and red shaded regions

corresponding to the two Rydberg states described earlier. The scanning of the mm-wave frequency results in a change of signal strength in the defined ROIs and hence, a mm-wave spectra can be obtained for each region, as shown in fig. 3.4(b). The peak position of such a spectra determines the resonance frequency for the transition[2].

[2]AC stark shift of the state needs to be cared for, which is described in the next chapter.

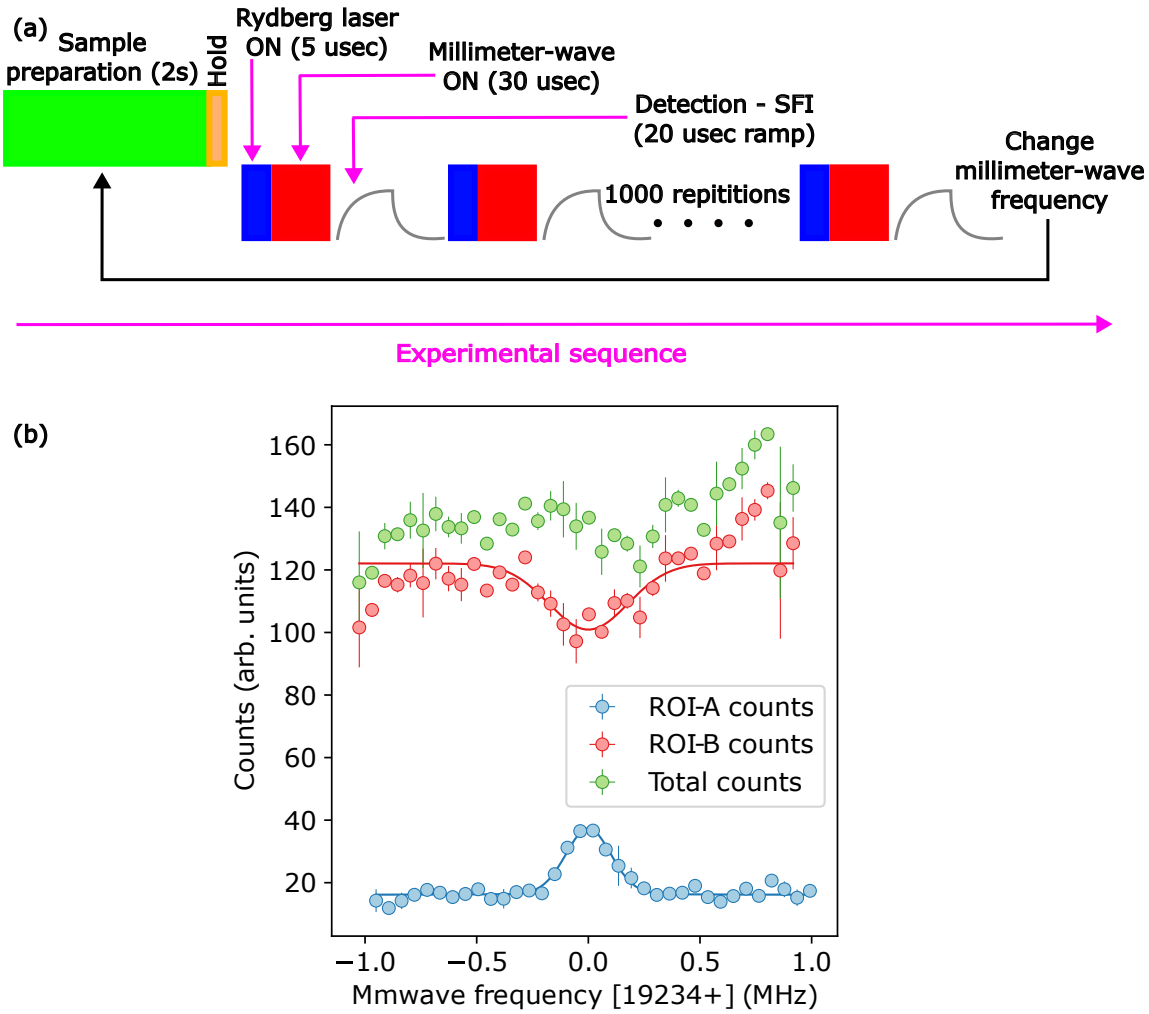

Figure 3.4 : (a) Experimental sequence of the SFI-ROI scheme. (b) Spectra of $(5s58s)\,^3S_1 \longrightarrow (5s58p)\,^3P_0$ transition. The counts in the state-defined ROIs (A and B) are plotted against the frequency of mm-wave radiation. At a near-resonant frequency, counts appear in ROI-A corresponding to the Rydberg-Rydberg transition to $(5s58p)\,^3P_0$-state. The total counts (green circles) is the total number of Rydberg atoms (either in $S-$ or $P-$ state) in the sample.

Let the state of a Rydberg atom dressed by near-resonant mm-wave radiation at a time t be denoted as $|\Psi(t)\rangle$, where,

$$|\Psi(t)\rangle = c_A(t)\,|A\rangle + c_B(t)\,|B\rangle \tag{3.1}$$

such that,

$$|c_A(t)|^2 + |c_B(t)|^2 = 1 \tag{3.2}$$

The amplitudes $c_A(t)$ and $c_B(t)$ are complex valued, where, $|c_A(t)|^2$ and $|c_B(t)|^2$ give the population in state $|A\rangle$ and $|B\rangle$ respectively. In the SFI spectra, the signal in ROI-A and ROI-B are proportional to $|c_A(t)|^2$ and $|c_B(t)|^2$ respectively. The proportionality factor is dependent on the detection efficiency of the ionized Rydberg electrons and is constant.

The dynamics of state $|\Psi(t)\rangle$ is governed by the Schrodinger's equation, where the Hamiltonian contains a term for the atom and a term for the interaction of the atom with radiation. The strength of the interaction is controlled by the mm-wave field ($\vec{E}$) and the transition dipole moment of the atom ($\vec{d}_{AB}$), and is denoted by a Rabi frequency (Ω_{AB}) defined as:

$$\Omega_{AB} = \frac{\vec{d}_{AB}.\vec{E}}{\hbar} \tag{3.3}$$

The state of the atom oscillates between the two states as a function of time where the rate of oscillation depends on the magnitude of Rabi frequency. The population of state $|B\rangle$ can be written as:

$$|c_2(t)|^2 = \frac{\Omega^2}{\Omega^2 + \delta^2}\left(\frac{1}{2} - \frac{1}{2}cos(\sqrt{\Omega^2 + \delta^2}t)e^{-t/\tau}\right) \tag{3.4}$$

δ is the detuning from the resonant frequency and τ is the coherence time. Such an oscillation is shown in fig. 3.5 between $(5s58s)\,^3S_1$ and $(5s58p)\,^3P_0$ states, where, the data is fit to eq. (3.4) to determine the magnitude of Ω_{AB} and the value of coherence time (τ). Coherence time accounts for the decaying amplitude for oscillation and describes a stretch of time when the relative phases of the states is coherent. Decoherence is introduced into the system by external factors such as stray electric or magnetic fields, resulting in the scrambling of relative phase.

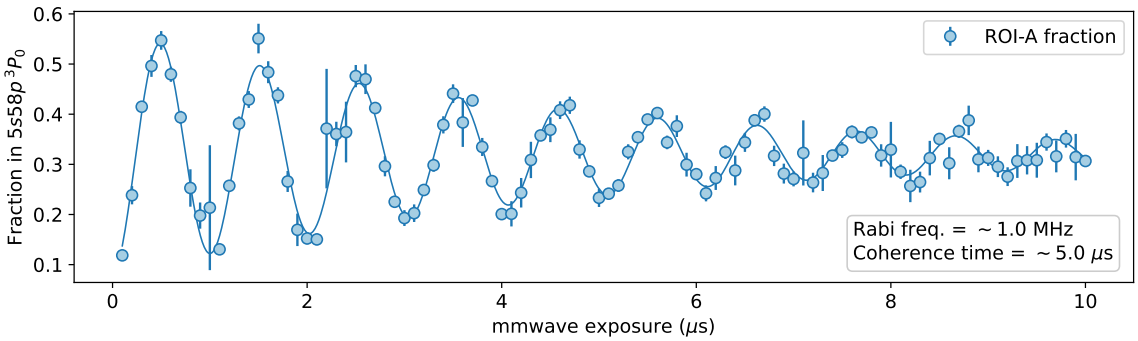

Figure 3.5 : Rabi oscillation observed for the transition $(5s58s)\,^3S_1 \longrightarrow (5s58p)\,^3P_0$.

Autler-Townes(AT) scheme

Autler-Townes effect[73] is the splitting of a transition addressed by weak probe field, when one of the two states is coupled to a third state by a strong near-resonant field. Figure 3.6 provides a schematic of the phenomena. The Rydberg transition is the weak probe field in this case, which addresses the Rydberg state $|A\rangle$. Let the resonant frequency between $|G\rangle$ and $|A\rangle$ be denoted by ω_0. In the presence of strong near-resonant mm-waves coupling nearby Rydberg states $|A\rangle$ and $|B\rangle$, the Rydberg transition energy splits into two, where, the new resonant frequencies are given by $\omega_0 - \Omega_{AB}$ and $\omega_0 + \Omega_{AB}$. Ω_{AB} is the Rabi frequency of the mm-wave coupling.

Rydberg laser is first scanned to determine the resonance frequency (ω_0) of the unperturbed Rydberg state, i.e., in the absence of any mm-wave field. Autler-Townes scheme to find Rydberg-Rydberg transitions involves turning on the mm-waves at a particular frequency immediately after a cold sample of atoms is prepared. Rydberg laser tuned to ω_0 is then switched on for about 10 μs, followed by a SFI electric field ramp to detect any Rydberg atoms created. After every iteration, the mm-wave frequency is tuned to a new value. A schematic of the sequence is presented

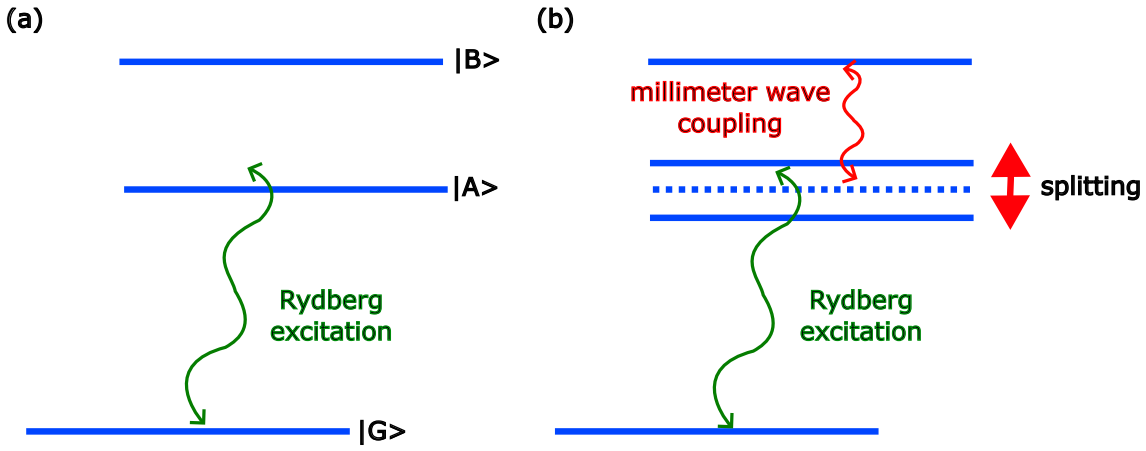

Figure 3.6 : (a) The green arrow denotes the two-photon Rydberg transition from the ground state ($|G\rangle$) to the unperturbed Rydberg state $|A\rangle$. (b) The Rydberg transition $|G\rangle \longrightarrow |A\rangle$ is split into two when $|A\rangle$ is strongly coupled to a higher lying Rydberg state ($|B\rangle$) via on-resonant mm-wave radiation. The stronger the coupling, the wider the split in energy. This splitting gradually vanishes as the mm-wave field drifts off-resonant from the $|A\rangle \longrightarrow |B\rangle$ transition frequency.

in fig. 3.7(a). A loss of Rydberg signal is observed when the mm-wave frequency is near resonance, due to Autler-Townes splitting of the Rydberg state and the Rydberg photon, with frequency ω_0, not being resonant to a Rydberg state anymore. A spectra is obtained by scanning the mm-wave frequency across resonance, as seen in fig. 3.7(b).

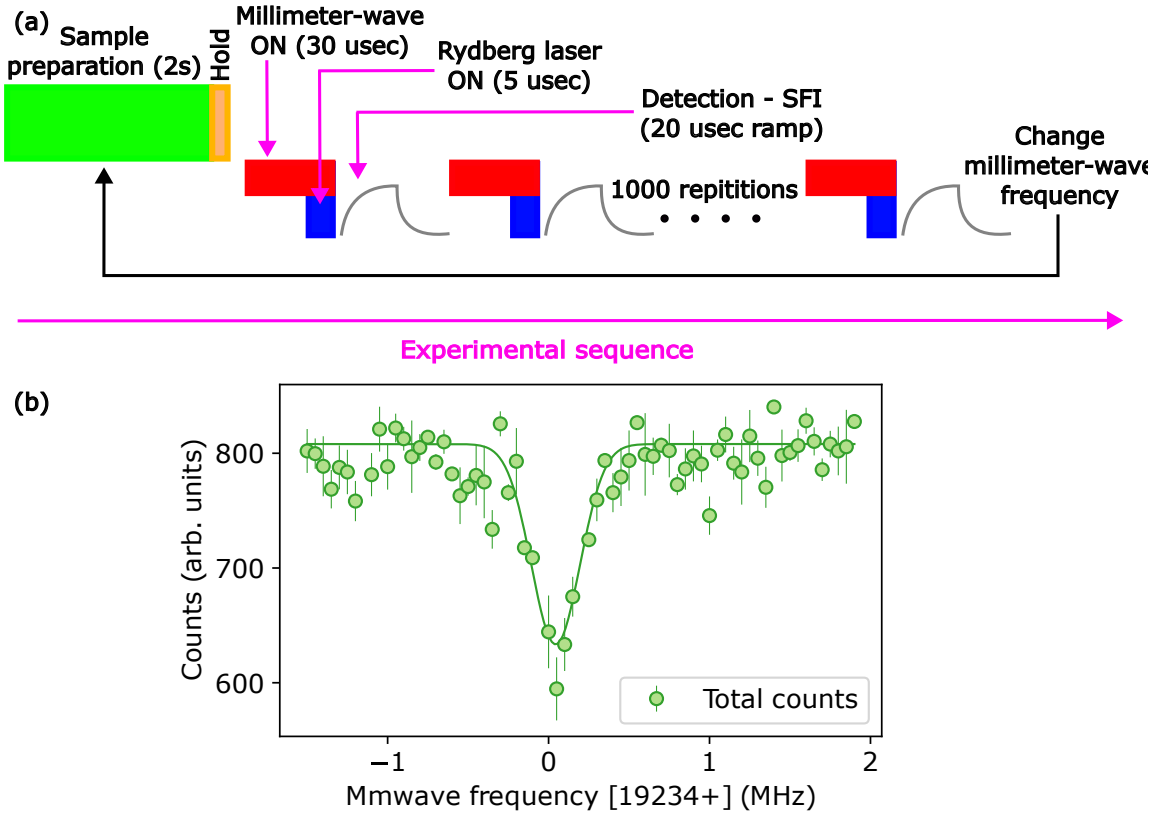

Figure 3.7 : (a) Experimental sequence of finding Rydberg-Rydberg transitions by Autler-Townes loss spectroscopy. (b) The loss of total Rydberg counts (green) is due to mm-wave frequency being near-resonant to $(5s58s)\,^3S_1 \longrightarrow (5s58p)\,^3P_0$ Rydberg-Rydberg transition. Resonance frequency is 19234.04(1) cm^{-1} with a linewidth of 150(10) kHz.

3.2.2 Resonant frequencies and quantum defect calculations

SFI-ROI and AT schemes were employed to find a number of $S-S$, $S-P$ and $S-D$ Rydberg-Rydberg transitions. Due to the precision of the mm-wave synthesizer, the measured resonance frequencies (ν_{observed}) were used to estimate the n-dependent quantum defects for various states more accurately. For the two-photon $(5sn_1s)\,^3S_1 \longrightarrow (5sn_2s)\,^3S_1$ transitions ($n_1 > n_2$), the following equation determines

the value of $^3S_1$ quantum defect (δ_{calc}):

$$h\nu_{\text{observed}} = \frac{R_y^{84}}{(n_2 - \delta_{\text{calc}})^2} - \frac{R_y^{84}}{(n_1 - \delta_{\text{calc}})^2} \tag{3.5}$$

The quantum defect values (δ_{calc}) of ^3P_j states in $(5sn_1s)\,^3S_1 \longrightarrow (5sn_2p)\,^3P_j$ type transitions is given by:

$$h\nu_{\text{observed}} = \frac{R_y^{84}}{(n_2 - \delta_{\text{calc}})^2} - \frac{R_y^{84}}{(n_1 - \delta_{n_1,0,1})^2} \tag{3.6}$$

R_y^{84} is the Rydberg constant for ^{84}Sr and $\delta_{n_1,0,1}$ is the quantum defect of the $^3S_1$ state [obtained from eq. (3.5)]. The transitions, the measured resonant frequencies and the calculated quantum defects for each of the transitions are presented in the table below.

n_1	l_1	j_1	n_2	l_2	j_2	δ_{lit}	$\nu_{\text{predicted}}$ (MHz)	ν_{observed} (MHz)	δ_{calc}
58	0	1	57	0	1	3.37022	41492.443106	41494.265187	3.37017
59	0	1	58	0	1	3.37021	39274.990284	39276.615123	3.37017
60	0	1	59	0	1	3.37020	37212.776836	37214.291047	3.37016
56	0	1	56	1	0	2.88676	21521.987992	21501.073508	2.88723
57	0	1	56	1	0	2.88676	22358.034823	22380.690078	2.88727
57	0	1	57	1	0	2.88675	20345.505441	20325.757764	2.88723
58	0	1	57	1	0	2.88675	21146.937665	21168.460860	2.88727
58	0	1	58	1	0	2.88674	19253.234059	19234.375308	2.88722
59	0	1	58	1	0	2.88674	20021.756225	20041.718182	2.88725
59	0	1	59	1	0	2.88674	18237.771892	18220.137603	2.88721
60	0	1	59	1	0	2.88674	18975.004944	18994.461079	2.88726

Table 3.1 : Transition frequencies measured by mm-wave spectroscopy of ^{84}Sr atoms. Initial ($i = 1$) and final ($i = 2$) states are labeled by principal, orbital angular momentum quantum number and total angular momentum quantum numbers(n_i, l_i, j_i). The literature value of quantum defects (δ_{lit}) obtained from [23] are used to calculate $\nu_{\text{predicted}}$. The value of Rydberg constant used for ^{84}Sr is 109736.598 cm^{-1}. Eq. (3.5) and (3.6) are used to calculate the new quantum defects (δ_{calc}) using the values of ν_{observed}.

3.3 Coherence times in the apparatus: Trends

Coherence is a desired property which quantifies the degree of "quantumness" of any quantum mechanical system. It is characterized by a "coherence time", denoted by τ. This defines a stretch of time in which the relative phases of a quantum superposition state can be defined with reasonable accuracy. Several factors in an experiment can introduce noise in the phases resulting in the loss of coherence among the states, and hence, resulting in an uninteresting system describable by statistics only. Here, we present measurements of coherence time in our apparatus through Rabi oscillations. Equation (3.4) describes the population of the excited state as a function of time, where, the loss of coherence is incorporated by an exponential factor containing coherence time (τ) as an argument. The amplitude of oscillation does not decay in a perfectly coherent system. But in real systems, like this experiment, the loss of coherence is reflected in the decay of the sinusoidal oscillations with time.

We observe dependence of the coherence time on two main factors.

3.3.1 Intensity dependence

The coherence time seems to depend on the magnitude of the Rabi frequency($\propto$ intensity), with higher Rabi frequencies resulting in lower coherence times. This puts a practical limit on the duration of coherent evolution of a quantum state created in the apparatus. Figure 3.8 plots Rabi oscillations obtained by varying the mm-wave intensity on the atoms. The coherence time is determined by fitting the oscillation data to eq. (3.4) and is plotted against Rabi frequency.

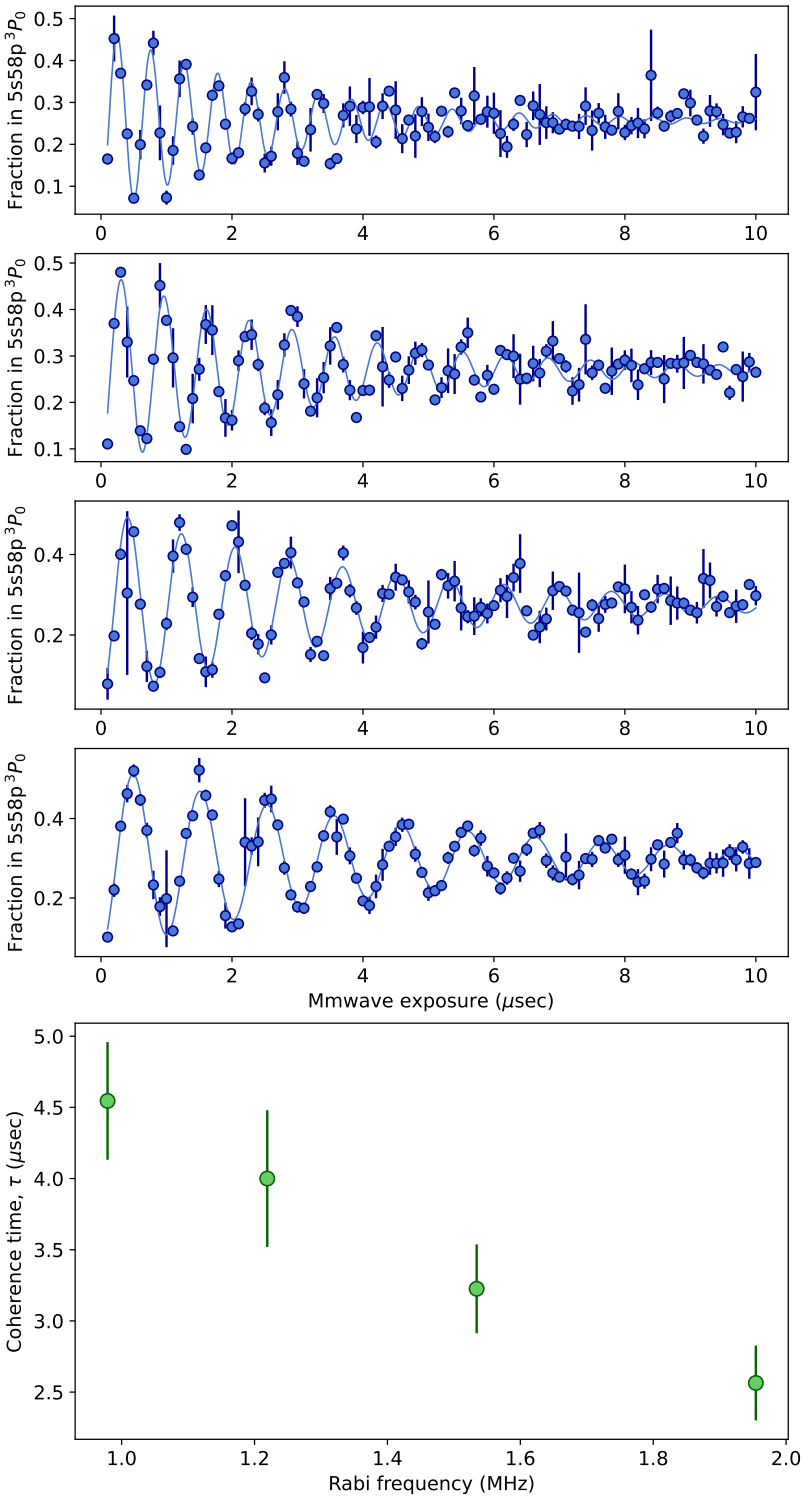

Figure 3.8 : Rabi oscillations for different mm-wave intensities. The coherence time extracted by fitting data to eq. (3.4) is plotted against Rabi frequency in the bottom panel. Lower coherence times at higher Rabi frequencies is observed.

3.3.2 Magnetic field dependence

We also see a dependence of coherence time on the presence of magnetic field on the atoms. This may originate from the stability of the field strength at the location of atoms. A current supply controls the current through the coils producing a magnetic field, and hence, the ripple noise on the current source translates to a time-varying magnetic field strength. A 30 kHz Zeeman broadening on the $^3S_1 - {}^3P_0$ transition is estimated from the specifications of the supply and the magnetic susceptibility of the magnetically-sensitive $^3S_1$ Rydberg state, which corresponds to about 5 μs in the time domain. This issue, however, can be circumvented by addressing magnetic-field-insensitive quantum states or quantum states with similar magnetic field dependence. Coherence time obtained from Rabi oscillations on a magnetic-field-insensitive two-photon $(5s60s)\,^3S_1 \longrightarrow (5s61s)\,^3S_1$ transition at various magnetic fields is plotted in figure 3.9. The dependence is in contrast to the magnetic-field-sensitive $(5s58s)\,^3S_1 \longrightarrow (5s58p)\,^3P_0$ transition plotted in figure 3.10.

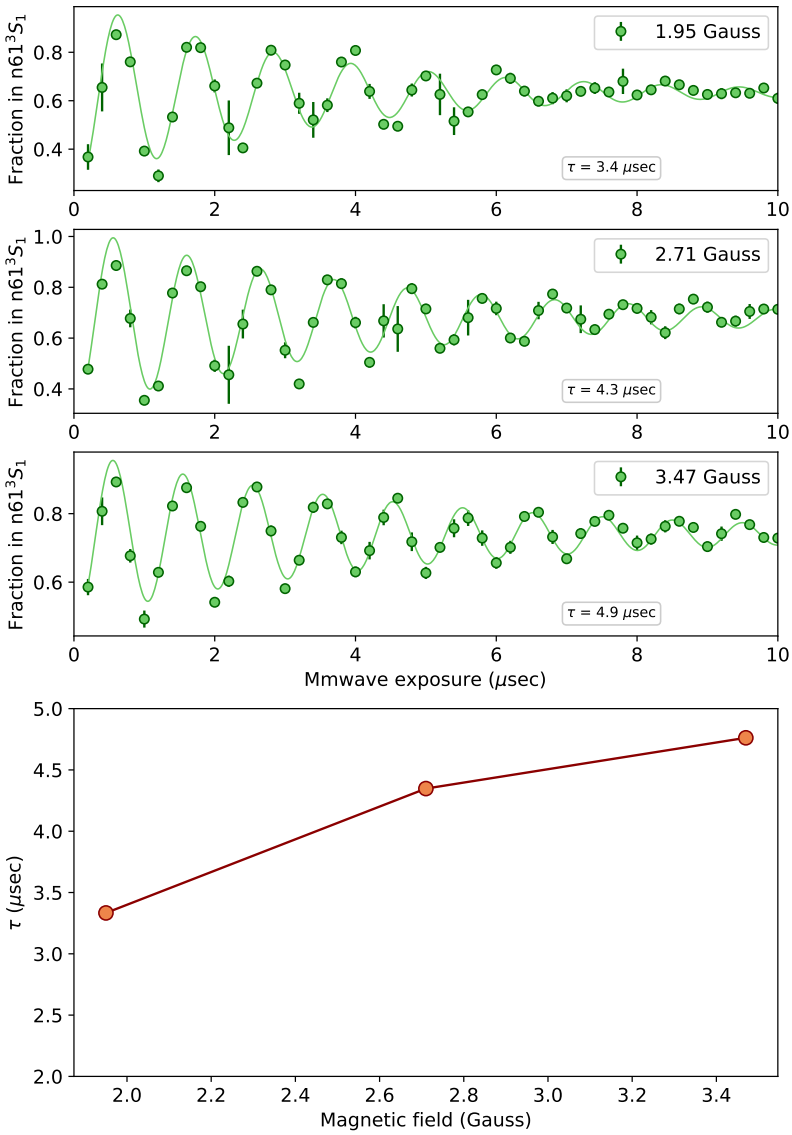

Figure 3.9 : Coherence time of magnetic-field-insensitive Rydberg-Rydberg transition $((5s60s)\,^3S_1 \longrightarrow (5s61s)\,^3S_1)$ as a function of magnetic field on atoms.

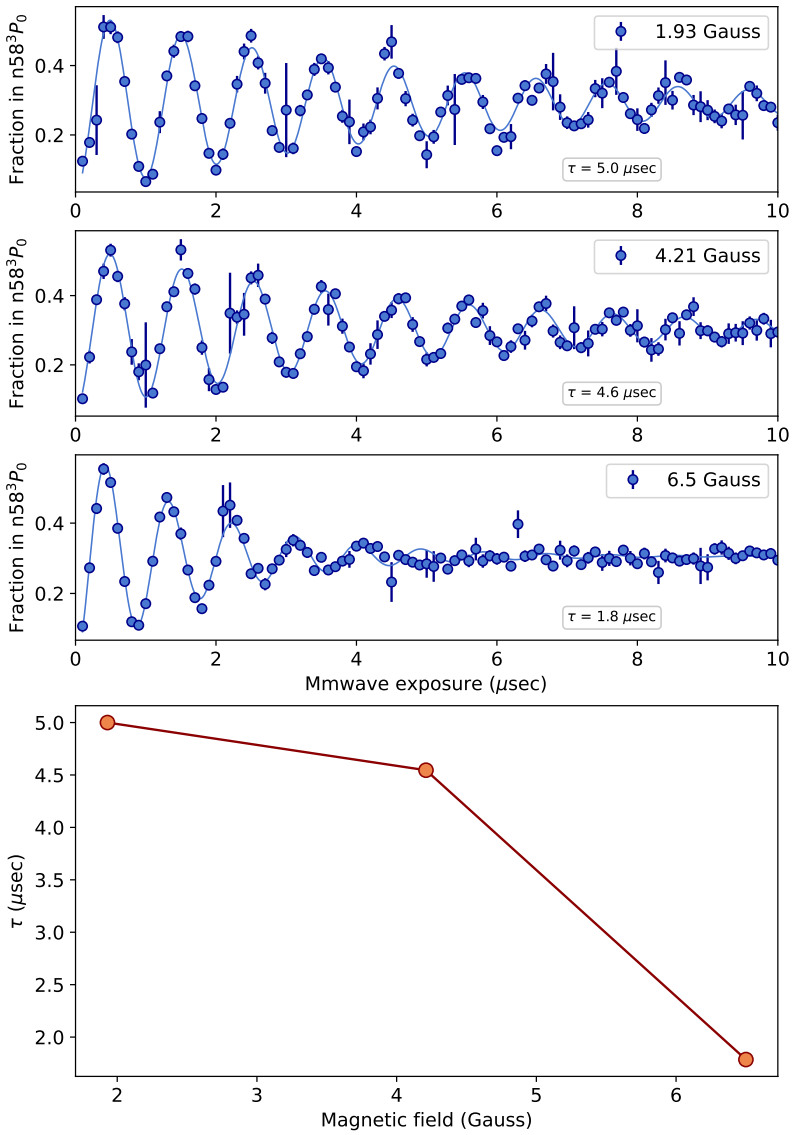

Figure 3.10 : Coherence time of magnetic-field-sensitive Rydberg-Rydberg transition $((5s58s)\,^3S_1 \longrightarrow (5s58p)\,^3P_0)$ as a function of magnetic field on atoms.

While we do not understand in detail about the behavior of coherence times in our apparatus, the Rabi oscillation measurements show that a we can maintain coherence up to a reasonable time to study the equilibrium states of the simulated Hamiltonian. The interaction of Rydberg atoms with photons are of the order of few microseconds

in our apparatus and hence is within the coherence time measured. This will not affect the interpretation of data and the observation of topological behavior.

Chapter 4

Publication: SSH model on Rydberg atomic states

4.1 Mapping lattice sites to Rydberg atomic states

Rydberg atomic states are a new platform for synthetic dimension experiments, where the Rydberg states are interpreted as lattice sites in a synthetic space. The tunneling between lattice sites is mapped to the coupling strength between the Rydberg states achieved by resonant electromagnetic radiation and characterized by the Rabi frequency. This idea is based on a recent proposal, where closely spaced rotational states of ultracold polar molecules provide a synthetic dimension for quantum simulation[45]. Rydberg atomic states at high principal quantum number (n) present an analogous system, but without the complexity of cooling molecules. They are much simpler to work with experimentally as they possesses a number exaggerated properties, such as huge transition matrix elements, which scale as $(n-\delta)^2$, where δ is the quantum defect of a given state. The energy spacing between levels scales as $(n-\delta)^{-3}$, which means, at sufficiently high n, Gigahertz frequencies are capable of coupling nearby Rydberg levels. This allows one to exploit the already well established mm-wave technology, which brings precise frequency tunability and phase stability. In contrast to needing several lasers to address different couplings at a given time, radiation in the GHz regime can simply be combined together with commercially available frequency combiners to expand the size of the realized synthetic dimension. The power of Rydberg-atom synthetic dimension lies in the exquisite control over connectivity,

tunneling rates and on-site potentials via frequency and phase tuning, which opens up the possibility of creating systems not realizable in physical space. Rydberg atoms also offer the possibility of creating tunable, localized interactions for many-body systems in the synthetic space, which is a challenge for other atom-based platforms.

Our proposal to implement strontium Rydberg states as synthetic lattices is shown in fig. 4.1. We couple neighboring triplet states in ^{84}Sr, i.e. $^3S_1$ and $^3P_0$ states, by mm-waves to realize the SSH Hamiltonian. A brief discussion of the SSH is presented next before diving into the implementation and the experimental results.

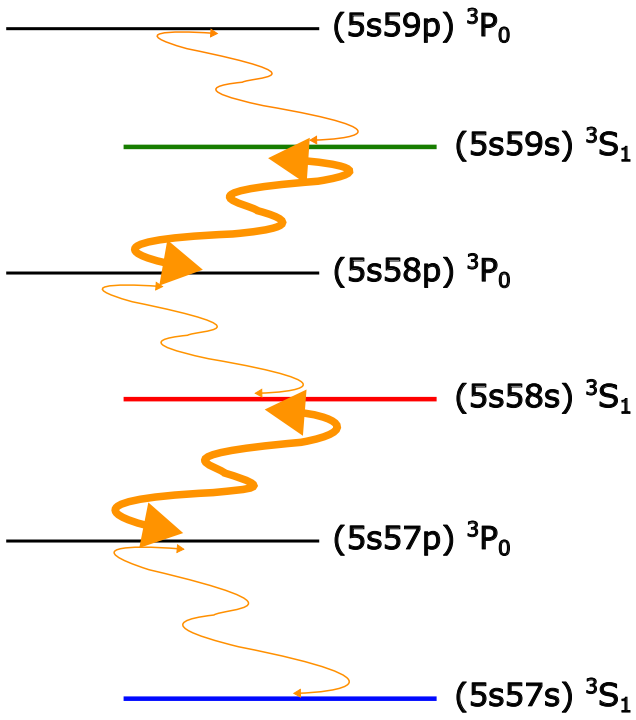

Figure 4.1 : Millimeter-wave coupled strontium Rydberg states to realize the SSH model. The double-headed wavy orange arrows denote the mm-wave coupling radiation, corresponding to the tunneling rate in the SSH Hamiltonian. Thicker wavy arrows highlight stronger coupling and hence greater tunneling. The red, blue and green lines are $^3S_1$ states. These states are color coded to identify Rydberg spectra in the corresponding manifolds. The black lines are $^3P_0$ states.

4.2 A brief history of the SSH model

The decade of the 1970s witnessed huge growth and excitement in to understanding numerous condensed matter phenomena, embodied in the seminal essay by P.W. Anderson, titled "More is different"[48]. Fundamental physics was not dominated by the journey into smaller and smaller length scales to unravel the mysteries of basic constituents of matter, but, there was new and exciting fundamental physics to be discovered at every scale. For example, lattice and many-body physics became the major line of interest for many physicists. Techniques such as doping, controlling electron transport properties in solids and the effect of fields on phases of matter[74] contributed to the enigma of condensed matter physics. One such mystery in the early days lied in the simplest of lattice systems, a 1-D chain, particularly long conjugated polymers like polyacetylene. The governing dynamics of the electron hopping along the 1-D polymer captured the interest of many and it was not until 1979 that there was a working theory to describe the phenomena. Su, Schrieffer and Heeger proposed the now famous SSH model in 1979[19], to elucidate the dynamics of single electron on a chain with staggered bond structure. The theory assumes zero on-site potential and spinless particles without interactions. Even with such simplifications, it exhibits rich topological physics. Figure 4.2(a) shows an example of a 1-D molecule, taken from the original SSH paper. The SSH chain has two phases, the topological [4.2(b)] and trivial phases [4.2(c)] parameterized by the bond strength. The alternative strong and weak bonds resulting in a weak bond to the edge of the molecule bodes the topologically relevant phase which allows for the existence of topologically-protected edge states (TPS), which are robust against perturbations respecting the inherent chiral symmetry of the 1-D chain. In this context, chiral symmetry refers to the absence of any terms in the Hamiltoniian that connects A-sites to A-sites, or B-sites

to B-sites. Here is a brief discussion on the mathematics of the SSH model.

4.2.1 1-D topological chain

We assume a finite 1-D chain with 2N sites where the two sublattices (A and B) each contain N sites. The hopping amplitudes are assumed to be real and non-negative and are denoted by j_s and j_w, with $j_s > j_w$. There is no on-site potential or a spin degree of freedom and hence, the particles are spinless for all purposes. The Hamiltonian can then be written as:

$$\hat{H} = j_w \sum_{n=1}^{N} (|n, B\rangle \langle n, A| + h.c.) + j_s \sum_{n=1}^{N-1} (|n+1, A\rangle \langle n, B| + h.c.) \tag{4.1}$$

Here, the state of an electron is given by the index of the unit cell and sublattice. $|n, A\rangle$ means the electron is at the n^{th} unit cell on the sublattice A. A basis set for the Hilbert space spanned by the Hamiltonian is given as:

$$\mathcal{B} : (|1, A\rangle, |1, B\rangle, |2, A\rangle, |2, B\rangle, ...) \tag{4.2}$$

Each basis vector is a direct product of the basis vector in the subspace spanned by index n and the basis vector in the sub-space spanned by the set, [A,B]. There is translation invariance over the unit cells (n) in the chain and hence Bloch's theorem can be applied to write the eigenstate in the subspace of unit cells as:

$$|k\rangle = \frac{1}{\sqrt{N}} \sum_{n=1}^{N} e^{ink} |n\rangle, \tag{4.3}$$

where, n denotes the unit cell index. The wavefunction inside the unit cell in the momentum-space representation is written as:

$$|\psi_n(k)\rangle = a_n(k) |A\rangle + b_n(k) |B\rangle, \tag{4.4}$$

where, $a_n(k)$ and $b_n(k)$ are the amplitudes of $|A\rangle$ and $|B\rangle$ in the n^{th} unit cell respectively. The total eigenstate wavefunction now is a direct product of the two subspace wavefunctions. It is given as:

$$|\Psi_n(k)\rangle = |k\rangle \otimes |\psi_n(k)\rangle \tag{4.5}$$

One can expand eq.(4.5) to write in terms of the basis vectors in $\mathcal{B}$ and substitute in the Schrodinger's equation to get the following:

$$\begin{pmatrix} 0 & j_w & 0 & 0 & 0 & 0 \\ j_w & 0 & j_s & 0 & 0 & 0 \\ 0 & j_s & 0 & j_w & 0 & 0 \\ 0 & 0 & j_w & 0 & j_s & 0 \\ 0 & 0 & 0 & j_s & 0 & j_w \\ 0 & 0 & 0 & 0 & j_w & 0 \end{pmatrix} \begin{pmatrix} a(k)e^{ik} \\ b(k)e^{ik} \\ a(k)e^{2ik} \\ b(k)e^{2ik} \\ a(k)e^{3ik} \\ b(k)e^{3ik} \end{pmatrix} = E(k). \begin{pmatrix} a(k)e^{ik} \\ b(k)e^{ik} \\ a(k)e^{2ik} \\ b(k)e^{2ik} \\ a(k)e^{3ik} \\ b(k)e^{3ik} \end{pmatrix} \tag{4.6}$$

On equating the terms in the left-hand side and the right-hand side, we get a set of two coupled equations. In matrix notation it is given by:

$$\begin{pmatrix} 0 & j_w + j_s e^{-ik} \\ j_w + j_s e^{ik} & 0 \end{pmatrix} \begin{pmatrix} a(k) \\ b(k) \end{pmatrix} = E(k). \begin{pmatrix} a(k) \\ b(k) \end{pmatrix} \tag{4.7}$$

The eigenenergies obtained by diagonalizing the above matrix are,

$$E(k) = \pm\sqrt{j_w^2 + j_s^2 + 2j_w j_s cos(k)} \tag{4.8}$$

The gap in energy between the two bands is given by 2Δ where, $\Delta = j_s - j_w$. It is interesting to note that for $j_s = j_w$, there is no band gap, and the molecule behaves as a conductor. A band gap is present when the bonds are staggered.

There are six eigenstates for the Hamiltonian described in eq. (4.6). Figure 4.2(d) and (e) plot these eigenstates in terms of the basis vectors in $\mathcal{B}$ for the two relevant

configurations. Figure 4.3(b) plots the eigen-energies for various ratios of strong to weak coupling across the phase transition boundary, depicted in fig. 4.3(c).

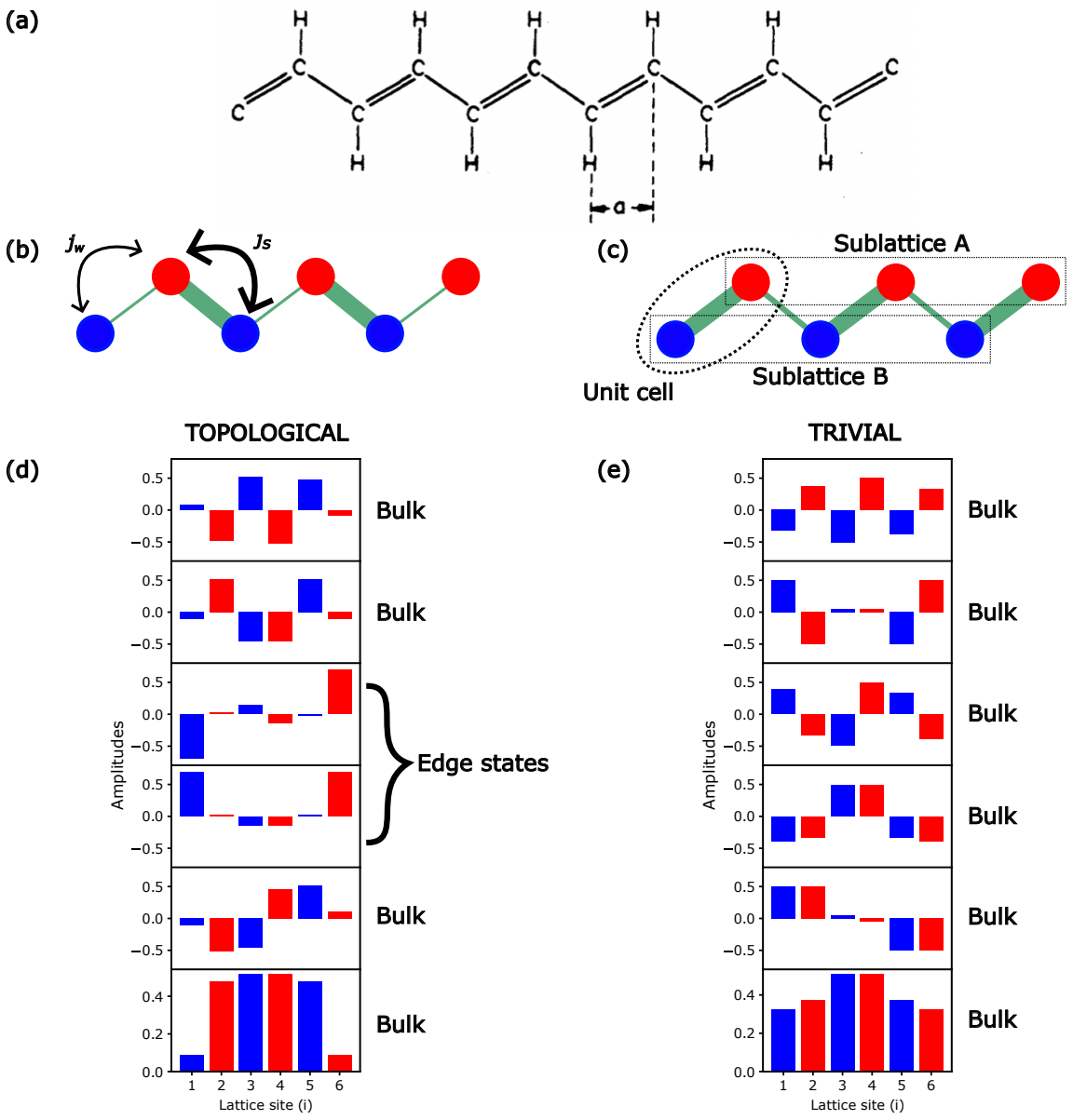

Figure 4.2 : (a) A 1-D polymer (such as a Polyacetylene molecule) showing the staggered bond pattern[19]. (b) Topological configuration of the SSH model with weak coupling to the edge sites that possesses TPS. The thick bonds denote strong tunneling (j_s), while the weak bonds denote weak tunneling (j_w). (c) Trivial configuration of the SSH model with strong tunneling to the edge sites. The set of red and blue lattice sites are denoted as sublattice A and B respectively. Each unit cell contains one lattice site each from A and B. (d) Eigenstates of the topological configuration with two edge states, which are symmetric and anti-symmetric superpositions of the left and right edges. The bulk states are superpositions of the bulk sites. (e) Eigenstates of the trivial configuration, where each eigenstate is a superposition of all the lattice sites. No TPS are present.

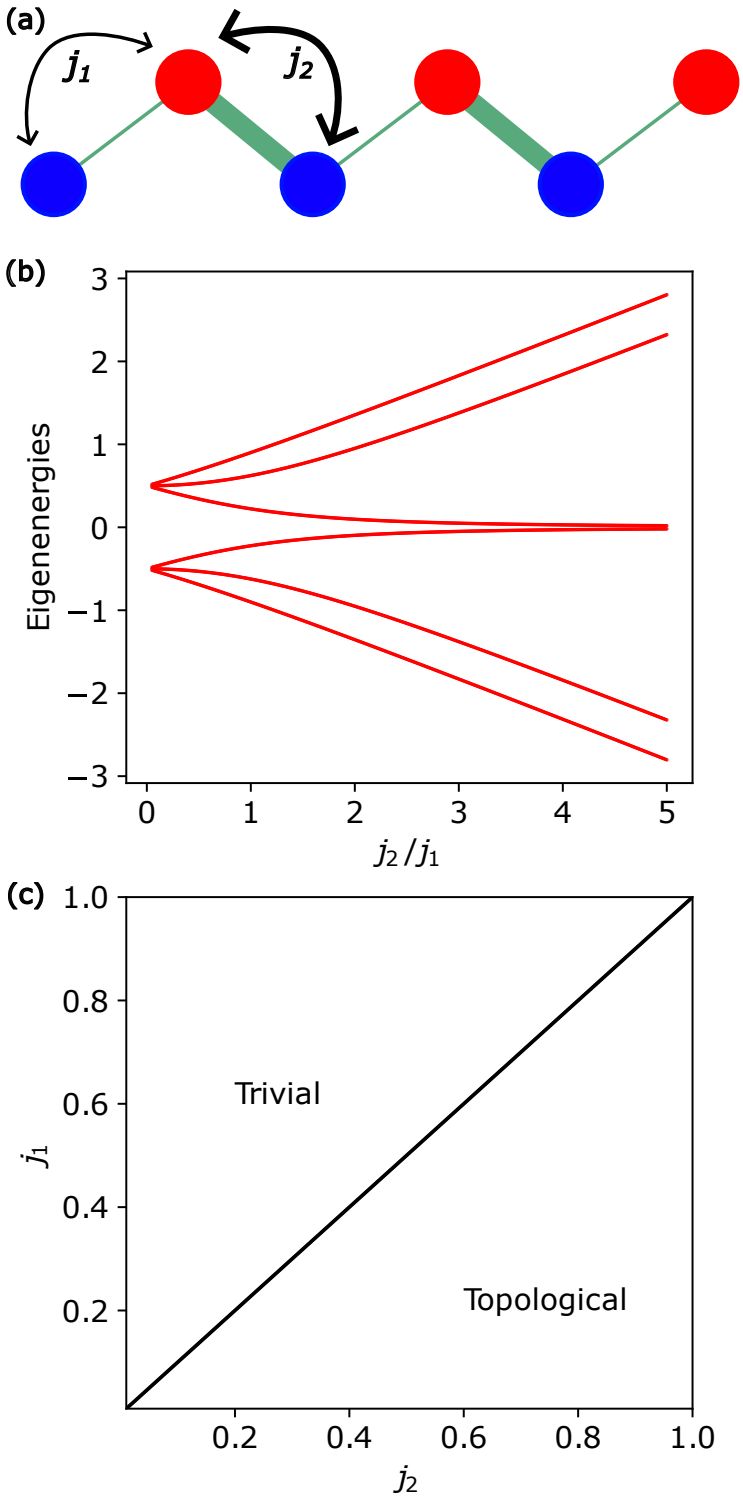

Figure 4.3 : (a) Six site SSH chain characterized by staggered tunneling amplitudes denoted by j_1 and j_2. (b) Band structure as a function of the tunneling ratio j_2/j_1. The edge states are realized with weak tunneling to the edges(i.e., $j_2/j_1 >> 1$), with their energies unperturbed and pinned to zero. (c) Phase diagram of the SSH model, where $j_1 = j_2$ separates the two phases.

4.2.2 Simulating SSH model - platforms

The SSH model is a paradigmatic example of a system which possesses several topological properties. Its simplicity as a 1-D chain along with the richness of physics it harbors has inspired numerous experiments to probe its topological behavior, and make it an attractive candidate for exploring new platforms for quantum simulation. For example, geometric Zak phases, which describe the underlying topological character of the bloch bands in solids, have been measured with the SSH model realized on 1-D optical superlattices[75]. Another famous topological phenomena, Thouless charge pumping, has also been demonstrated by implementing the SSH Hamiltonian in a phase controlled optical superlattice[76]. Newer systems based on optical tweezer techology, have realized SSH physics with trapped Rydberg atoms, where hopping is realized by dipolar exchange interactions[77].

Synthetic dimensions, realized on internal or external degrees of freedom, are powerful platforms to simulate topological rich Hamiltonians, such as the SSH model. A synthetic dimension based on magnetic sublevels was recently utilized to implement a "virtual" 1-D lattice to study the SSH Hamiltonian[78]. Raman transitions were employed for hopping between sites. Another experiment realized the SSH model on the momentum-states of a BEC, where tunneling between lattice sites was achieved via Bragg transitions[46, 79], for the study of single particle transport properties in the SSH regime.

Inspired by the traditional SSH model, many variations of the Hamiltonian have been explored. For example, the SSH4 model, where an unit cell contains four lattice sites (instead of 2 as in SSH)[80] was studied on momentum-states based synthetic lattice to understand its topological phase transitions. Other experiments have included particle interactions, on-site potentials, long-range hopping[11] and periodic

modulations of tunneling[81] to study additional topological behavior.

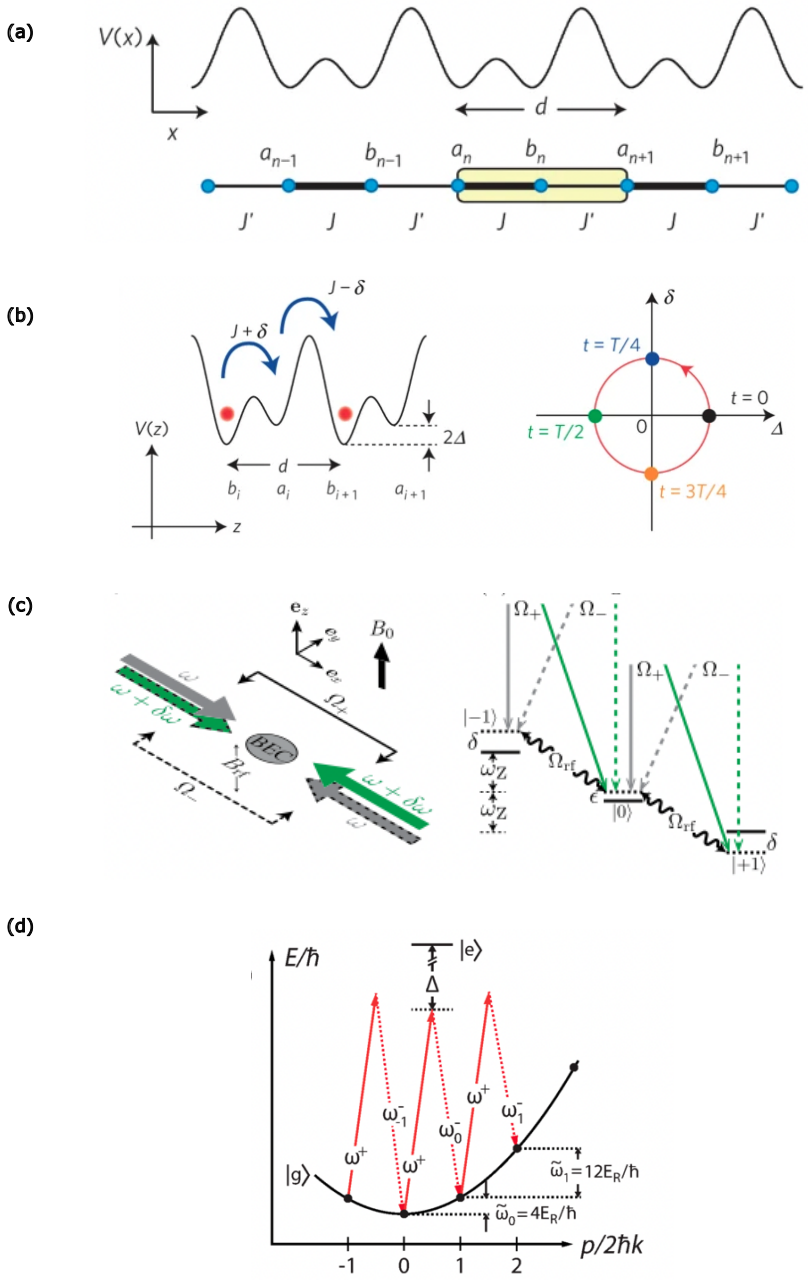

Figure 4.4 : (a) 1-D superlattice used (by I. Bloch group, MPQ, Germany) to measure the Zak phase difference between the topological and trivial phases of the SSH model[75]. (b)The SSH model with an on-site potential term, called the Rice-Mele model, realized with 1-D superlattices to implement a fermionic Thouless pump (shown on the right)[76]. (c) Magnetic sublevels used as a synthetic dimension where tunneling is realized by Raman transitions to realize the SSH model with on-site potentials (Spielman group, JQI, Maryland)[78]. (d) Bragg transitions used to realize tunneling between momentum states in a BEC (Gadway group, University of Illinois at Urbana-Champaign) to implement the SSH model[46, 79].

4.3 Six-site SSH model on the Rydberg atom

Figure 4.1 provides a schematic about the implementation of the SSH model using strontium Rydberg states. A careful consideration of the full spectrum of energy levels is important to evaluate the chances of encountering an accidental degeneracy. A degeneracy occurs when a photon of given frequency is resonant (or near-resonant) with multiple transitions. Such a degeneracy is undesirable because it changes the system under study, and thereby, morphing the equilibrium quantum states realized on it. Also, a quantum simulation involving evolution of an initial quantum state to a final quantum state may have unintended dephasing by the introduction of non-negligible perturbation terms in the modeled Hamiltonian.

4.3.1 Proximity of $S-P$ transitions

In ^{84}Sr the triplet $P-$state lies roughly in the middle of two triplet $S-$states. Moreover, there are triplet $D-$states in the vicinity that can be driven by two photons in the K-band. In order to compare between the photon energies, figure 4.5 plots the difference in photon energies of various $^3S_1 - {}^3P_j$ transitions (j = 0,1 and 2) from other $S-P$, $S-S$ and $S-D$ type transitions. It is seen that $^3S_1 - {}^3P_0$ transition avoids any accidental resonances in the K-band. Other $^3S_1 - {}^3P_j$ transitions are degenerate with at least one other transition in the range of interest. Moreover, for the $^3S_1 - {}^3P_0$ transition, the closest photon energies are separated by $\sim$100 MHz, which is much greater than the Rabi couplings ($\sim$ few MHz) in this experiment. Thus, a $^3S_1 - {}^3P_0$ is a natural candidate for a single-photon transition to implement a synthetic lattice, where tunneling is realized with mm-wave coupling of strontium Rydberg states.

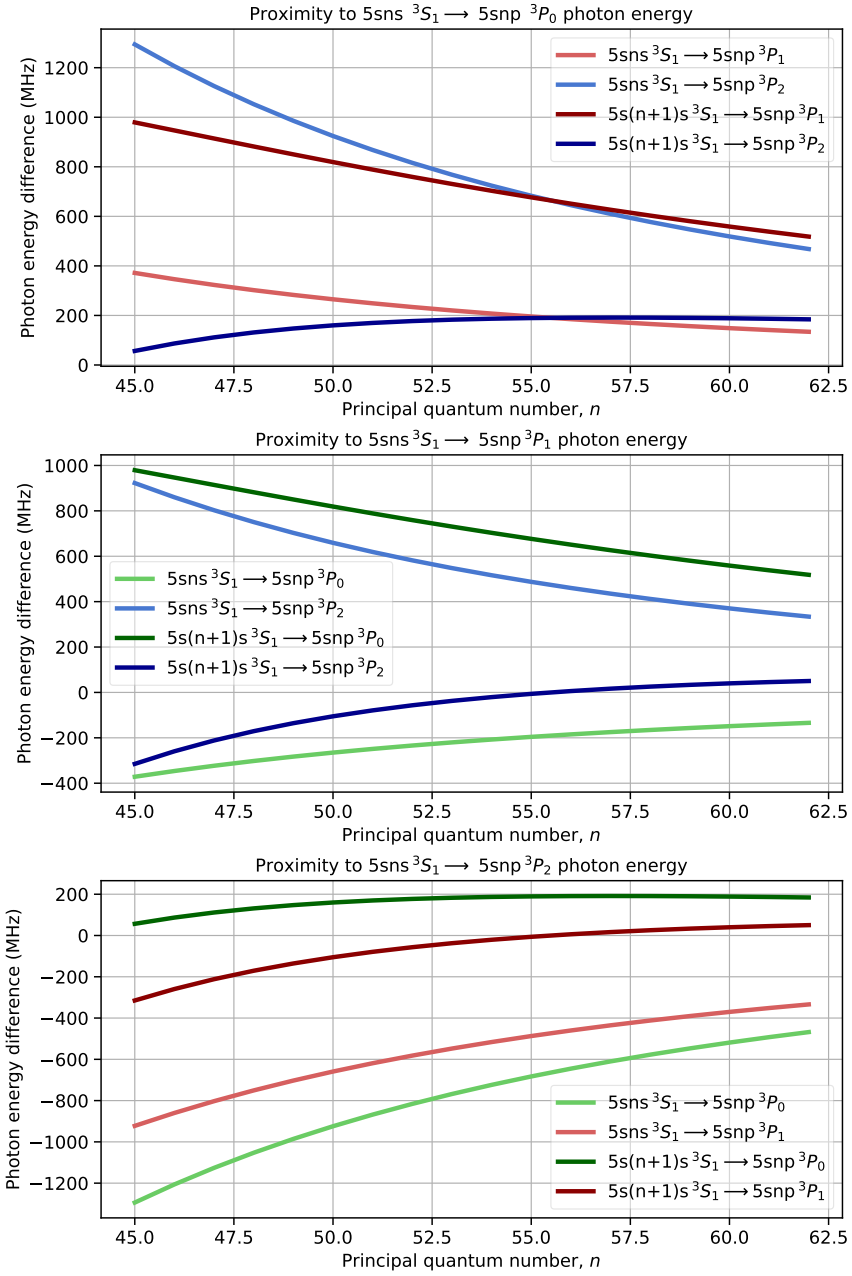

Figure 4.5 : Plotting the difference of the photon energy of transition in the title of each panel with the transitions in the legend. The photon energies for all the transitions in the range of quantum numbers presented in the figure lie in the K-band. Only the $^3S_1 - {}^3P_0$ transition avoids any accidental resonances, i.e., no zero-crossings.

4.3.2 AC stark effect

Another important aspect of coupling Rydberg levels by radiation is the shifting of resonance energy due to the presence of radiation itself. This manifests as the AC stark effect, where radiation interacts with an atom through its electric dipole moment and shifts its energy levels. The unperturbed Rydberg states described in this thesis possess no permanent dipole moment due to the symmetry of the electronic orbitals and therefore, the first order correction to energy, given by perturbation theory[69], is zero. The second order correction to energy is characterized by the transition dipole moment between the Rydberg levels and is non-zero, where, the shift in energy of a Rydberg level due to a coupling field of amplitude E can be written as:

$$\Delta E_{nlj} = -\frac{1}{4}\alpha_{nlj}E^2 \,(\propto \text{Intensity of mm-waves}) \tag{4.9}$$

where, ΔE_{nlj} gives the energy shift for a state described by quantum numbers n, l and j, and α_{nlj} is its polarizability. Note, the Rabi frequency is proportional to E. Therefore, we expect the AC stark shift of a Rydberg state to be linearly proportional to Ω^2, where Ω denotes the Rabi frequency.

$S - P$ transitions

In order to create a synthetic dimensions with $^3S_1 - {}^3P_0$ single-photon transitions, the AC stark shifts of each transition is explored using Autler-Townes effect. The Autler-Townes (AT) spectra for each of the $^3S_1 - {}^3P_0$ single-photon transition is obtained by scanning the 320 nm Rydberg photon in the two-photon Rydberg excitation scheme discussed in chapter 2. The Rabi frequency is obtained from the Autler-Townes splitting and is a measure of the intensity($\propto \Omega^2$) of mm-waves on the atoms. When the mm-waves are on resonance, both of the peak strengths in the AT spectra are

equal, whereas, they are unequal when mm-wave frequency is off-resonant. This asymmetry in peak heights can be used to estimate the detuning of the mm-waves from resonance. No other frequencies are present other than the one addressing the transition for such an experiment. The resonance frequencies for a range of mm-wave intensities on the atoms are recorded with this procedure.

The Hamiltonian describing the interaction of mm-waves with two Rydberg levels in the rotating frame under rotating-wave approximation can be written as:

$$\hat{H} = \begin{pmatrix} 0 & \Omega/2 \\ \Omega^*/2 & \delta \end{pmatrix} \tag{4.10}$$

where, δ is the detuning and Ω is the magnitude of Rabi frequency (* denotes the complex conjugate). The matrix is diagonalized to obtain the eigenenergies and eigenstates. These are plotted in fig. 4.6 for three typical values of Rabi frequencies used in the experiment (1, 2 and 5 MHz). Mathematically, they are given by:

$$E_{1,2} = \frac{\delta \pm \sqrt{\delta^2 + \Omega^2}}{2} = \frac{\delta \pm \tilde{\Omega}}{2} \tag{4.11}$$

where, E_1 and E_2 denote the eigenenergies of the two eigenstates and $\tilde{\Omega} = \sqrt{\delta^2 + \Omega^2}$ is the generalized Rabi frequency. The splitting between the two AT peaks is therefore $\tilde{\Omega}$. The two eigenstates are given as:

$$\begin{aligned} |1\rangle &= \sin\theta\,|e\rangle + \cos\theta\,|g\rangle \\ |2\rangle &= \cos\theta\,|e\rangle - \sin\theta\,|g\rangle \end{aligned} \tag{4.12}$$

where,

$$\tan\theta = \frac{\Omega}{\sqrt{\Omega^2 + \delta^2} - \delta} = \frac{\sqrt{\tilde{\Omega} + \delta}}{\sqrt{\tilde{\Omega} - \delta}} \tag{4.13}$$

In the AT spectra, the strength of the two peaks are equal to $\sin^2\theta$ and $\cos^2\theta$, and hence, eq. (4.13) can be solved for the value of δ. Figure 4.6(b) plots the strengths

of the two peaks as a function of detuning. A negative detuning results in a stronger right (higher in energy) peak, whereas, a positive detuning results in stronger left peak.

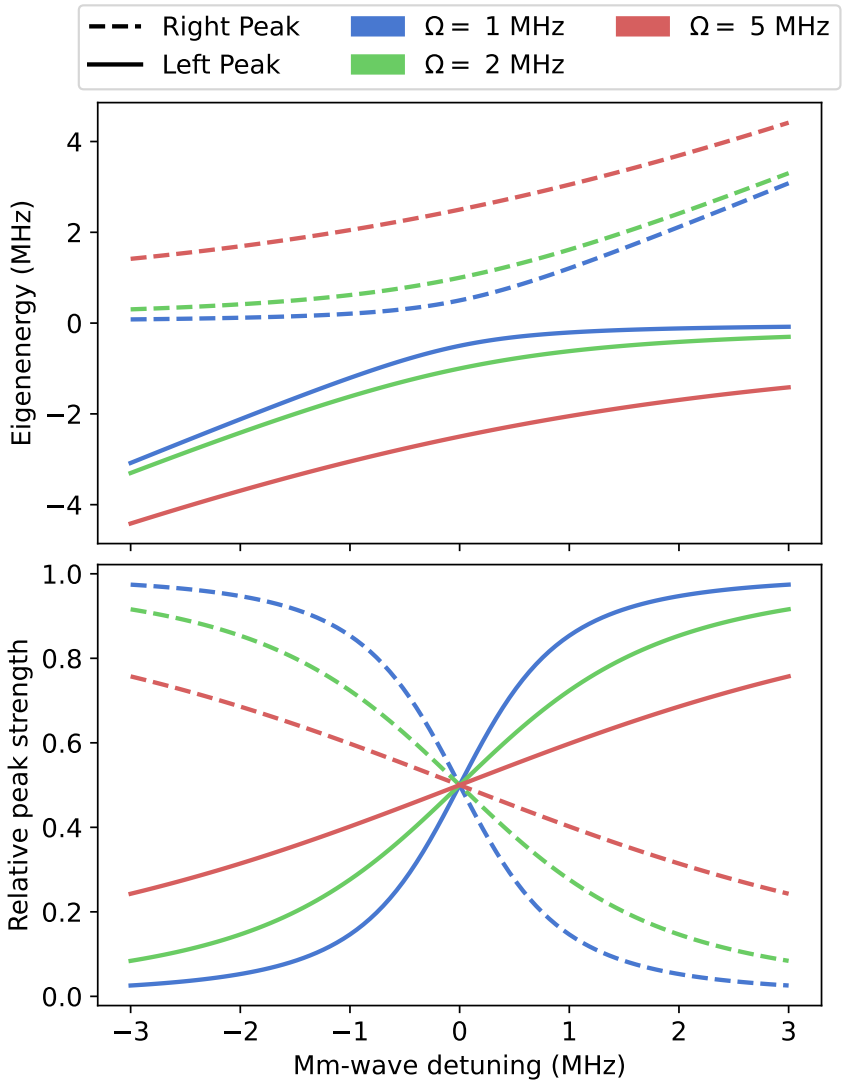

Figure 4.6 : (a) Eigenenergies (eq. 4.11) for the new eigenstates (seen in the AT spectra as two separate peaks), when the atom is dressed by near-resonant radiation, as a function of detuning from the resonant frequency. Y-axis is scaled such that zero energy corresponds to the resonant energy of the transition with the mm-waves present. (b) The strengths of the left and right peaks in the AT spectra as a function of detuning from resonant frequency.

Let ν denote the mm-wave frequency on the atoms to obtain an AT spectra and ν_0 denote the resonant mm-wave frequency. The detuning calculated from the strength of the two peaks in the AT spectra is denoted by δ_{calc}. Then,

$$\nu_0 = \nu - \delta_{\text{calc}}. \tag{4.14}$$

The individual peaks in the AT spectra are fit by a gaussian lineshape to determine the spectral areas, $A_{\text{left}}(\propto \sin^2\theta)$ and $A_{\text{right}}(\propto \cos^2\theta)$. The solution for eq. (4.13) yields:

$$\delta_{\text{calc}} = \Omega \frac{A_{\text{left}} - A_{\text{right}}}{A_{\text{left}} + A_{\text{right}}} \tag{4.15}$$

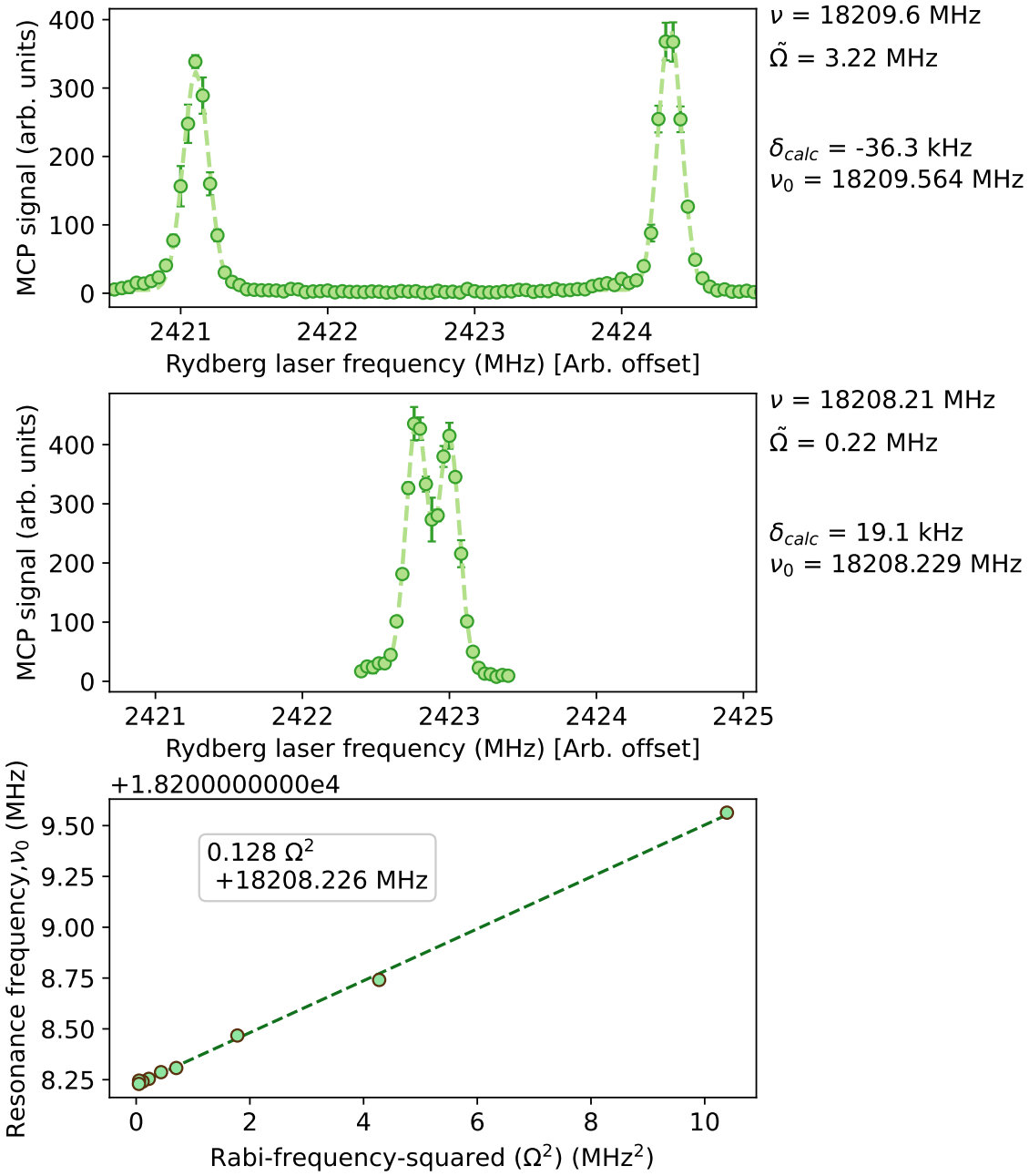

Figure 4.7 : Top two panels show Autler-Townes spectra for two different powers of mm-waves on the atoms for the transition $(5s59s)\,^3S_1 \longrightarrow (5s59p)\,^3P_0$. The bottom panel plots the mm-wave resonance frequency (ν_0) as a function of Rabi frequency.

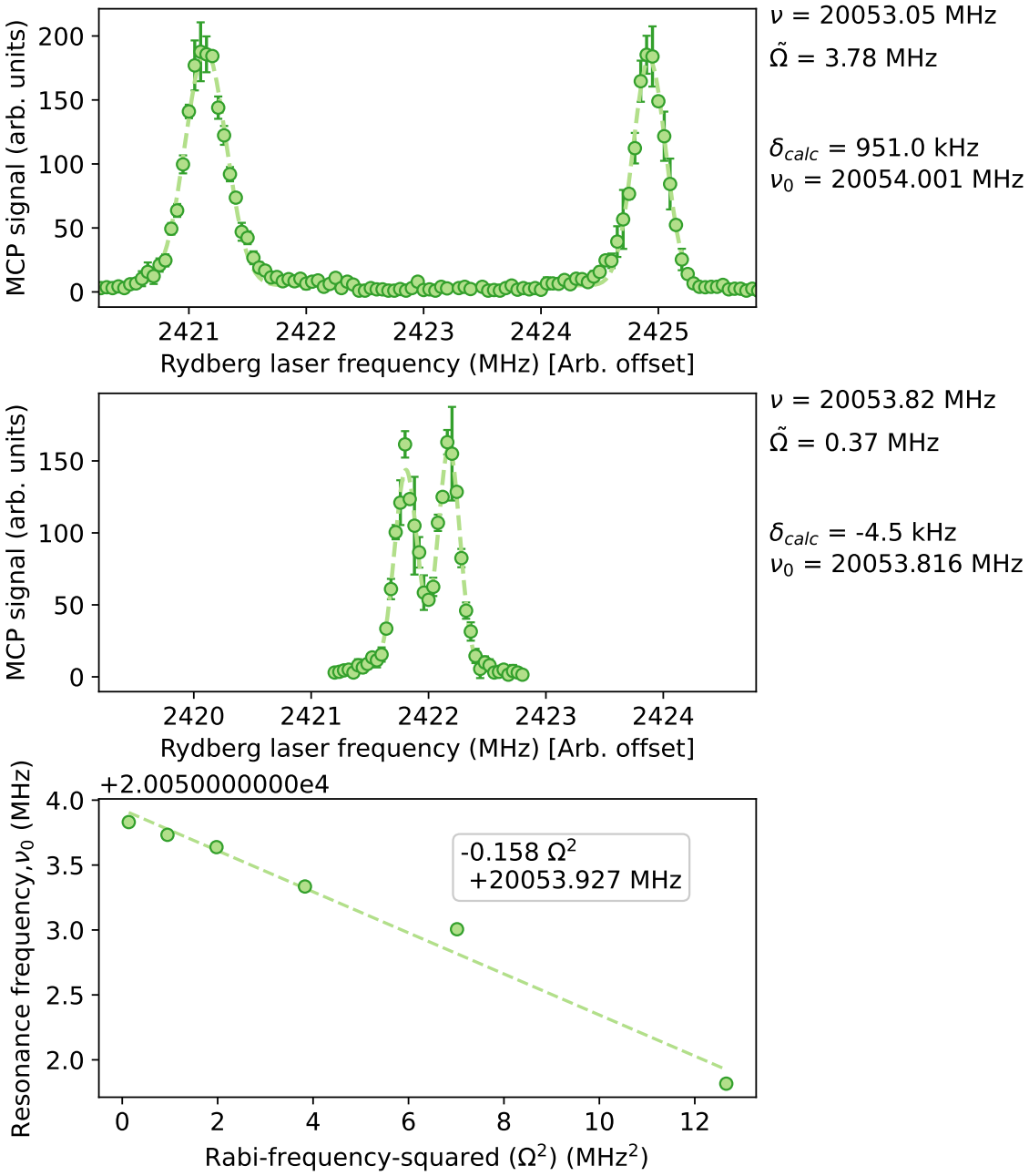

Figure 4.8 : Top two panels show Autler-Townes spectra for two different powers of mm-waves on the atoms for the transition $(5s59s)\,^3S_1 \longrightarrow (5s58p)\,^3P_0$. The bottom panel plots the mm-wave resonance frequency (ν_0) as a function of Rabi frequency.

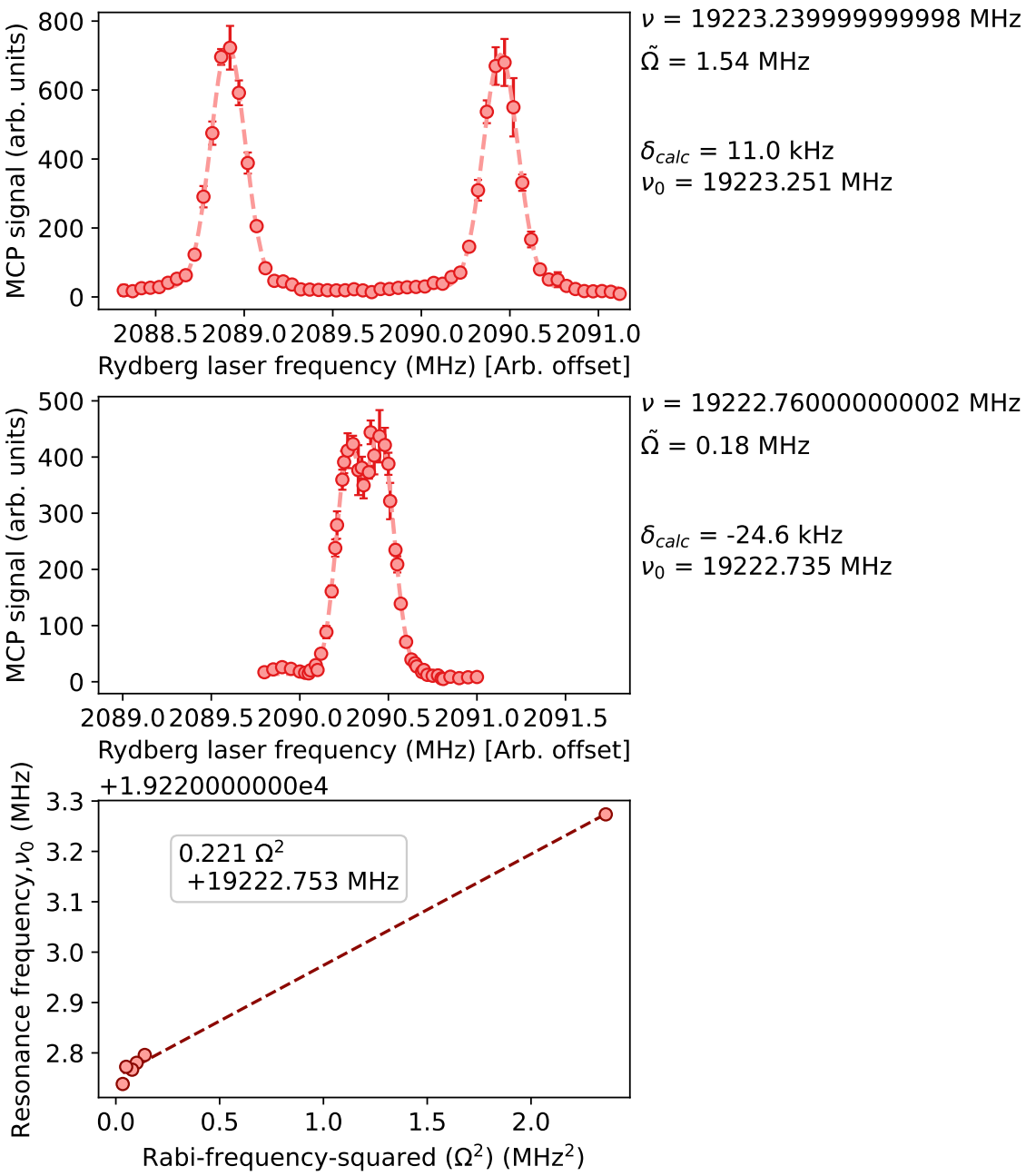

Figure 4.9 : Top two panels show Autler-Townes spectra for two different powers of mm-waves on the atoms for the transition $(5s58s)\,^3S_1 \longrightarrow (5s58p)\,^3P_0$. The bottom panel plots the mm-wave resonance frequency (ν_0)as a function of Rabi frequency.

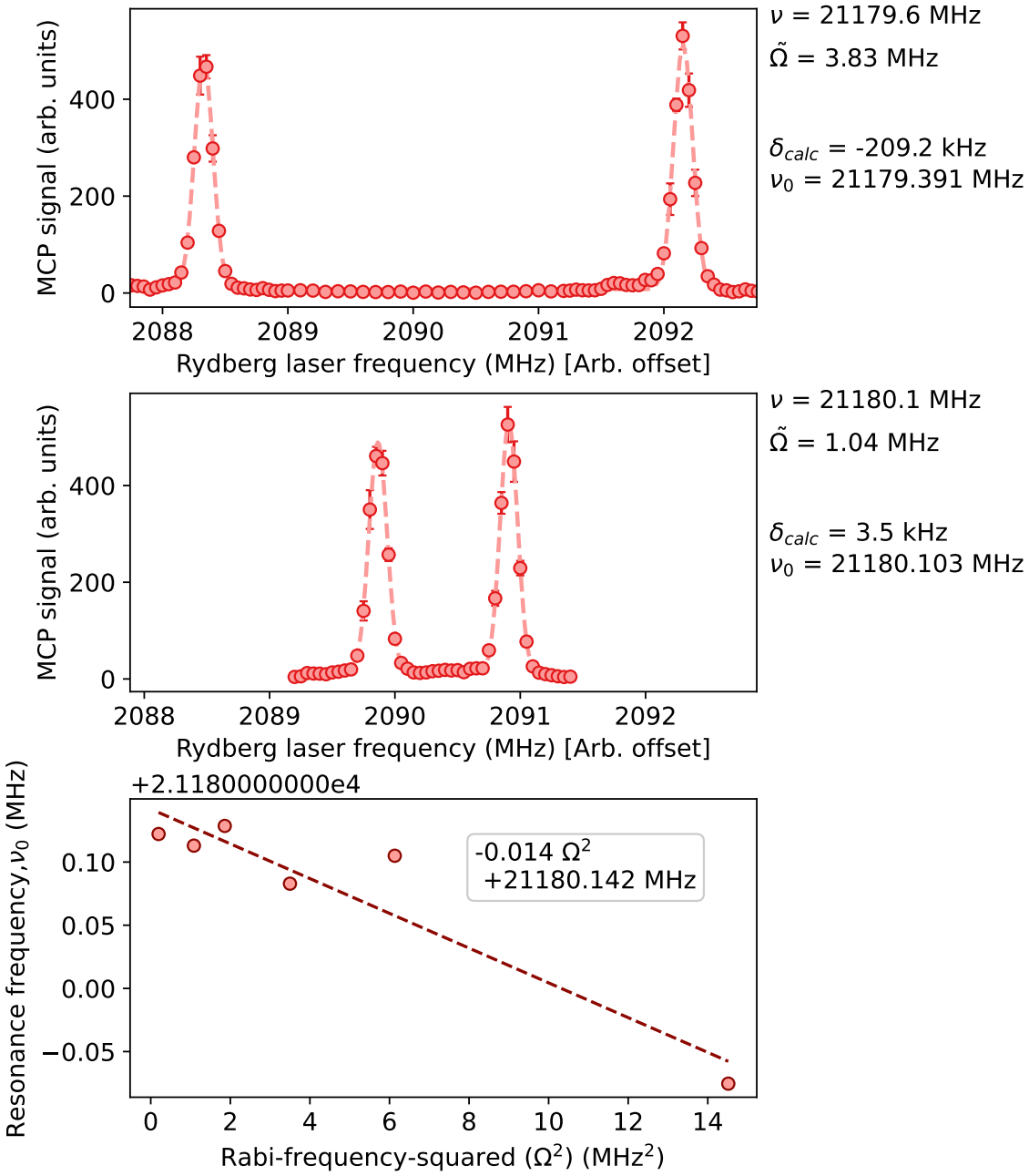

Figure 4.10 : Top two panels show Autler-Townes spectra for two different powers of mm-waves on the atoms for the transition $5s58s\,^3S_1 \longrightarrow 5s57p\,^3P_0$. The bottom panel plots the mm-wave resonance frequency (ν_0) as a function of Rabi frequency.

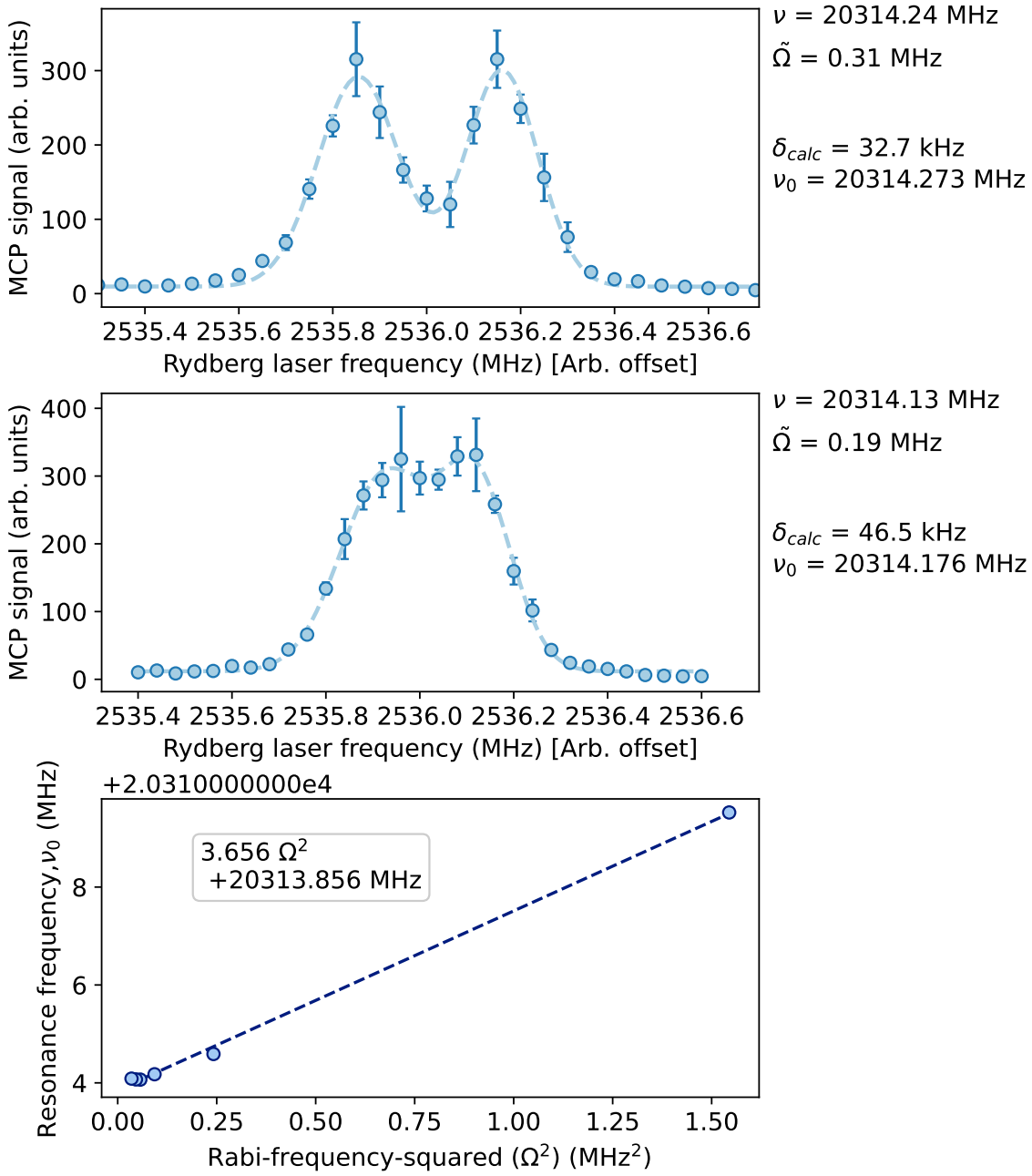

Figure 4.11 : Top two panels show Autler-Townes spectra for two different powers of mm-waves on the atoms for the transition $(5s57s)\,^3S_1 \longrightarrow (5s57p)\,^3P_0$. The bottom panel plots the mm-wave resonance frequency (ν_0) as a function of Rabi frequency.

The AC stark shift resonance frequencies are important to measure because we

need the mm-waves to be on resonance to realize the SSH model (which has zero on-site potential). Moreover, each energy level's resonance frequency is measured in the presence of other frequency components as well, and luckily they are negligible with regards to the experimental linewidth ($\ll 100$ kHz). Even if there are contributions to the overall shift of the energy levels because of other frequency components, they are additive in the low power regime of the experiment.

4.4 Equations that matter

The following sections have been adapted from the publication titled "Realizing topological edge states with Rydberg-atom synthetic dimensions" (Kanungo, S.K., Whalen, J.D., Lu, Y. et al, Nat Commun 13, 972 (2022)).

Let's introduce a few variables first. From now on, the states $(5sns)\,^3S_1\,(m=1)$ are denoted as ns and $(5snp)\,^3P_0$ are denoted as np. The synthetic sites $57s$, $58s$ and $59s$ are mapped to i =1, 3 and 5, while, the synthetic sites $57p$, $58p$ and $59p$ are mapped to i =2, 4 and 6 respectively. The realized Hamiltonian is then given by:

$$\hat{H}_{\text{lattice}} = \sum_{i=1}^{5}(-hJ_{i,i+1}\,|i\rangle\langle i+1| + \text{h.c.}) + \sum_{i=1}^{6} h\delta_i\,|i\rangle\langle i|\,, \tag{4.16}$$

where $J_{i,i+1}$ are the tunneling amplitudes and δ_i are on-site potentials set respectively by amplitudes and detunings of the mm-wave couplings, and h is Planck's constant. To obtain Eq. (4.16), we have neglected counter-rotating terms in the millimeter-wave couplings and transformed into a rotating frame. The kets $|i\rangle$ correspond to the unperturbed Rydberg levels of ^{84}Sr up to a time-dependent phase arising from the transformation. A 4 Gauss field is applied to ensure negligible coupling to $(5sns)\,^3S_1(m=-1,0)$ states by other polarizations of the mm-wave field.

$\delta_i = 0$ yields the SSH model, where the configuration with topologically protected

edge states(TPS) is realized when $J_{i,i+1} = J_w(J_s)$ for i =1,3,5(2,4) and $J_w < J_s$. The trivial configuration is realized when the strength of the couplings are reversed. All data is taken with $J_w = 100$ kHz and $J_s = 0.5 - 3$ MHz.

4.4.1 Probing Rydberg-atom synthetic dimension

Rydberg excitation from the ground-state of ^{84}Sr to the mm-wave coupled Rydberg manifold populates the synthetic space. It is realized by a two-photon excitation using the intermediate $(5s5p)\,^3P_1$ level in a 5 μs pulse. The laser polarizations select excitation to $ns(m = 1)$ levels only. Selective field ionization (SFI) follows immediately, where an electric field liberates any electrons in an excited Rydberg state. The arrival time of these electrons in the charged-particle detector heralds the Rydberg level, or occupied synthetic-lattice site. With the current experimental resolution, arrival times of the states np and $(n + 1)s$ are unresolved.

Figure 4.12 shows the setup to realize the SSH model with strontium Rydberg states, along with the Rydberg excitation scheme to probe the resulting band-structure.

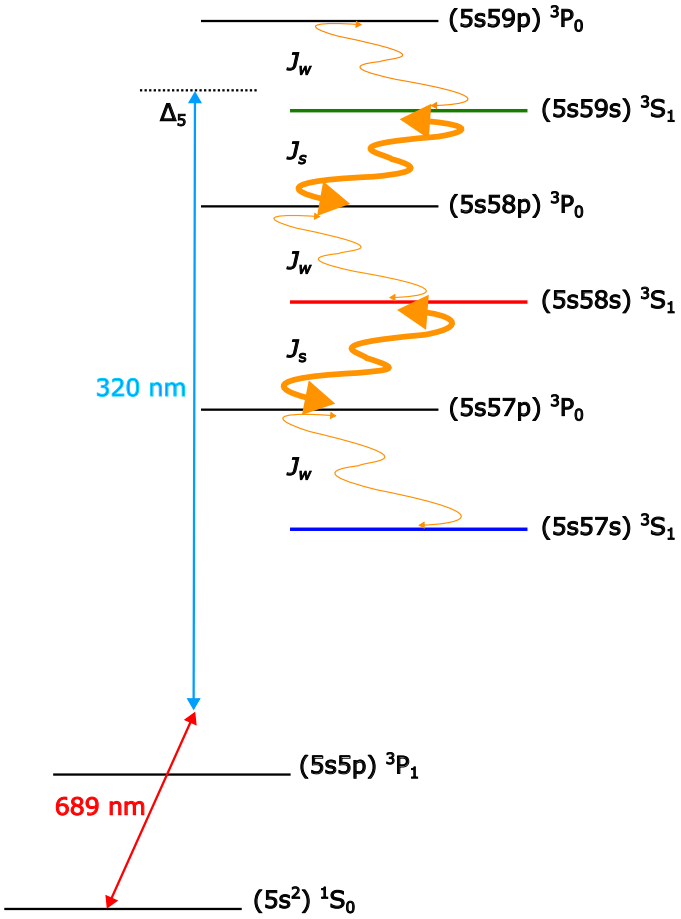

Figure 4.12 : Six-site SSH model in the topological configuration realized on a ^{84}Sr Rydberg atom. The wavy arrows denote near-resonant mm-wave couplings, which induce tunneling between sites of the synthetic lattice. Thicker lines correspond to faster tunneling. The blue and red arrows show two-photon excitation to a Rydberg level of interest (for example, $i = 5$).

The two-photon laser, with detuning $\Delta_{i_{\rm pr}}$ is tuned near the energy of one of the unperturbed Rydberg levels $|i_{\rm pr}\rangle$. Neglecting far off-resonant terms, the Hamiltonian for the entire system is written as:

$$\hat{H} = \frac{h\Omega_{i_{\rm pr}}}{2} |g\rangle\langle i_{\rm pr}| \, e^{i2\pi\Delta_{i_{\rm pr}} t} + \text{h.c.} + \hat{H}_{\rm lattice}, \tag{4.17}$$

where, $\Omega_{i_{\rm pr}}$ (typically ~ 100 Hz $\ll J_w, J_s$) is the effective two-photon Rabi frequency, $|g\rangle$ is the ground-state vector in the frame rotating at the frequency difference of the

$|i_{\rm pr}\rangle$ and $|g\rangle$ levels. The Rydberg excitation rate before convolving with instrumental linewidth is well-described as:

$$\Gamma(\Delta_{i_{\rm pr}}) = \pi^2 \Omega_{i_{\rm pr}}^2 \sum_{\beta} |\langle \beta | i_{\rm pr} \rangle|^2 \delta(\Delta_{i_{\rm pr}} - \epsilon_\beta/h), \tag{4.18}$$

where, $|\beta\rangle$ and ϵ_β are the eigenstates and eigenenergies of $\hat{H}_{\rm lattice}$. Thus, by scanning the two-photon excitation detuning, a spectra is obtained for a topological (or trivial) configuration. Figure 4.13 plots the Rydberg spectra obtained at $i_{\rm pr}$ =1,3 and 5 for $J_s/J_w = 5$.

The strong photon coupling of atomic states can be described in the language of Autler-Townes splitting of multiple levels, where, the coupling Rabi frequency is related to the tunneling rate though $\Omega = 2J$, but, with increasing system size, the lattice interpretation becomes natural. A band structure emerges even for six lattice sites demonstrated here, as do phenomena such as edge states with an energy splitting that is exponentially small in the number of levels.

4.4.2 SSH band structure

The spectrum at different lattice sites $|i_{\rm pr}\rangle$ complement each other to provide a characterization of the band structure and decomposition of the eigenstate, where, the spectral contribution from each eigenstate is proportional to its overlap with the unperturbed Rydberg level corresponding to the lattice site $i_{\rm pr}$.

Figure 4.13(b) shows spectra for the configuration with TPS, $J_s/J_w = 5$, and $\delta_i = 0$ as a function of probe-laser detuning near each of the unperturbed Rydberg ns levels (odd $i_{\rm pr}$). Each spectra is normalized by the total signal for its $i_{\rm pr}$. The signal rate at $\Delta_{i_{\rm pr}} = 0$ corresponds to the the population localized at the upper and lower boundaries of the lattice. For $i_{\rm pr}$=1, the signal at $\Delta_{i_{\rm pr}} = 0$ is the greatest, while it

is observed to decay at the sites $i_{\rm pr}$= 3 and 5. In fact, the zero energy peak is not visible in the $i_{\rm pr} = 5$ spectra. This is the hallmark of the SSH model, where the edge state is present in the gap(of width $\sim 2J_s$) between the non-zero energy bulk states.

The integrated signal intensity around the peak centered at detuning $\Delta_{i_{\rm pr}} = \epsilon_\beta/h$ reflects the overlap of the lattice eigenstate $|\beta\rangle$ with $|i_{\rm pr}\rangle$. Thus, the intensity pattern confirms that the edge states are localized on the weakly coupled boundary site, with little contribution from undressed bulk sites $58s$ ($i_{\rm pr} = 3$) and $59s$ ($i_{\rm pr} = 5$). This is confirmed by the direct diagonalization of eq. (4.16) [shown in fig. 4.13(c)], where it is observed that the overlap of the edge state is minimal with the bulk lattice sites. The widely split bulk states give rise to equal spectral contribution at $\Delta_{i_{\rm pr}} = \pm J_s$, revealing the energy splitting in the band structure. The bulk state features are strong in the spectra at $58s$ and $59s$ undressed levels and is weak near $57s$, which is expected because the eigenstate decompositions show little weight on the edge sites $57s$ and $59p$.

The spectra [in fig. 4.13(e)] for the trivial configuration at $i_{\rm pr}$=1, 3 and 5 with strong tunneling to the boundary, do not possess any zero-energy edge state in the bulk gap. The unresolved bulk peak states are split by $\Delta_{i_{\rm pr}} = \pm J_s$. In this case, every eigenstate is a superposition of all the lattice sites and the direct diagonalization results in fig. 4.13(f) portray this behavior.

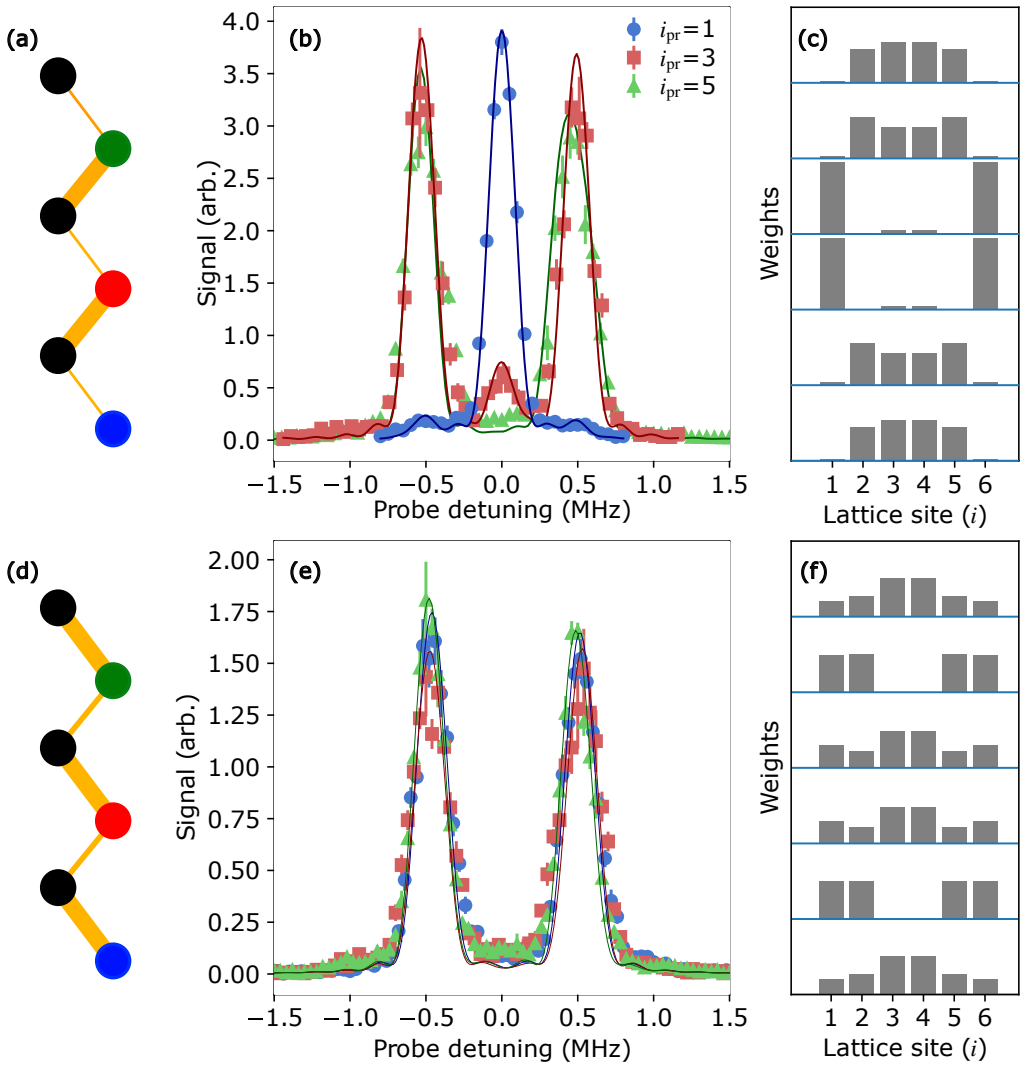

Figure 4.13 : (a) Topological configuration of the SSH molecule color-coded to map to corresponding Rydberg synthetic sites. (b) Rydberg spectra at i =1,3 and 5 for the topological configuration with $J_s/J_w = 5$ in the six-site SSH model in Rydberg synthetic dimensions. The spectra for i =3,5 are multiplied by a factor of 2 for clarity. (c) State-decomposition weights, $|\langle\beta|i\rangle|^2$, for the topological configuration, obtained from direct diagonalization of eq. 4.16 for $J_s/J_w = 5$. (d) Trivial configuration of the SSH molecule. (e) Rydberg spectra at i =1,3 and 5 for the trivial configuration with $J_s/J_w = 5$. (f) State-decomposition weights, $|\langle\beta|i\rangle|^2$, for the trivial configuration with $J_s/J_w = 5$[20].

In figure 4.14, Rydberg spectra in the topological configuration for two different

ratios ($J_s/J_w = 5, 15$) at $i_{\rm pr}$= 1, 3 and 5 are compared. The edge state contribution at $\Delta_{i_{\rm pr}} = 0$ indicate greater localization to $57s\,(i = 1)$ at higher ratios. The direct diagonalization results also confirm vanishing contribution from the bulk to the edge states localized on the boundaries. Also, an increase in the splitting of the bulk states is observed, which matches $\Delta_{i_{\rm pr}} \approx \pm J_s$. From the peak positions in a series of data sets such as in fig. 4.14, the band structure as a function of the strong-tunneling rate J_s can be measured. These agree with results from the direct diagonalization with $\delta_i = 0$.

The series of data sets can also be used to study the variation in state decomposition as a function of strong tunneling rate J_s. Exact diagonalization, such as Fig. 4.14(c) and (d), provides the decomposition of each SSH eigenstate $|\beta\rangle$ upon the bare lattice sites, expressed in the factors $|\,\langle\beta|i\rangle\,|^2$. This is compared with experimental measurements of the fraction of the total spectra area in either the edge or the bulk spectral features when probing the overlap with a specific lattice site in spectra such as Fig. 4.14(a) and (b). Spectral area is determined by fitting each of the three features in a spectrum with a sinc-squared lineshape corresponding to the 5 μs laser exposure time convolved with a 100 kHz FWHM Gaussian linewidth from laser and natural broadening, estimated from independent measurements of spectra in the absence of mm-waves. Center frequency and amplitude are varied for fitting. Figure 4.16 (left) shows that the experimentally measured edge-state fraction matches $\sum_{\beta\in\rm edge} |\,\langle\beta|i_{\rm pr}|\rangle|^2$, and Fig. 4.16 (right) does the same for the bulk contribution and $\sum_{\beta\in\rm bulk} |\,\langle\beta|i_{\rm pr}|\rangle|^2$. The width of the calculated line denotes 10 % variation in the Rabi frequencies. For a given J_s/J_w, the edge-state measurements add to one, while the bulk-state measurements add to 2. This reflects the fact that there are two edge states and four bulk states for this system, and half of the wight for the states in each

group is in overlap with even lattice sites, which the photoexcitation probe does not detect.

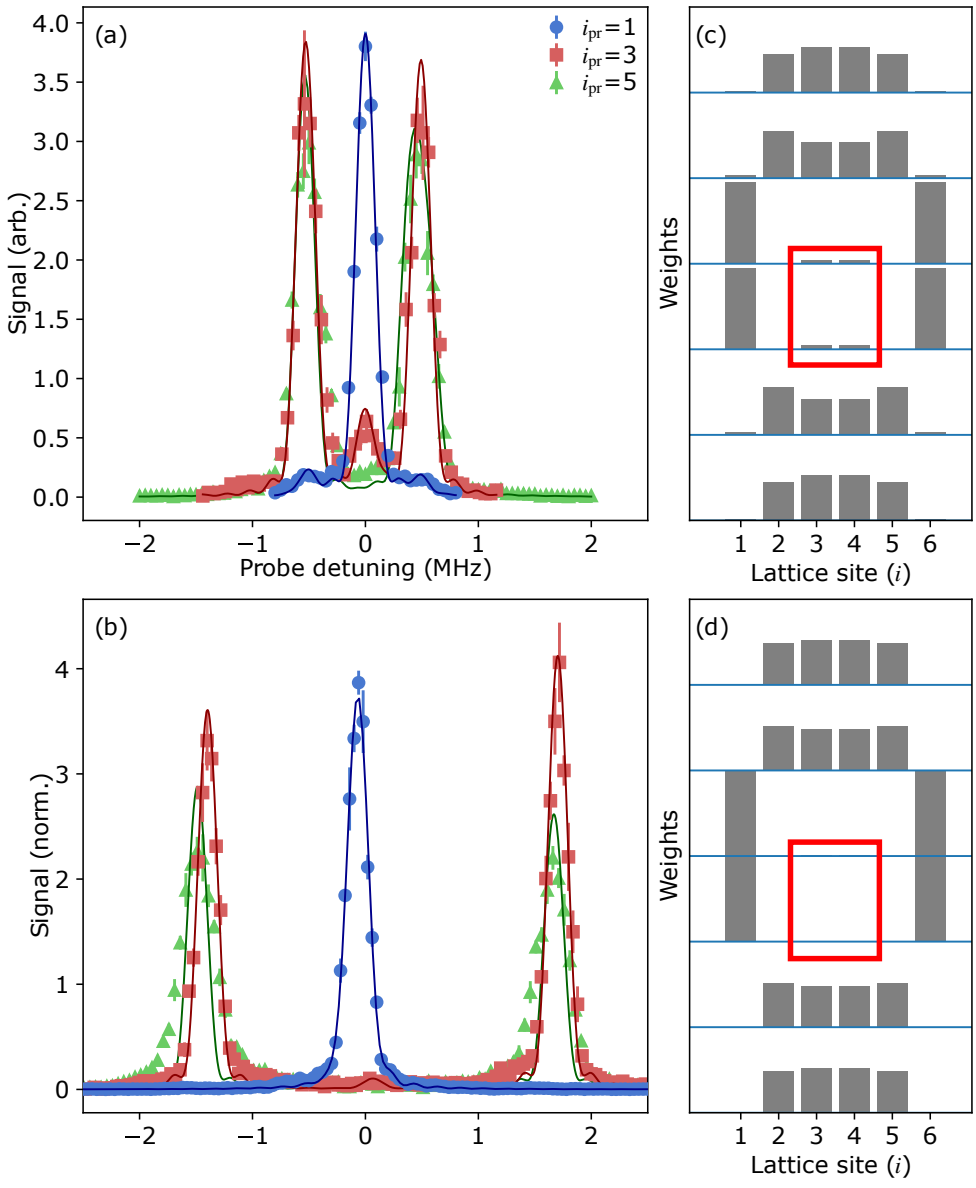

Figure 4.14 : (a) Rydberg spectra at i_{pr}= 1, 3 and 5 for $J_s/J_w = 5$. (b) Rydberg spectra at i_{pr}= 1, 3 and 5 for $J_s/J_w = 15$. (c) Direct diagonalization results for (a). (d) Direct diagonalization results for (b). The edge states have less overlap with the bulk at higher J_s/J_w ratios. This is indicated by the red rectangles[20].

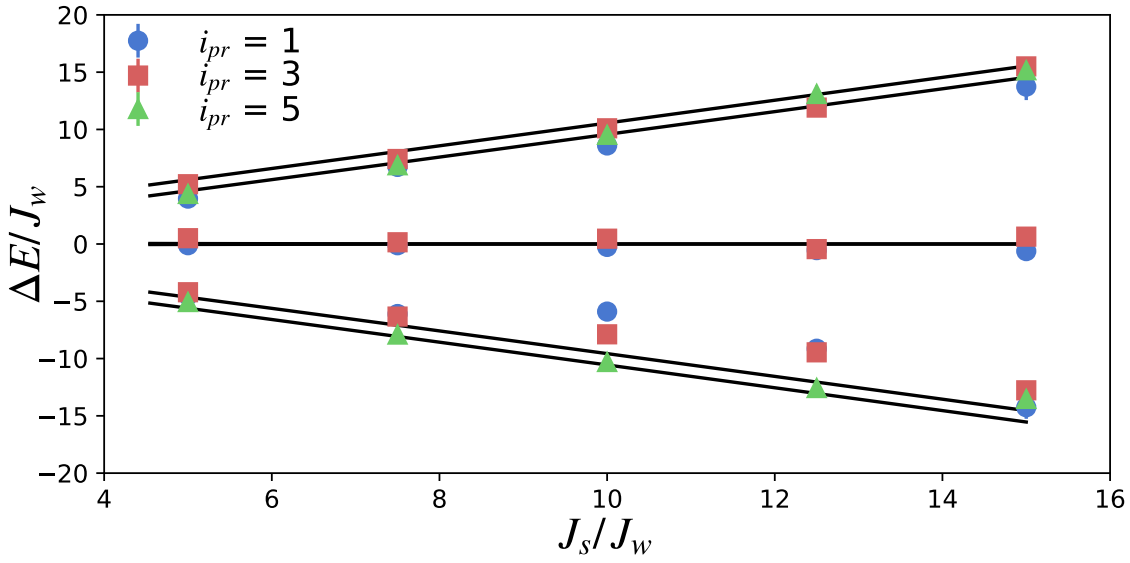

Figure 4.15 : Peak positions (ϵ_β) in the Rydberg spectra, such as in fig. 4.14, giving the bulk and edge state energies for various values of J_s/J_w. Measurements match the band structure calculated by direct diagonalization of eq. (4.16)[20].

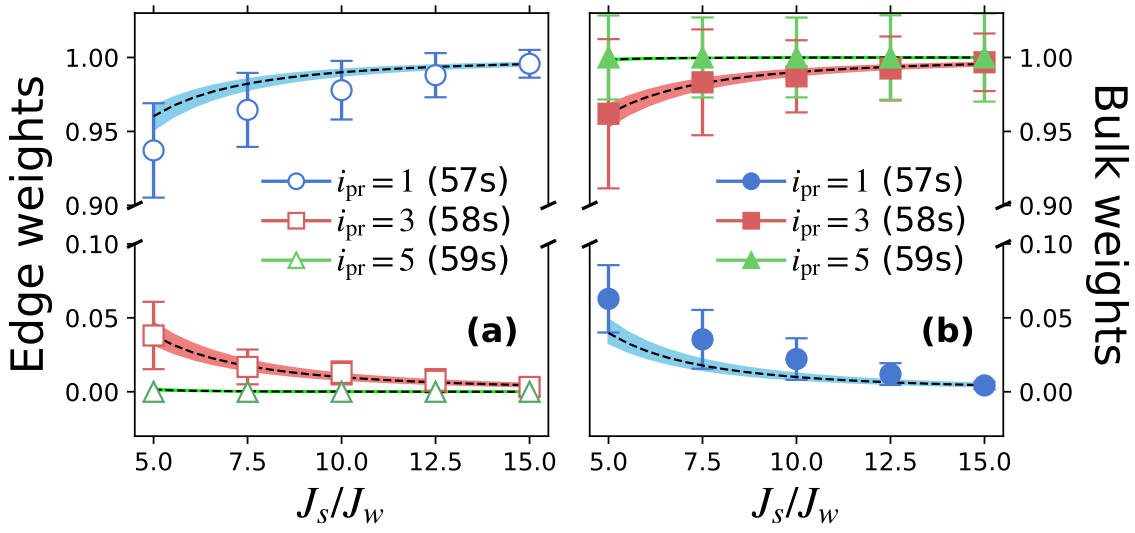

Figure 4.16 : Synthetic-lattice-eigenstate decomposition obtained from spectral-line areas for the configuration with TPS. (a) Fraction of the entire signal under the spectral features corresponding to the edge states for probe tuned near site i_{pr} (Rydberg level) indicated in the legend. The line is the sum of the squares of the calculated overlaps of the SSH edge eigenstates with the i_{pr} site found from direct diagonalization of eq. (4.16) with $\delta_i = 0$. (b) Fraction of the entire signal under the bulk state features and calculated sum of squares of the overlaps of the SSH bulk eigenstates with the i_{pr} site[20].

4.4.3 State decomposition with SFI

The spectral probe is only sensitive to ns contributions to the edge state, and therefore, it cannot establish whether the edge states observed are localized on one boundary site or a superposition of both. To answer that question, we turn to SFI as a tool for site-population measurements in Rydberg-atom synthetic dimensions

Consider Rydberg excitation near $58s$ ($i_{\mathrm{pr}} = 3$) for $J_s/J_w = 5$ and a laser detuning set to the resonance with the left of right bulk-state peaks ($\Delta_{i_{\mathrm{pr}}} \approx \pm 500$ kHz). The electrons which are liberated at ionization fields correspond to Rydberg levels in the bulk of the synthetic lattice, i.e. $i = 2 - 5$. For a laser detuning on the edge-state peak ($\Delta_{i_{\mathrm{pr}}} \approx 0$ kHz), signal arrives at ionization fields corresponding predominantly

to the $57s$ Rydberg state ($i = 1$). This indicates localization of the edge state on the boundary in general and, more specifically, on the single boundary site connected to the ground-state by the two-photon excitation, which is a linear combination of states $\beta = 3$ and $\beta = 4$.

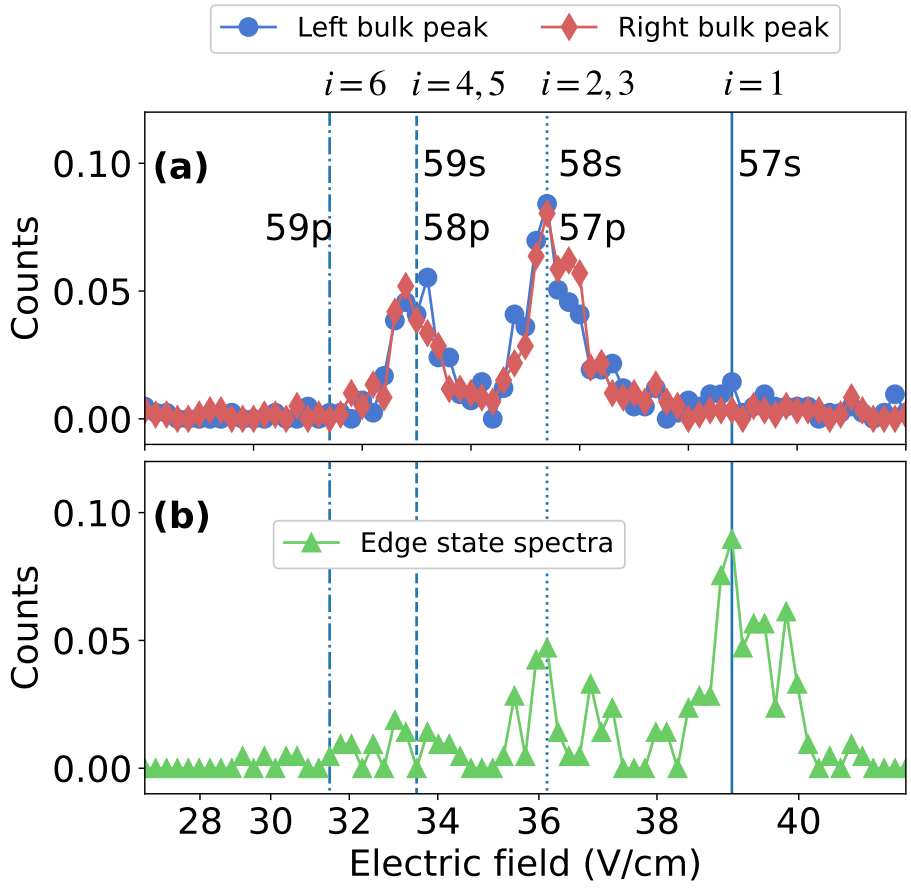

Figure 4.17 : SFI signal for the probe laser tuned near $58s$ for $J_s/J_w = 5$. Vertical lines indicate ionization fields for bare Rydberg levels. The data points are evenly spaced in time. (a) Localization of the bulk-states (at $\Delta_{i_{\rm pr}} \approx \pm 500$ kHz) at the lattices sites $i = 2, 3, 4, 5$. (b) Localization of the edge-state (at$\Delta_{i_{\rm pr}} \approx 0$) at the lattice site $57s$ ($i = 1$). The small contribution to the signal at $i = 2, 3, 4, 5$ is predominantly from the wings of the bulk-state peaks[20].

SFI and trivial configuration

A trivial configuration of the SSH model is realized by switching off the weak $57s-57p$ coupling and switching on a strong $59p-60s$ coupling. Figure 4.18 (right) shows the level structure and the two-photon probe. The states are label from $i = 1-6$ with the lowest energy state labled as $i = 1$. The red, green and blue states ($(5sns)\,^3S_1$) are accessible via our two-photon probe, and the spectra at each $i_{\rm pr}$ is composed of only non-zero energy bulk peaks [as shown in fig. 4.13(e)]. The SFI spectra when the probe is tuned to resonance for each of the bulk features are plotted in fig. 4.18(a, b, and c). The colored brackets in the figure denote the lattice site being probed. It is observed that all the synthetic sites contribute to the signal at each $i_{\rm pr}$. This is in agreement with the direct diagonalization of the eq. (4.16) for the trivial configuration.

Interestingly, there is an asymmetry of the signal in the SFI spectra at each $i_{\rm pr}$. The SFI signal tend to accumulate around the $i_{\rm pr}$ being probed. We intend to explore more in the future, and test the role of the probe in exploring the synthetic dimensions and its effect on the observed decoherence.

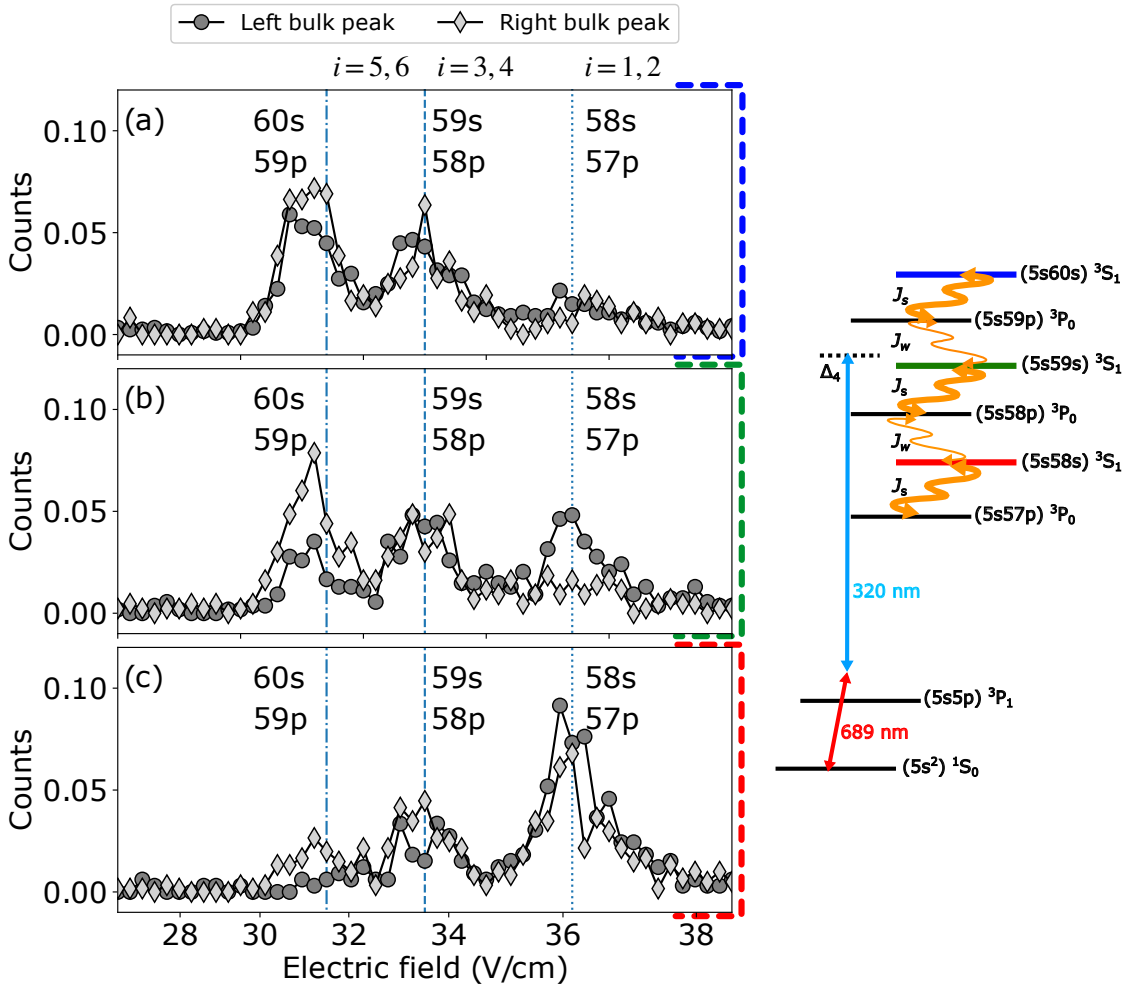

Figure 4.18 : (a) SFI spectra at $i_{\rm pr} = 6$. (b) SFI spectra at $i_{\rm pr} = 4$. (c) SFI spectra at $i_{\rm pr} = 2$. For all the cases, the probe is tuned to resonance on the bulk features in the Rydberg spectra.

4.4.4 Protected edge states

The pinning of the edge-state energy to $\Delta_{i_{\rm pr}} = 0$ is the defining feature of the TPS in the SSH model. It arises due to the inherent chiral symmetry of the system with vanishing matrix elements between sites of different parity, including diagonal(on-site) matrix elements. To demonstrate the robustness of the pinning of the edge-state

energy, the band-structure is probed in the presence of perturbations.

The first kind of perturbation introduced in the system is the imbalance of the strong tunneling rates. Let the strong tunneling rates for the balanced configuration be denoted as $J_{2-3} = J_{4-5} = J_s^0$. A 15% variation is introduced by controlling the mm-wave couplings such that, $J_{2-3} = (1 \pm 0.15)J_s^0$ and $J_{4-5} = (1 \mp 0.15)J_s^0$. The bulk state energies are strongly affected by the imbalance. With an increase J_{2-3}, the bulk states that are more localized on the $i = 3$ site show increased splitting, whereas, with increased J_{4-5}, the bulk states that are more localized on the $i = 5$ site show increased splitting. In contrast, the energy of the edge-state signal is immune to this perturbation. This is because such perturbation preserves the protecting chiral symmetry as the tunneling matrix elements only link even and odd sites.

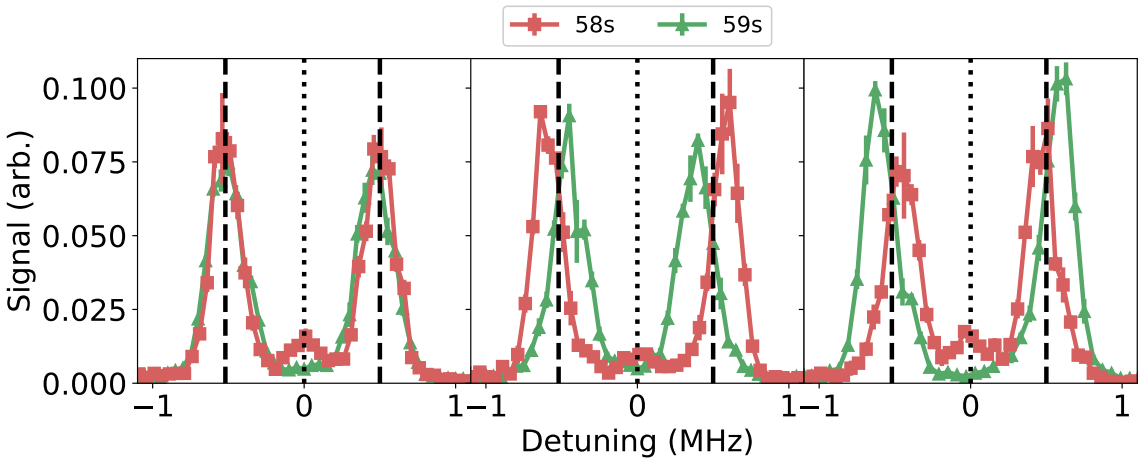

Figure 4.19 : Band structure with Hamiltonian perturbations. (a) SSH model: $\delta_i = 0$ with balanced tunneling rates ($J_{2-3}, J_{4-5} = J_s^0$ and $J_s^0/J_w = 5$). Lines mark positions of the bulk and edge peaks. (b) Strong tunneling rates are imbalanced to $J_{2-3} = 1.15J_s^0$ and $J_{4-5} = 0.85J_s^0$ for $J_s^0/J_w = 5$. This perturbation respects chiral symmetry. (c) Same as (b) but $J_{2-3} = 0.85J_s^0$ and $J_{4-5} = 1.15J_s^0$[20].

The second kind of perturbation introduced to the SSH system does change the edge-state energy by breaking the chiral symmetry. This is realized by shifting the

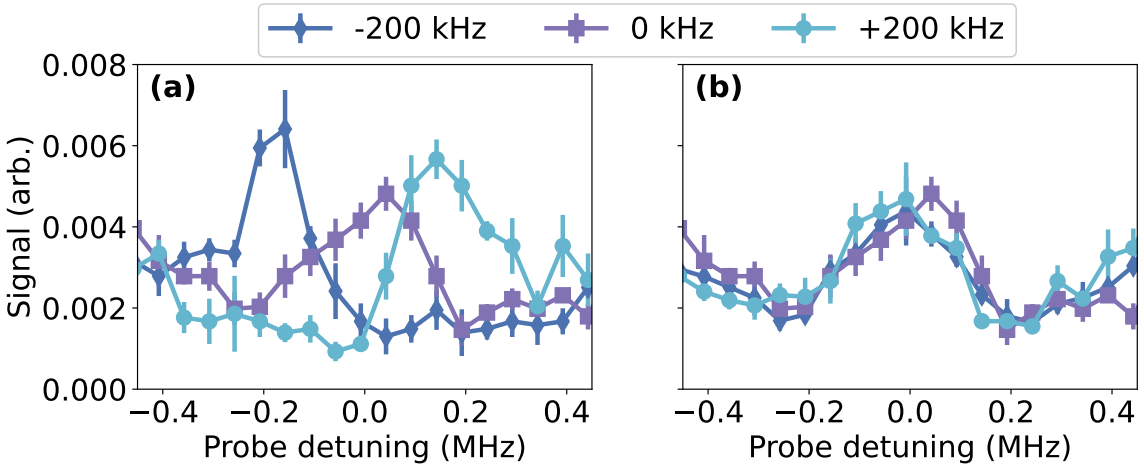

Figure 4.20 : (a) Edge state spectra in the presence of perturbations breaking chiral symmetry: tunneling rates are balanced as in the standard topological SSH configuration, with $J_s/J_w = 10$, but the frequency of the $i = 1$ to $i = 2$ $(57s - 57p)$ coupling is varied by the value given in the legend. Spectra are recorded with the probe laser tuned near the 58 level ($i_{\rm pr} = 3$). (b) Same as (a), but the $i = 5$ to $i = 6$ $(59s - 59p)$ coupling frequency is varied. All error bars denote one s.e. of the mean[20].

on-site potentials by changing mm-wave frequencies. Spectra are recorded with the probe laser tuned near the $58s$ level ($i = 3$) for the $J_s/J_w = 10$. In figure 4.20(a), the frequency of $i = 1$ to $i = 2$ is varied, which shifts the value of δ_1 and hence the on-site potential at $i = 1$ site. $\delta \neq 0$ introduces a diagonal term in the Hamiltonian that breaks the chiral symmetry, and the edge-state energy shifts by an amount equal to the detuning from resonance. For fig. 4.20(b) the frequency connecting the site $i = 5$ to $i = 6$ is varied, which changes the value of δ_6, and the position of the edge-state signal remains unchanged. These results confirm that the edge state coupled to by the probe laser is localized on the $i = 1$ boundary site. The orthogonal edge state is localized on $i = 65$, with vanishing weights on odd sites. In general, we expect any kind of perturbation connecting even to even or odd to odd sites will break the chiral symmetry and shift the edge states.

4.5 Discussion on decoherence

The lineshape of the spectra deviates from the sinc-squared lineshape convolved with an experimental linewidth of 100 kHz. In order to gain insight into this phenomena and comment about the broader implications on expanding the size of the synthetic dimensions and limits on the physics that can be explored, a numerical approach was adopted by our theory collaborators (S.D. Dasgupta, M. Yuan and Dr. K.R.A. Hazzard) to understand sources of decoherence linked to amplitude or frequency noise of the mm-waves.

Equation 4.16 provides an idealized description of the SSH lattice that neglects certain effects, which warrant discussion. One, the current treatment neglects coupling to off-resonant magnetic sublevels ($m = -1, 0$) of the ns states. Theoretical simulation predicts shifting of Rydberg levels in addition to AC stark shifts and no effect on broadening of spectral lines. The shifts are compensated by experimentally measuriung them and setting the detuning of the mm-waves to be on-resonant to the levels shifted by AC stark shift and off-resonant coupling to magnetic sublevels.

Two, counter-rotating terms were dropped to arrive at eq. (4.16). The tunneling rates are $\sim$1.5 MHz and Rydberg energies are $\sim$ 20 GHz, which means the effect of keeping counter-rotating terms are of the order 10^{-4} or smaller. Numerical simulations confirm such effects are negligible.

A third possible source of deviations is the presence of dissipation or decoherence in the system that could arise from multiple sources such as, spontaneous decay from a Rydberg state or stimulated decay due to black-body radiation. These effects predict a lifetime of around 60 μs, which is long compared to the timescale of this experiment. Spectroscopy of two isolated Rydberg levels reveal a linewidth of around 50 kHz, which is much less than the linewidths observed in the current experiment.

It implies magnetic field noise and stray electric fields are not the major contributors to decoherence.

It is observed that the decoherence rates measured by the decay of Rabi oscillations between two Rydberg levels in the experiment is dependent on the intensity of the mm-waves on the atoms (Fig. 3.8). To capture this effect numerically, decoherence rates ($\Gamma_i^{i_{\rm pr}}$) are assumed to be proportional to the mm-wave amplitude ($\Gamma_i^{i_{\rm pr}} = \mathcal{C}^{i_{\rm pr}} J_{i,i+1}$) and the Lindbladian master equation (shown below) is solved.

$$\dot{\rho} = -\frac{i}{\hbar}[\hat{H}, \rho] + \sum_{i=1}^{N} \Gamma_i \left[L_i \rho L_i^\dagger - \frac{1}{2}\left(L_i^\dagger L_i \rho + \rho L_i^\dagger L_i \right) \right] \tag{4.19}$$

where ρ is the density matrix, $\hat{H}$ is the Hamiltonian in Eq. (4.17), and the jump operators L_i depend on the noise model. For mm-wave amplitude noise

$$L_i^{\rm amp} = \begin{cases} |i\rangle\langle i+1| + |i+1\rangle\langle i| & \text{if } i < N \\ 0 & \text{if } i = N \end{cases}. \tag{4.20}$$

Discrepancies between observations and decoherence-free theory are visible in the linewidths for $i_{\rm pr} = 5$ for the largest value of strong coupling J_s (Fig. 4.21). Other differences between theory and experiment are the small reductions in contrast between the spectral features and a very small increase in weight and smoothing in the tails of the spectra, which are seen most strongly for $i_{\rm pr} = 5$ (Fig. 4.22). Calculations with decoherence capture these effects and provide values for decoherence rates $\Gamma_i^{i_{\rm pr}}$ by fitting to the spectra for each value of $i_{\rm pr}$.

Trends in the decoherence emerge from this analysis. One already mentioned is that the decoherence for $i_{\rm pr} = 5$ is much larger than for other $i_{\rm pr}$ values when in the topological tunneling configuration, which is reflected in a value of $\mathcal{C}^{i_{\rm pr}=5}$ that is ~ 3 times larger than for other $i_{\rm pr}$. When in the trivial configuration, no such difference is observed. A possible explanation is that the fluctuations on the coupling between

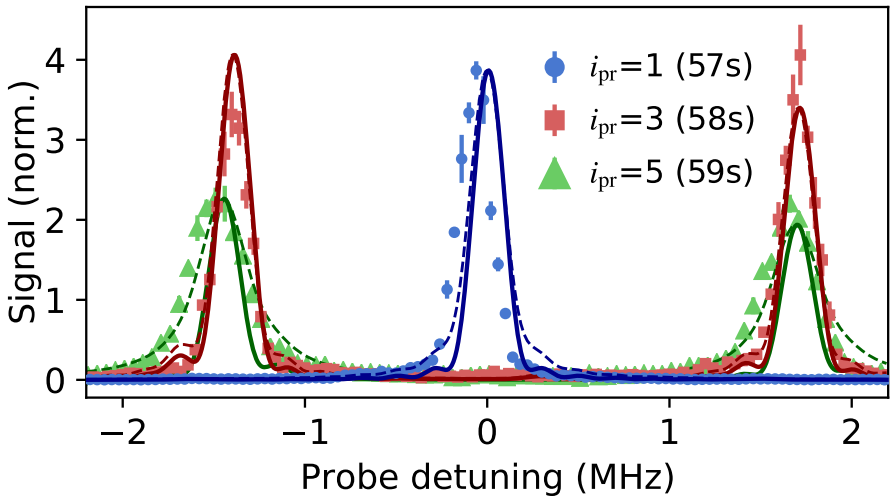

Figure 4.21 : **Noise model analysis.** Fits of experimental data with theoretical calculations assuming no decoherence (———), and using the amplitude-noise model [Eq. (4.20), - - - - -]. Data shown are for $J_s/J_w = 15$ [from fig. 4.14(b), the $i_{\mathrm{pr}} = 3, 5$ spectra have been multiplied by a factor of 2 for clarity]. All error bars denote one s.e. of the mean.

$|5\rangle$ and $|4\rangle$ are particularly noisy. Another possibility is coupling of one or multiple bare states to higher angular momentum states by the millimeter-wave fields, perhaps through multi-photon transitions. Experiments described here were performed with triplet Rydberg states. Working with the less-dense manifold of singlet states would reduce the chance of spurious couplings.

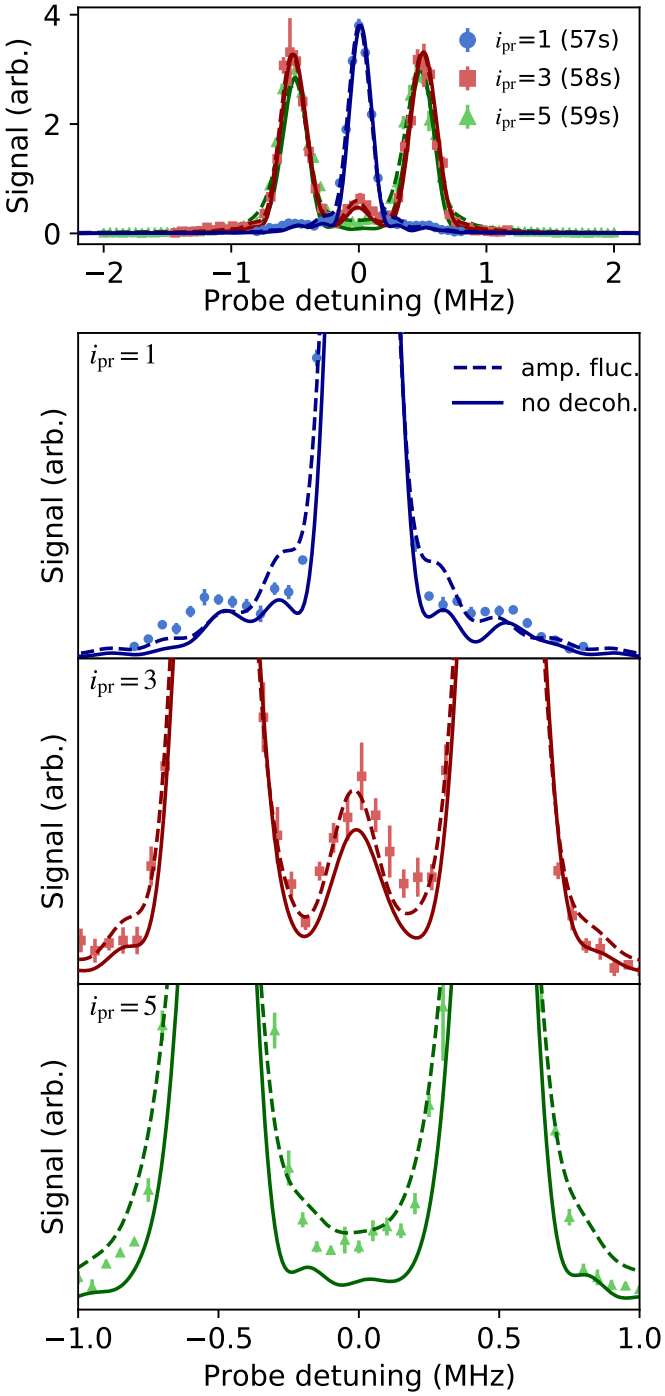

Figure 4.22 : **Noise model analysis.** Same as fig. 4.21, but experimental data shown are for $J_s/J_w = 5$ [from fig. 4.14(a)]. Top panel shows all three i_{pr} while the bottom three panels show central regions of the same data for the individual i_{pr} indicated in each panel. All error bars denote one s.e. of the mean.

Chapter 5

Conclusion and future directions

5.1 Conclusion

We have demonstrated Rydberg-atom synthetic dimensions as a promising platform for the study of quantum matter. The spectrum of photo-excitation to the synthetic lattice space formed by the manifold of coupled Rydberg levels provides the band structure and decomposition of the lattice eigenstates. SFI of the excited states provides an additional diagnostic of lattice-site populations with two-site resolution. TPS were observed in a six- site SSH model, and the measured band structure and eigenstate decomposition agree well with theory. Varying the detuning of the millimeter-wave fields that create tunneling between sites introduces on-site potentials, and this has been used to break the chiral symmetry of the SSH model and to shift the energies of edge states away from the center of the bandgap at $\Delta_{i_{\rm pr}} = 0$. Numerical simulations based on the master equation were pre- sented, which enable investigation of decoherence effects.

Demonstration of the defining features of the SSH model illustrates the potential of Rydberg-atom synthetic dimensions for quantum simulation. The size of the synthetic space can be expanded by applying more millimeter-wave frequency components, although this will introduce additional complexity such as the need to use multiple local oscillators and horns to cover a wider range of frequencies. The limits imposed by Rydberg-level decoherence, AC stark shifts, and coupling to ancillary levels need

further study, but our initial investigations, as well as previous work demonstrating coherent manipulation of Rydberg-level populations[82, 83], indicate that these should be technical, rather than fundamental, complications.

The most exciting prospect is to extend these capabilities to the study of interacting, many-body systems [45, 84] using arrays of single Rydberg atoms in closely spaced optical tweezers [85, 86] with appreciable long-range dipolar interactions in real space [24] but negligible tunneling of atoms between microtraps. For the Rydberg-level arrangement demonstrated here, the dominant interactions would be flip-flop interactions that couple $|ns, n'p\rangle$ and $|n'p, ns\rangle$ states, giving the many-body Hamiltonian

$$H = -\sum_{i,a} t_i \left(c_{ia}^\dagger c_{i,a+1} + \text{h.c.} \right) + \sum_{ij,ab} V_{ij;ab} c_{ib}^\dagger c_{ja}^\dagger c_{ia} c_{jb} \tag{5.1}$$

where the c_{ia} and $c_{ia}^\dagger$ are annihilation and creation operators (which can be taken to be either fermionic or bosonic since there is no real-space tunneling) at synthetic site i and real space site a, and the interaction matrix elements $V_{ij;ab}$ take the form $V_{ij,ab} = \frac{1-3\cos^2\theta_{ab}}{r_{ab}^3} M_{i,j} \delta_{\text{mod}(i-j,2),1}$ where $r_{ab} = |\vec{r}_a - \vec{r}_b|$ is the (real-space) distance between atoms a and b, and θ_{ab} is the angle of $\vec{r}_a - \vec{r}_b$ relative to the quantization axis. Here the quantization axis is the one defining the m levels. The matrix element $M_{i,j}$ falls off rapidly with $|n - n'|$ [87] and thus $|i - j|$, so, in contrast to many other types of synthetic dimensions, the interactions are highly local in the synthetic space. This can give rise to interesting quantum phases and phase transitions, such as quantum strings and membranes [45, 84]. We expect this to be just a small sample of the phenomena these systems can display, with a wide variety of scenarios arising from the easily tunable and dynamic synthetic and real-space geometries.

5.2 Future direction

5.2.1 Other interesting realizable systems

There could be many interesting lattice structures envisioned with the array of states available in the Rydberg-atom synthetic dimensions. An example is the realization of a breathing kagome lattice. It is a tripartite lattice, whose unit cell contains three lattice sites, with alternating intra- and inter-cell hopping amplitudes. A key feature of the system is the presence of a phase that possesses corner modes at zero-energy. It is defined as the non-trivial phase of the breathing kagome lattice, very similar to the zero-energy edge state in the SSH model. There are interesting aspects to explore in terms of topology, and whether such states are topologically protected against different types of perturbations which may or may not respect the inherent chiral symmetry.

The unit cell contains three sites, shown as yellow, blue and grey in the inset of figure 5.1. The intra- and inter-cell hopping are denoted by $\Omega^{'}/2$ and $\Omega/2$ respectively. In the tight-binding model, the Hamiltonian in the reciprocal space is given by[88]:

$$\hat{H} = \begin{pmatrix} 0 & \Omega/2 + \Omega^{'}/2e^{i\mathbf{k}a_3} & \Omega/2 + \Omega^{'}/2e^{i\mathbf{k}a_2} \\ \Omega/2 + \Omega^{'}/2e^{-i\mathbf{k}a_3} & 0 & \Omega/2 + \Omega^{'}/2e^{i\mathbf{k}a_1} \\ \Omega/2 + \Omega^{'}/2e^{-i\mathbf{k}a_2} & \Omega/2 + \Omega^{'}/2e^{-i\mathbf{k}a_1} & 0 \end{pmatrix} \tag{5.2}$$

where, $\mathbf{k}$ is the crystal momentum, and $a_{1,2} = (\pm 1/2, \sqrt{3}/2)$ and $a_3 = a_2 - a_1 = (-1, 0)$ are the lattice vectors. Such couplings can be realized experimentally with mm-waves. All the parameters have full tunability, including introduction of on-site potentials.

A scheme to realize the breathing kagome lattice is presented by using strontium Rydberg states in figure 5.1, where the color of the tunneling encode the different kinds of mm-wave couplings. But to realize such complex quantum matter in Rydberg-atom

synthetic dimensions, one has to move beyond single-photon $S - P$ couplings (like shown for the six-site SSH model in this thesis) and incorporate other states, such as, $^1D_2$ states, which require resonant two-photons couplings.

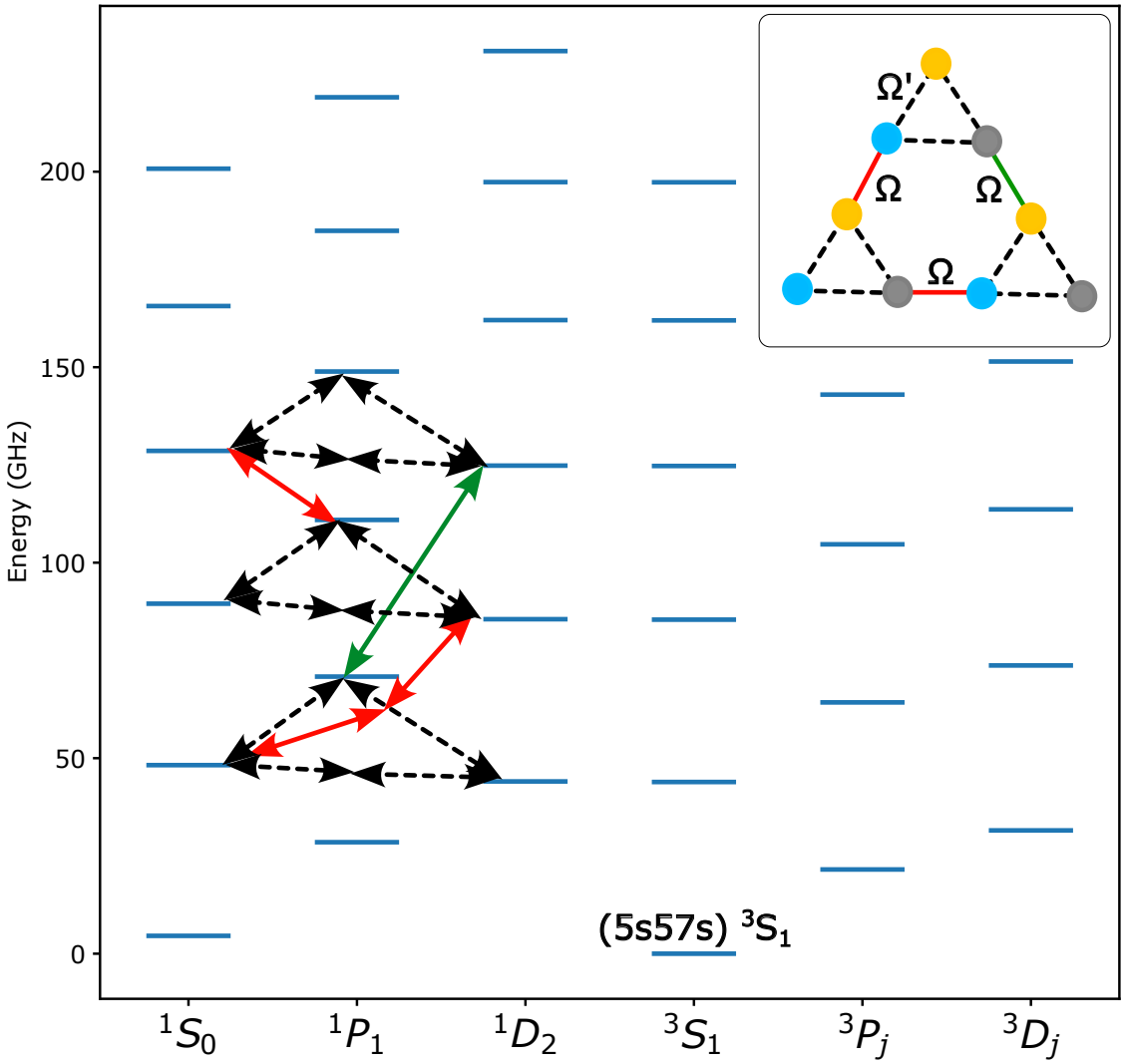

Figure 5.1 : A Rydberg synthetic dimension scheme to realize a breathing kagome lattice that harbors corner states.

Another example could be the realization of loop topologies. Figure 5.2 shows 15 Rydberg states connected by mm-wave couplings. For such a large system a two-

photon coupling with $\Delta n = 4$ is necessary to close the loop. It is interesting to note that by changing the $S - S$ and $D - D$ couplings to $S - D$ and $D - S$ couplings a Mobius strip topology can be realized.

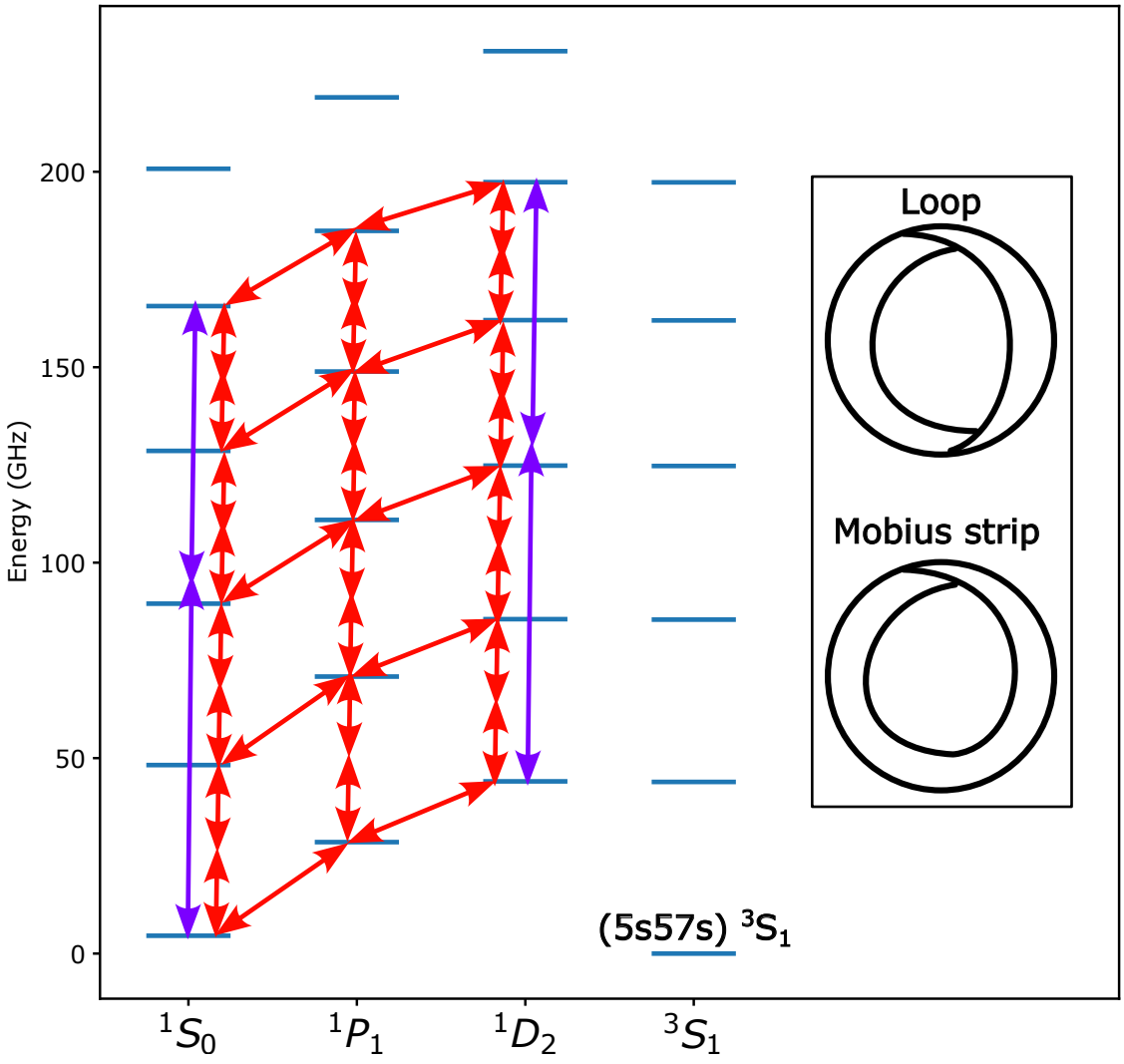

Figure 5.2 : Rydberg synthetic dimension scheme to realize a loop topology using K-, Ka- and W-band mm-wave frequencies. Swapping the $S - S$ and $D - D$ to $S - D$ and $D - S$ couplings realizes a Mobius strip topology (as shown in inset). The red photons lie in the K-band and the violet photons lie in the W-band.

These are visually complex structures, but the current experiment with six-site SSH model offers techniques that will make such a structures feasible. Some of the challenges that may arise include the wide range of mm-wave frequencies required to realize all the couplings. Multiple horns fed by mm-wave synthesizers, whose phases can be controlled by a single local oscillator, will be required, and this is certainly possible in the realms of the current experiment. For example, the mm-wave frequency for the green coupling, shown in fig. 5.1, lies in the Ka-band ($\sim 27-40$ GHz), whereas mm-wave frequencies for other couplings (red and black) lie in the K-band ($\sim 16-27$ GHz). The frequency for the violet two-photon coupling in figure 5.2 lies in the W-band ($\sim 75-110$ GHz).

It will be particularly interesting to conduct pump-probe type experiments, especially with the powerful tool of SFI. Such experiments will require exciting to a bare Rydberg state without the presence of any mm-wave coupling and then turning on the mm-wave components diabatically to project the initial state on the new set of eigenstates for the geometry realized, such as the SSH or the breathing kagome lattice. A time of evolution measurement, where the system is allowed to evolve for a time, T, with the synthetic lattice on and then diabatically switching off the lattice to project the state back to the bare Rydberg manifold, followed by SFI detection to measure population in different state will be interesing.

Appendix A

UV fiber profiles

As discussed in Ch. 2 of this thesis, the pointing problem of the UV beam was solved by using a fiber intermediary (LMA-10-UV-PM, UV fiber from Alphanov) between the source of 320 nm photons (Toptica SHG cavity) and the position of the atoms in the science chamber. Adjustable fiber collimators (60FC-4-S24-49-XV) are used on the input and output side of the fiber to help couple light into the fiber. The collimator housing contains a 12 mm plano-convex lens with focal length 24 mm and NA = 0.10. The position of this collimator can be adjusted with an eccentric key (60EX-5) to optimally position the lens with respect to the tip of the fiber. Figures A.3 and A.6 are the beam profiles on the input and output sides of the UV fiber. The profile is obtained by capturing the image of the beam at various positions along the beam path on a camera (Duma Optronics, BA7-UV-USB). The image is fit to two gaussians along the minor (vertical) and major (horizontal) axis respectively of the ellipsoid shaped beam cross-section and the fit beam waists are plotted versus distance of the camera from the front face of collimator.

In order to couple UV beam from the SHG through the input collimator, a profile of the free-space beam after the 150 MHz AOM was measured. A lens combination was chosen based on this profile so that UV light can be coupled via efficient mode-mathcing with the input collimator. The lenses (+500 mm and -400 mm cylindrical lenses with a vertical axis), separated by 5 cm, are shown in figure A.1 after the UV AOM. This results in a 30 % coupling quite easily with minimal beam walking

and tweaking of the collimator position with the eccentric key. A maximum of 40 % efficiency of coupling has been observed with this fiber. A major factor which affects the coupling performance is the cleanliness of the UV fiber tip. Dust settles on the tip overtime and hence needs to be cleaned every few months with Isopropanol (99%). To avoid settling of particles on the tip, it must be purged with nitrogen gas with a flow rate of 1.35 SCFH at all times . A photo of the mount with the flush hole and tube is shown in fig. A.2.

The output of the UV fiber is connected to a cage system (shown in fig. A.1) which contains a half-wave plate, a polarizing beam splitter, a beam-sampler and a pair of lenses in a telescope configuration. The half-wave plate can be adjusted to maximise the p-polarized power transmitted to the atoms. The beam-sampler reflects less than 1% of the total power onto a UV photodiode (SM05PD7A - Thorlabs) to monitor the power. The telescope is composed of a convex lens (200 mm focal length), followed by a concave lens (-100 mm focal length) to reduce the spot size from 500 microns, at the output face of collimator, to a collimated beam with a spot size of $\sim$250 microns. This increases the intensity of UV light at the atoms by a factor of 4 to get a better signal to noise ratio for a number of weak transitions, such as Rydberg trimers, tetramers etc.

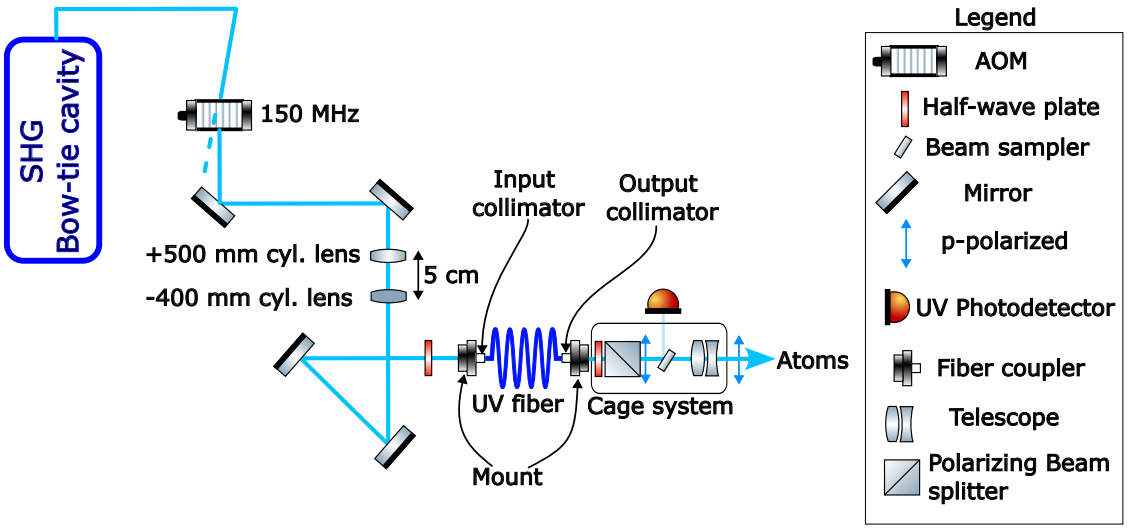

Figure A.1 : Layout of optical components to have a collimated UV beam on the atoms. The profile of the free-space beam from the second mirror after the 150 MHz AOM was measured. The cylindrical lens combination immediately following the mirror results in a collimated beam with a waist of about 500 microns that couples efficiently with the UV fiber on the input side. The output profile (A.6) was measured before the cage system to help calculate the focal length of the lenses needed for the telescope. The telescope reduces the spot size to about 250 microns.

Figure A.2 : Collimator is secured inside a modified AD12F (Thorlabs) mount. The tube in the photo purges the tip of the fiber with nitrogen at a flow rate of about 1.35 SCHF. The eccentric key (that has a white marker and is below the tube) rotation adjusts the position of the lens inside the collimator.

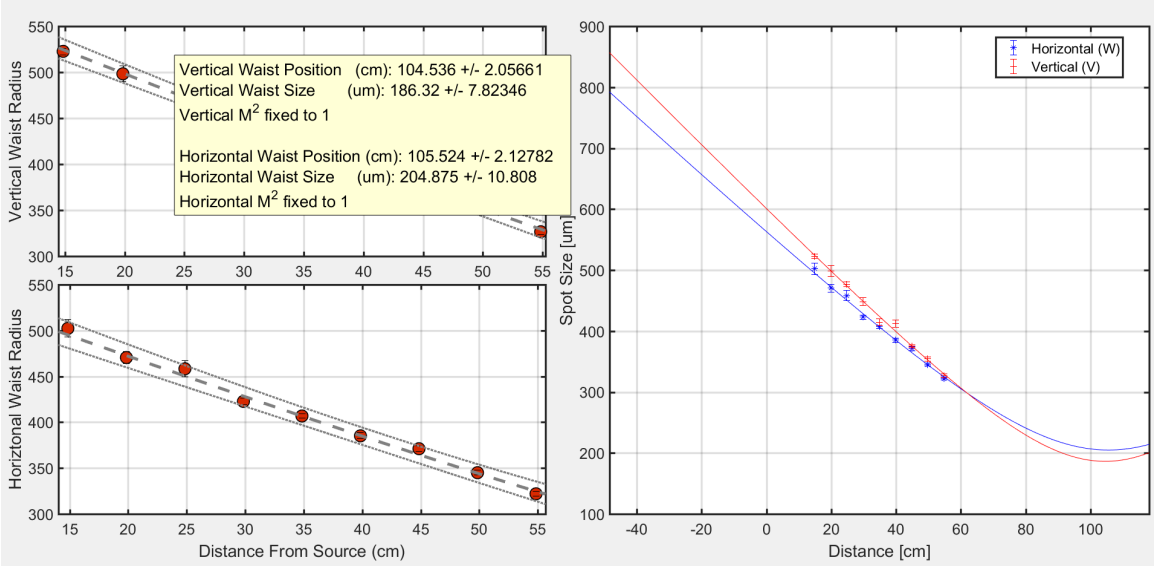

Figure A.3 : Beam profile of light from the input collimator. 0 cm represents the location of the front face of the collimator. The lens position inside the collimator is adjusted to get the best possible collimation.

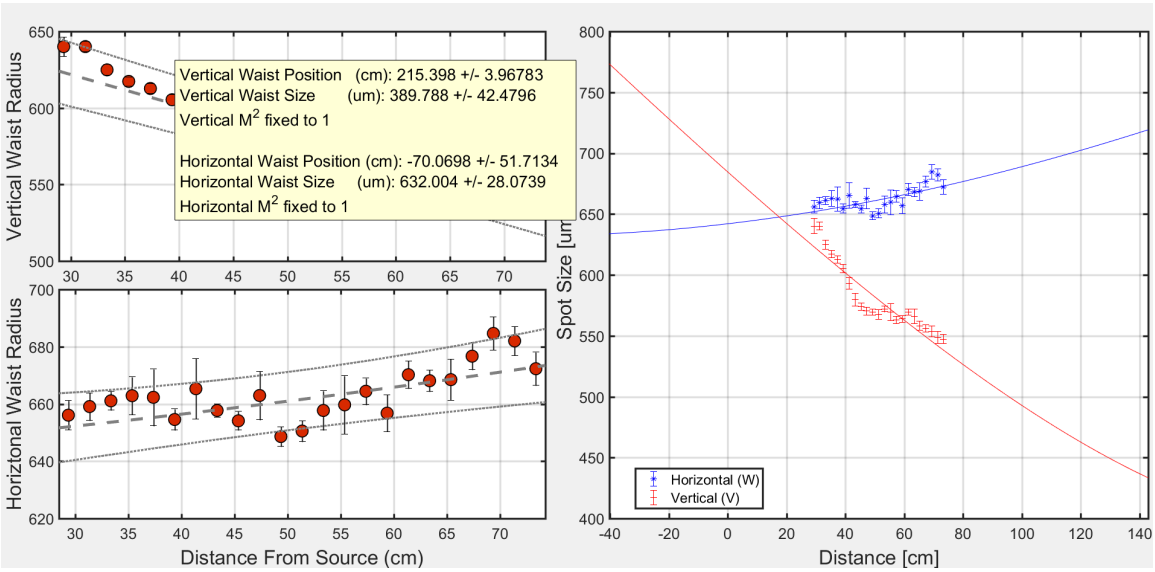

Figure A.4 : Beam profile measured from the second mirror (see fig. A.1) after the UV AOM. The vertical component of the beam needs to be collimated to around 500 microns spot size to mode-match the input collimator profile (A.3) of the UV fiber and get efficient coupling.

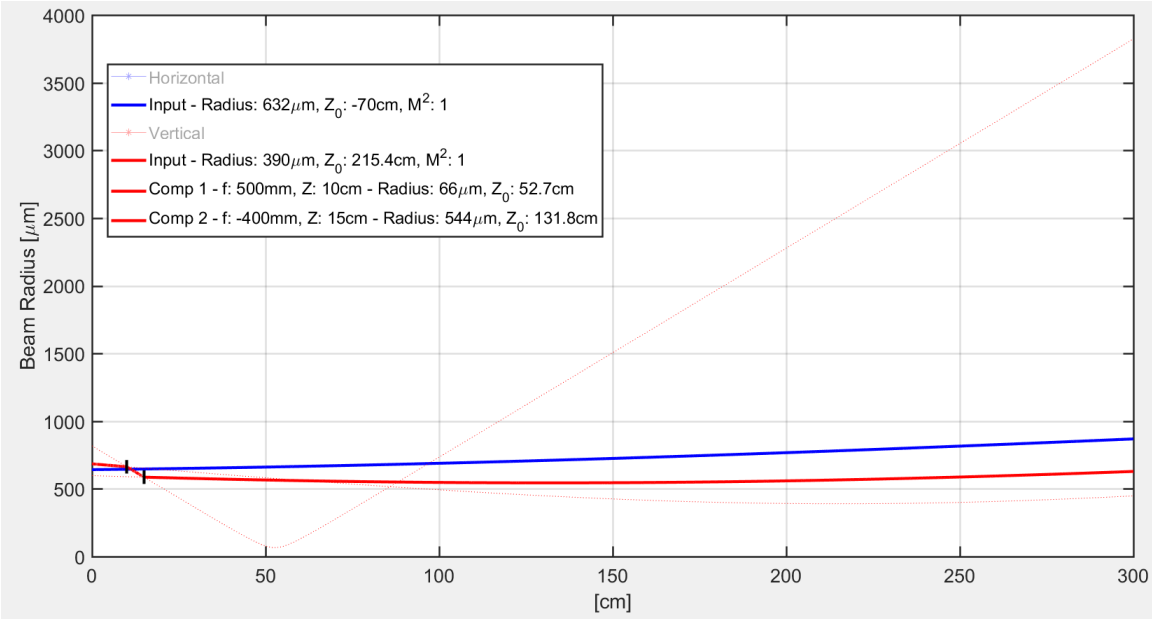

Figure A.5 : Beam propagation calculation reveals a combination of 500 mm and -400 mm cylindrical lenses is required to collimate the free-space UV beam after the UV AOM.

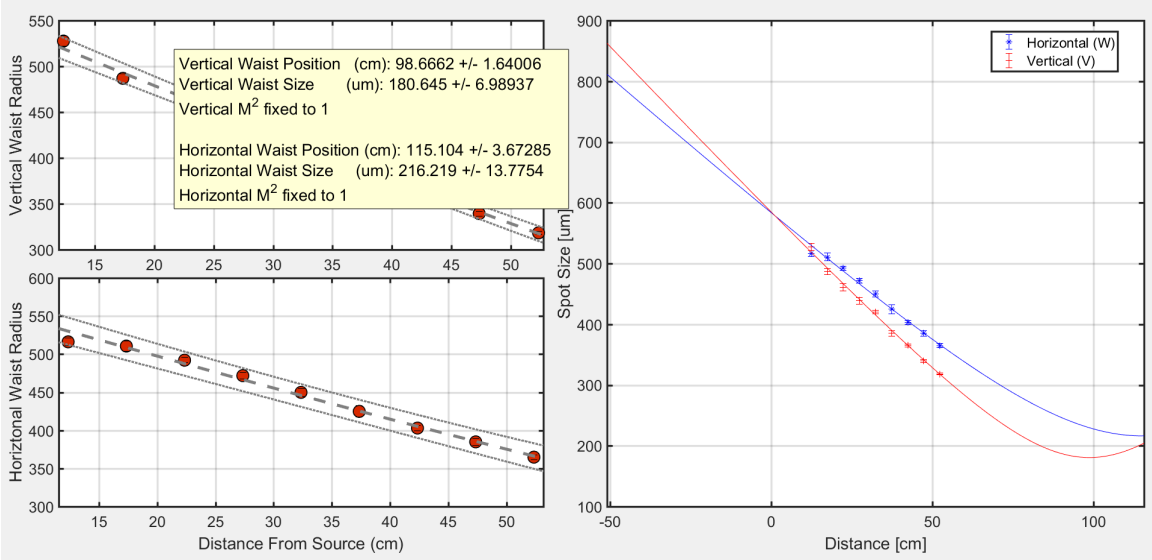

Figure A.6 : Beam profile of light from the output collimator after the UV light is coupled to the fiber on the input end. 0 cm represents the location of the front face of the collimator. The lens position inside the collimator is adjusted to get the best possible collimation.

Appendix B

Trim field box: circuits

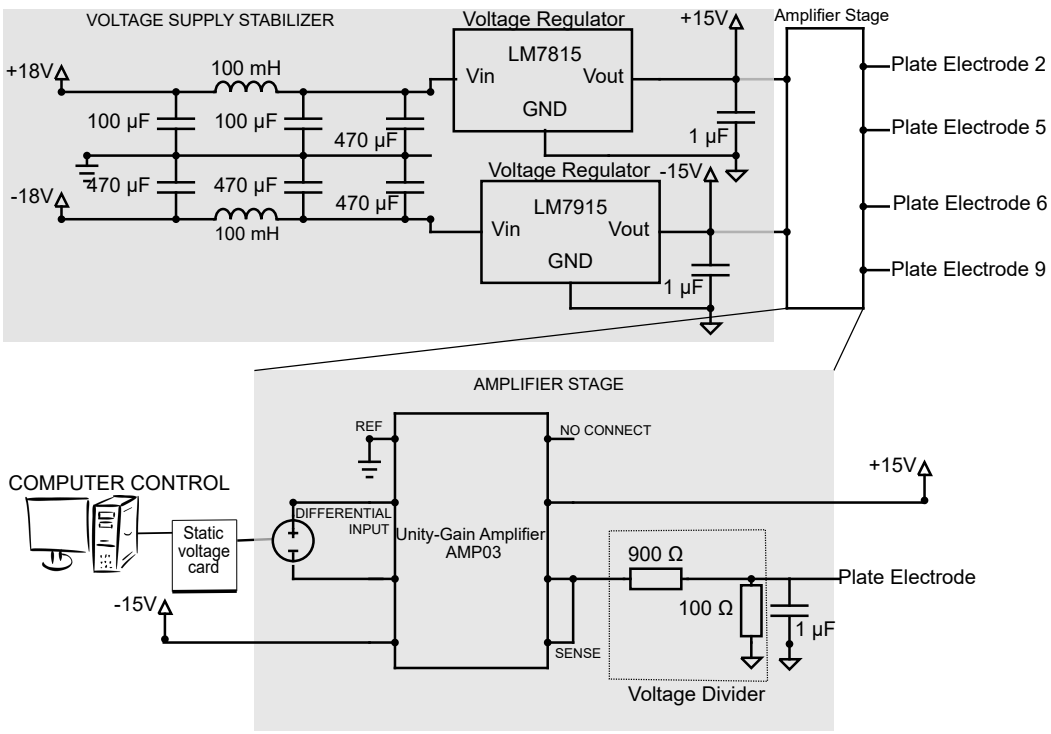

Figure B.1 : Circuit for the trim field setup. Plates 2, 5, 6 and 9 are the plates closest to the MCP. The other four plates are used to apply a voltage ramp to ionize a Rydberg state. The highlighted amplifier stage isolates the static voltage card from the plate electrodes in the chamber to avoid damage by voltage spikes. The static cards can apply ± 10 V. A voltage divider before the electrodes ensures finer offset voltages can be applied to cancel the stray electric fields at higher principal quantum numbers, upto $n = 160$.

Bibliography

[1] O. Boada, A. Celi, J. I. Latorre, and M. Lewenstein, "Quantum Simulation of an Extra Dimension," *Physical Review Letters*, vol. 108, p. 133001, Mar. 2012. Publisher: American Physical Society.

[2] D. I. Tsomokos, S. Ashhab, and F. Nori, "Using superconducting qubit circuits to engineer exotic lattice systems," *Physical Review A*, vol. 82, p. 052311, Nov. 2010. Publisher: American Physical Society.

[3] D. Jukić and H. Buljan, "Four-dimensional photonic lattices and discrete tesseract solitons," *Physical Review A*, vol. 87, p. 013814, Jan. 2013. Publisher: American Physical Society.

[4] O. Boada, A. Celi, J. Rodríguez-Laguna, J. I. Latorre, and M. Lewenstein, "Quantum simulation of non-trivial topology," *New Journal of Physics*, vol. 17, p. 045007, Apr. 2015. Publisher: IOP Publishing.

[5] T. Chalopin, T. Satoor, A. Evrard, V. Makhalov, J. Dalibard, R. Lopes, and S. Nascimbene, "Probing chiral edge dynamics and bulk topology of a synthetic Hall system," *Nature Physics*, vol. 16, pp. 1017–1021, Oct. 2020. Number: 10 Publisher: Nature Publishing Group.

[6] A. Bansil, H. Lin, and T. Das, "Colloquium: Topological band theory," *Reviews of Modern Physics*, vol. 88, p. 021004, June 2016. Publisher: American Physical Society.

[7] X.-L. Qi and S.-C. Zhang, "Topological insulators and superconductors," *Reviews of Modern Physics*, vol. 83, pp. 1057–1110, Oct. 2011.

[8] A. Celi, P. Massignan, J. Ruseckas, N. Goldman, I. Spielman, G. Juzeliūnas, and M. Lewenstein, "Synthetic Gauge Fields in Synthetic Dimensions," *Physical Review Letters*, vol. 112, p. 043001, Jan. 2014. Publisher: American Physical Society.

[9] M. Aidelsburger, S. Nascimbene, and N. Goldman, "Artificial gauge fields in materials and engineered systems," *Comptes Rendus Physique*, vol. 19, pp. 394–432, Sept. 2018.

[10] F. A. An, E. J. Meier, and B. Gadway, "Diffusive and arrested transport of atoms under tailored disorder," *Nature Communications*, vol. 8, p. 325, Aug. 2017. Number: 1 Publisher: Nature Publishing Group.

[11] F. A. An, E. J. Meier, and B. Gadway, "Engineering a Flux-Dependent Mobility Edge in Disordered Zigzag Chains," *Physical Review X*, vol. 8, p. 031045, Aug. 2018. Publisher: American Physical Society.

[12] M. Mancini, G. Pagano, G. Cappellini, L. Livi, M. Rider, J. Catani, C. Sias, P. Zoller, M. Inguscio, M. Dalmonte, and L. Fallani, "Observation of chiral edge states with neutral fermions in synthetic Hall ribbons," *Science*, vol. 349, no. 6255, pp. 1510–1513, 2015. Publisher: American Association for the Advancement of Science _eprint: https://science.sciencemag.org/content/349/6255/1510.full.pdf.

[13] E. Anisimovas, M. Račiūnas, C. Sträter, A. Eckardt, I. B. Spielman, and G. Juzeliūnas, "Semisynthetic zigzag optical lattice for ultracold bosons," *Phys-*

ical Review A, vol. 94, p. 063632, Dec. 2016. Publisher: American Physical Society.

[14] M. L. Wall, A. P. Koller, S. Li, X. Zhang, N. R. Cooper, J. Ye, and A. M. Rey, "Synthetic Spin-Orbit Coupling in an Optical Lattice Clock," *Physical Review Letters*, vol. 116, p. 035301, Jan. 2016. Publisher: American Physical Society.

[15] J. Floß, A. Kamalov, I. S. Averbukh, and P. H. Bucksbaum, "Observation of Bloch Oscillations in Molecular Rotation," *Physical Review Letters*, vol. 115, p. 203002, Nov. 2015. Publisher: American Physical Society.

[16] T. Ozawa and H. M. Price, "Topological quantum matter in synthetic dimensions," *Nature Reviews Physics*, vol. 1, pp. 349–357, May 2019. arXiv: 1910.00376.

[17] B. K. Stuhl, H.-I. Lu, L. M. Aycock, D. Genkina, and I. B. Spielman, "Visualizing edge states with an atomic Bose gas in the quantum Hall regime," *Science*, vol. 349, no. 6255, pp. 1514–1518, 2015. Publisher: American Association for the Advancement of Science _eprint: https://science.sciencemag.org/content/349/6255/1514.full.pdf.

[18] E. J. Meier, F. A. An, A. Dauphin, M. Maffei, P. Massignan, T. L. Hughes, and B. Gadway, "Observation of the topological Anderson insulator in disordered atomic wires," *Science*, vol. 362, pp. 929–933, Nov. 2018. Publisher: American Association for the Advancement of Science.

[19] W. P. Su, J. R. Schrieffer, and A. J. Heeger, "Solitons in Polyacetylene," *Physical Review Letters*, vol. 42, pp. 1698–1701, June 1979. Publisher: American Physical Society.

[20] S. K. Kanungo, J. D. Whalen, Y. Lu, M. Yuan, S. Dasgupta, F. B. Dunning, K. R. A. Hazzard, and T. C. Killian, "Realizing topological edge states with Rydberg-atom synthetic dimensions," *Nature Communications*, vol. 13, p. 972, Feb. 2022. Number: 1 Publisher: Nature Publishing Group.

[21] T. G. Walker and M. Saffman, "Zeros of Rydberg–Rydberg Föster interactions," *Journal of Physics B: Atomic, Molecular and Optical Physics*, vol. 38, pp. S309–S319, Jan. 2005. Publisher: IOP Publishing.

[22] I. I. Ryabtsev, D. B. Tretyakov, I. I. Beterov, and V. M. Entin, "Observation of the Stark-Tuned F\"orster Resonance between Two Rydberg Atoms," *Physical Review Letters*, vol. 104, p. 073003, Feb. 2010. Publisher: American Physical Society.

[23] C. L. Vaillant, M. P. A. Jones, and R. M. Potvliege, "Long-range Rydberg–Rydberg interactions in calcium, strontium and ytterbium," *Journal of Physics B: Atomic, Molecular and Optical Physics*, vol. 45, p. 135004, June 2012. Publisher: IOP Publishing.

[24] A. Browaeys, D. Barredo, and T. Lahaye, "Experimental investigations of dipole–dipole interactions between a few Rydberg atoms," *Journal of Physics B: Atomic, Molecular and Optical Physics*, vol. 49, p. 152001, June 2016. Publisher: IOP Publishing.

[25] M. D. Lukin, M. Fleischhauer, R. Cote, L. M. Duan, D. Jaksch, J. I. Cirac, and P. Zoller, "Dipole Blockade and Quantum Information Processing in Mesoscopic Atomic Ensembles," *Physical Review Letters*, vol. 87, p. 037901, June 2001. Publisher: American Physical Society.

[26] T. Peyronel, O. Firstenberg, Q.-Y. Liang, S. Hofferberth, A. V. Gorshkov, T. Pohl, M. D. Lukin, and V. Vuletić, "Quantum nonlinear optics with single photons enabled by strongly interacting atoms," *Nature*, vol. 488, pp. 57–60, Aug. 2012. Number: 7409 Publisher: Nature Publishing Group.

[27] Y. O. Dudin and A. Kuzmich, "Strongly Interacting Rydberg Excitations of a Cold Atomic Gas," *Science*, vol. 336, pp. 887–889, May 2012. Publisher: American Association for the Advancement of Science.

[28] M. Saffman, T. G. Walker, and K. Mølmer, "Quantum information with Rydberg atoms," *Reviews of Modern Physics*, vol. 82, pp. 2313–2363, Aug. 2010. Publisher: American Physical Society.

[29] C. L. Vaillant, M. P. A. Jones, and R. M. Potvliege, "Multichannel quantum defect theory of strontium bound Rydberg states," *Journal of Physics B: Atomic, Molecular and Optical Physics*, vol. 47, p. 155001, July 2014. Publisher: IOP Publishing.

[30] R. P. Feynman, "Simulating physics with computers," *International Journal of Theoretical Physics*, vol. 21, pp. 467–488, June 1982.

[31] R. Blatt and C. F. Roos, "Quantum simulations with trapped ions," *Nature Physics*, vol. 8, pp. 277–284, Apr. 2012. Number: 4 Publisher: Nature Publishing Group.

[32] A. A. Houck, H. E. Türeci, and J. Koch, "On-chip quantum simulation with superconducting circuits," *Nature Physics*, vol. 8, pp. 292–299, Apr. 2012. Number: 4 Publisher: Nature Publishing Group.

[33] I. Bloch, J. Dalibard, and S. Nascimbène, "Quantum simulations with ultracold quantum gases," *Nature Physics*, vol. 8, pp. 267–276, Apr. 2012. Number: 4 Publisher: Nature Publishing Group.

[34] S. A. Moses, J. P. Covey, M. T. Miecnikowski, D. S. Jin, and J. Ye, "New frontiers for quantum gases of polar molecules," *Nature Physics*, vol. 13, pp. 13–20, Jan. 2017. Number: 1 Publisher: Nature Publishing Group.

[35] C. Monroe, W. Campbell, L.-M. Duan, Z.-X. Gong, A. Gorshkov, P. Hess, R. Islam, K. Kim, N. Linke, G. Pagano, P. Richerme, C. Senko, and N. Yao, "Programmable quantum simulations of spin systems with trapped ions," *Reviews of Modern Physics*, vol. 93, p. 025001, Apr. 2021. Publisher: American Physical Society.

[36] M. J. Hartmann, "Quantum simulation with interacting photons," *Journal of Optics*, vol. 18, p. 104005, Sept. 2016. Publisher: IOP Publishing.

[37] M. Greiner, O. Mandel, T. Esslinger, T. W. Hänsch, and I. Bloch, "Quantum phase transition from a superfluid to a Mott insulator in a gas of ultracold atoms," *Nature*, vol. 415, pp. 39–44, Jan. 2002. Number: 6867 Publisher: Nature Publishing Group.

[38] *The BCS-BEC Crossover and the Unitary Fermi Gas*.

[39] C. Gross and I. Bloch, "Quantum simulations with ultracold atoms in optical lattices," *Science*, vol. 357, pp. 995–1001, Sept. 2017. Publisher: American Association for the Advancement of Science.

[40] I. Georgescu, S. Ashhab, and F. Nori, "Quantum simulation," *Reviews of Modern Physics*, vol. 86, pp. 153–185, Mar. 2014. Publisher: American Physical Society.

[41] W. S. Bakr, J. I. Gillen, A. Peng, S. Fölling, and M. Greiner, "A quantum gas microscope for detecting single atoms in a Hubbard-regime optical lattice," *Nature*, vol. 462, pp. 74–77, Nov. 2009.

[42] N. Schlosser, G. Reymond, I. Protsenko, and P. Grangier, "Sub-poissonian loading of single atoms in a microscopic dipole trap," *Nature*, vol. 411, pp. 1024–1027, June 2001. Number: 6841 Publisher: Nature Publishing Group.

[43] H. Bernien, S. Schwartz, A. Keesling, H. Levine, A. Omran, H. Pichler, S. Choi, A. S. Zibrov, M. Endres, M. Greiner, V. Vuletić, and M. D. Lukin, "Probing many-body dynamics on a 51-atom quantum simulator," *Nature*, vol. 551, pp. 579–584, Nov. 2017. Number: 7682 Publisher: Nature Publishing Group.

[44] L. Livi, G. Cappellini, M. Diem, L. Franchi, C. Clivati, M. Frittelli, F. Levi, D. Calonico, J. Catani, M. Inguscio, and L. Fallani, "Synthetic Dimensions and Spin-Orbit Coupling with an Optical Clock Transition," *Physical Review Letters*, vol. 117, p. 220401, Nov. 2016. Publisher: American Physical Society.

[45] B. Sundar, B. Gadway, and K. R. A. Hazzard, "Synthetic dimensions in ultracold polar molecules," *Scientific Reports*, vol. 8, p. 3422, Feb. 2018. Number: 1 Publisher: Nature Publishing Group.

[46] B. Gadway, "Atom-optics approach to studying transport phenomena," *Physical Review A*, vol. 92, p. 043606, Oct. 2015. Publisher: American Physical Society.

[47] H. M. Price, T. Ozawa, and N. Goldman, "Synthetic dimensions for cold atoms from shaking a harmonic trap," *Physical Review A*, vol. 95, p. 023607, Feb. 2017. Publisher: American Physical Society.

[48] M. H. Anderson, J. R. Ensher, M. R. Matthews, C. E. Wieman, and E. A. Cornell, "Observation of Bose-Einstein Condensation in a Dilute Atomic Vapor," *Science*, vol. 269, pp. 198–201, July 1995. Publisher: American Association for the Advancement of Science.

[49] C. C. Bradley, C. A. Sackett, J. J. Tollett, and R. G. Hulet, "Evidence of Bose-Einstein Condensation in an Atomic Gas with Attractive Interactions," *Physical Review Letters*, vol. 75, pp. 1687–1690, Aug. 1995. Publisher: American Physical Society.

[50] K. B. Davis, M. O. Mewes, M. R. Andrews, N. J. van Druten, D. S. Durfee, D. M. Kurn, and W. Ketterle, "Bose-Einstein Condensation in a Gas of Sodium Atoms," *Physical Review Letters*, vol. 75, pp. 3969–3973, Nov. 1995. Publisher: American Physical Society.

[51] B. DeMarco and D. S. Jin, "Onset of Fermi Degeneracy in a Trapped Atomic Gas," *Science*, vol. 285, pp. 1703–1706, Sept. 1999. Publisher: American Association for the Advancement of Science.

[52] B. DeMarco, "Quantum Behavior of an Atomic Fermi Gas," p. 318.

[53] S. Stellmer, M. K. Tey, B. Huang, R. Grimm, and F. Schreck, "Bose-Einstein Condensation of Strontium," *Physical Review Letters*, vol. 103, p. 200401, Nov. 2009. Publisher: American Physical Society.

[54] Y. N. M. de Escobar, P. G. Mickelson, M. Yan, B. J. DeSalvo, S. B. Nagel, and T. C. Killian, "Bose-Einstein Condensation of $ˆ{84}\mathrm{Sr}$," *Physical Review Letters*, vol. 103, p. 200402, Nov. 2009. Publisher: American Physical Society.

[55] P. G. Mickelson, Y. N. Martinez de Escobar, M. Yan, B. J. DeSalvo, and T. C. Killian, "Bose-Einstein condensation of $ˆ{88}\mathrm{Sr}$ through sympathetic cooling with $ˆ{87}\mathrm{Sr}$," *Physical Review A*, vol. 81, p. 051601, May 2010. Publisher: American Physical Society.

[56] S. Stellmer, M. K. Tey, R. Grimm, and F. Schreck, "Bose-Einstein condensation of $ˆ{86}\mathrm{Sr}$," *Physical Review A*, vol. 82, p. 041602, Oct. 2010. Publisher: American Physical Society.

[57] B. J. DeSalvo, M. Yan, P. G. Mickelson, Y. N. Martinez de Escobar, and T. C. Killian, "Degenerate Fermi Gas of $ˆ{87}\mathrm{Sr}$," *Physical Review Letters*, vol. 105, p. 030402, July 2010. Publisher: American Physical Society.

[58] M. K. Tey, S. Stellmer, R. Grimm, and F. Schreck, "Double-degenerate Bose-Fermi mixture of strontium," *Physical Review A*, vol. 82, p. 011608, July 2010. Publisher: American Physical Society.

[59] S. Stellmer, F. Schreck, and T. C. Killian, "DEGENERATE QUANTUM GASES OF STRONTIUM," in *Annual Review of Cold Atoms and Molecules*, vol. 2, pp. 1–80, WORLD SCIENTIFIC, May 2014.

[60] M. M. Boyd, A. D. Ludlow, S. Blatt, S. M. Foreman, T. Ido, T. Zelevinsky, and J. Ye, "$ˆ{87}\mathrm{Sr}$ Lattice Clock with Inaccuracy below ${10}ˆ{\ensuremath{-}15}$," *Physical Review Letters*, vol. 98, p. 083002, Feb. 2007. Publisher: American Physical Society.

[61] F. Camargo, *Camargo_PhD.pdf*. PhD thesis.

[62] R. Ding, *Narrow Line Cooling of 84Sr*. PhD thesis.

[63] J. D. Whalen, *Probing nonlocal correlations with ultralong-range Rydberg molecules*. PhD thesis.

[64] S. Stellmer, F. Schreck, and T. C. Killian, "Degenerate quantum gases of strontium," *arXiv:1307.0601 [cond-mat, physics:physics]*, vol. 2, pp. 1–80, May 2014. arXiv: 1307.0601.

[65] R. Grimm, M. Weidemüller, and Y. B. Ovchinnikov, "Optical Dipole Traps for Neutral Atoms," in *Advances In Atomic, Molecular, and Optical Physics* (B. Bederson and H. Walther, eds.), vol. 42, pp. 95–170, Academic Press, Jan. 2000.

[66] K. M. O'Hara, M. E. Gehm, S. R. Granade, and J. E. Thomas, "Scaling laws for evaporative cooling in time-dependent optical traps," *Physical Review A*, vol. 64, p. 051403, Oct. 2001. Publisher: American Physical Society.

[67] H. Kogelnik and T. Li, "Laser Beams and Resonators," *Applied Optics*, vol. 5, pp. 1550–1567, Oct. 1966. Publisher: Optica Publishing Group.

[68] C. J. Foot and D. o. P. C. J. Foot, *Atomic Physics*. OUP Oxford, 2005. Google-Books-ID: kXYpAQAAMAAJ.

[69] D. Budker, D. Kimball, D. F. Kimball, and D. P. DeMille, *Atomic Physics: An Exploration Through Problems and Solutions*. Oxford University Press, 2004.

[70] E. D. Black, "An introduction to Pound–Drever–Hall laser frequency stabilization," *American Journal of Physics*, vol. 69, pp. 79–87, Jan. 2001. Publisher: American Association of Physics Teachers.

[71] C. D. Marciniak, H. B. Ball, A. T.-H. Hung, and M. J. Biercuk, "Towards fully commercial, UV-compatible fiber patch cords," *Optics Express*, vol. 25,

pp. 15643–15661, July 2017. Publisher: Optica Publishing Group.

[72] T. F. Gallagher, *Rydberg Atoms*. Cambridge Monographs on Atomic, Molecular and Chemical Physics, Cambridge: Cambridge University Press, 1994.

[73] S. H. Autler and C. H. Townes, "Stark Effect in Rapidly Varying Fields," *Physical Review*, vol. 100, pp. 703–722, Oct. 1955. Publisher: American Physical Society.

[74] K. v. Klitzing, G. Dorda, and M. Pepper, "New Method for High-Accuracy Determination of the Fine-Structure Constant Based on Quantized Hall Resistance," *Physical Review Letters*, vol. 45, pp. 494–497, Aug. 1980. Publisher: American Physical Society.

[75] M. Atala, M. Aidelsburger, J. T. Barreiro, D. Abanin, T. Kitagawa, E. Demler, and I. Bloch, "Direct measurement of the Zak phase in topological Bloch bands," *Nature Physics*, vol. 9, pp. 795–800, Dec. 2013. Number: 12 Publisher: Nature Publishing Group.

[76] S. Nakajima, T. Tomita, S. Taie, T. Ichinose, H. Ozawa, L. Wang, M. Troyer, and Y. Takahashi, "Topological Thouless pumping of ultracold fermions," *Nature Physics*, vol. 12, pp. 296–300, Apr. 2016. Number: 4 Publisher: Nature Publishing Group.

[77] S. de Léséleuc, V. Lienhard, P. Scholl, D. Barredo, S. Weber, N. Lang, H. P. Büchler, T. Lahaye, and A. Browaeys, "Observation of a symmetry-protected topological phase of interacting bosons with Rydberg atoms," *Science*, vol. 365, pp. 775–780, Aug. 2019.

[78] H.-I. Lu, M. Schemmer, L. Aycock, D. Genkina, S. Sugawa, and I. Spielman,

"Geometrical Pumping with a Bose-Einstein Condensate," *Physical Review Letters*, vol. 116, p. 200402, May 2016. Publisher: American Physical Society.

[79] E. J. Meier, F. A. An, and B. Gadway, "Observation of the topological soliton state in the Su–Schrieffer–Heeger model," *Nature Communications*, vol. 7, p. 13986, Dec. 2016. Number: 1 Publisher: Nature Publishing Group.

[80] D. Xie, W. Gou, T. Xiao, B. Gadway, and B. Yan, "Topological characterizations of an extended Su–Schrieffer–Heeger model," *npj Quantum Information*, vol. 5, pp. 1–5, May 2019. Number: 1 Publisher: Nature Publishing Group.

[81] V. Dal Lago, M. Atala, and L. E. F. Foa Torres, "Floquet topological transitions in a driven one-dimensional topological insulator," *Physical Review A*, vol. 92, p. 023624, Aug. 2015. Publisher: American Physical Society.

[82] D. Barredo, H. Labuhn, S. Ravets, T. Lahaye, A. Browaeys, and C. S. Adams, "Coherent Excitation Transfer in a Spin Chain of Three Rydberg Atoms," *Physical Review Letters*, vol. 114, p. 113002, Mar. 2015. Publisher: American Physical Society.

[83] A. Signoles, E. Dietsche, A. Facon, D. Grosso, S. Haroche, J. Raimond, M. Brune, and S. Gleyzes, "Coherent Transfer between Low-Angular-Momentum and Circular Rydberg States," *Physical Review Letters*, vol. 118, p. 253603, June 2017. Publisher: American Physical Society.

[84] B. Sundar, M. Thibodeau, Z. Wang, B. Gadway, and K. R. A. Hazzard, "Strings of ultracold molecules in a synthetic dimension," *Physical Review A*, vol. 99, p. 013624, Jan. 2019. Publisher: American Physical Society.

[85] S. Ebadi, T. T. Wang, H. Levine, A. Keesling, G. Semeghini, A. Omran, D. Bluvstein, R. Samajdar, H. Pichler, W. W. Ho, S. Choi, S. Sachdev, M. Greiner, V. Vuletić, and M. D. Lukin, "Quantum phases of matter on a 256-atom programmable quantum simulator," *Nature*, vol. 595, pp. 227–232, July 2021. Number: 7866 Publisher: Nature Publishing Group.

[86] P. Scholl, M. Schuler, H. J. Williams, A. A. Eberharter, D. Barredo, K.-N. Schymik, V. Lienhard, L.-P. Henry, T. C. Lang, T. Lahaye, A. M. Läuchli, and A. Browaeys, "Quantum simulation of 2D antiferromagnets with hundreds of Rydberg atoms," *Nature*, vol. 595, pp. 233–238, July 2021. Number: 7866 Publisher: Nature Publishing Group.

[87] R. V. Jensen, S. M. Susskind, and M. M. Sanders, "Chaotic ionization of highly excited hydrogen atoms: Comparison of classical and quantum theory with experiment," *Physics Reports*, vol. 201, pp. 1–56, Mar. 1991.

[88] M. A. J. Herrera, S. N. Kempkes, M. B. de Paz, A. García-Etxarri, I. Swart, C. M. Smith, and D. Bercioux, "Corner modes of the breathing kagome lattice: Origin and robustness," *Physical Review B*, vol. 105, p. 085411, Feb. 2022. Publisher: American Physical Society.